



Politecnico di Torino

Master of Science in Mechanical Engineering

July 2021

Master thesis

Visualization of flame-fluid interactions and influence on kernel growth
in a DISI Engine

Academic Supervisor:

Prof. Federico Millo

CNR - STEMS Supervisors:

Dr. Simona Silvia Merola

Dr. Eng. Adrian Irimescu

Candidate:

Giovanni Cecere

Abstract

The ever more demanding of fuel economy and emission standards require innovative control strategies for internal combustion engines (ICE) and new procedures for the use of alternative fuels as well as improved after-treatment systems. This development is intrinsically linked to improved understanding of in-cylinder processes, with complex dependencies between phenomena that are related to flow, thermal and chemical engineering. In this thesis, kernel formation and flame front propagation were investigated in an optically accessible Direct Injection Spark Ignition (DISI) engine. The optical analysis was made possible by a Bowditch design that features an extended piston combined with a quartz window mounted within the piston crown. The results pertaining to this work can be divided into two categories: the first one dedicated to the thermodynamic analysis, i.e. the analysis of parameters derived from in-cylinder pressure measurements (Indicated Mean Effective Pressure IMEP, Covariance of the same COV_{IMEP} , Net Heat Release Rate NHRR, Mass Fraction Burned MFB, Volume Fraction Burned VFB etc.); the second part of the study is focused on the optical analysis of images related to the sequencies obtained through cycle-resolved digital imaging using a high-speed camera. Therefore, the two types of data were combined and compared to investigate how changing operative parameters affect the thermodynamic and optical results. Three different configurations (i.e. Cross-, Counter- and Uniflow with respect to the direction of tumble) in terms of spark plug orientations further emphasized the complex interaction between chemical phenomena and fluid motion. One of the main conclusions was that the spark plug orientation plays a significant role in flame kernel displacement and influences the direction of propagation of the flame front. Thanks to the large amount of experimental data acquired in the laboratory, a further goal of this research is to create a statistical database that contains detailed information on flame kernel formation and evolution. This database will constitute a solid basis for validation and implementation of a 3D CFD model capable of providing valuable information on the in-cylinder phenomena.

Acknowledgements

First of all, I would like to thank my relator Prof. Federico Millo for the opportunity given to me to start this experience and acquire new knowledge on a topic that for me is particularly important. If you believe in the fascinating technology of the Internal Combustion Engine, the land vehicle propulsion course, held by Prof. Millo at Polito, is the one for you.

I can't not mention my CNR supervisors Simona Silvia Merola and Ing. Adrian Irimescu for the daily motivation that they gave to me and attention to my personal growth path. With people like them, it is possible to understand the importance of the man or woman behind the researcher.

I must also thank the Prof. Luciano Rolando and the PhD student Fabrizio Gullino for the availability given in these months for the Gt-Suite software.

Special thanks go to my family, without whom I would never have reached this point in my life. You have always supported me and allowed me to make the choice I wanted without any limitation. Thank you, really.

I thank my girlfriend for her patience for staying with me even when I was away. You loved me like no one (yes, I know, it's an obvious statement) and I promise you none of our distant past days will have been useless. Thanks, Ida.

And now the list of my wonderful (and terrible) friends. The first ones, the guys of Doc magnus, a jumble of disreputable but wonderful elements, with the honorary member Peppe Venezia, better known as lù Veneziano. It is not important if you are tall, small, a doctor, a communist, a Chinese interpreter, or a ninja, I lovely hate all of you.

GG8, I know you are reading. Now you have unlocked 20 Disaronno sour offered by me. Yeah, you have a problem with alcohol, maybe I too...well, very well.

Guido, nothing, thank you Red. TVB.

Finally, I want to dedicate a thought to my grandmother who is no longer there. I am not a great believer, and honestly, I don't know if there is "another side", but listen to me if you are somewhere, "Hey Nonna, look at me, now I am a Mechanical Engineer". Probably it is better to say it in Napoletano..."Nonna, m' sò Laureat".

Life is a soup, and you are a fork.

Cit. Giovanni Cecere (After some drinks)

Contents

List of Figures	i
Chapter 1 Figures	i
Chapter 2 Figures	i
Chapter 3 Figures	i
Chapter 4 Figures	ii
Chapter 5 Figures	ii
Chapter 6 Figures	iii
Acronyms and Symbols	iv
Introduction	1
Background	1
Chapter 1	6
Literature Review	6
1.1 Optically accessible engine history and evolution	6
1.2 Cycle to Cycle Variability and Flame Kernel Growth	8
1.3 Homogeneous charge injection strategy	11
1.4 DISI Mixture Formation and Control	13
1.5 Motivation and Research Goal	14
Chapter 2	15
Experimental Setup	15
2.1 Engine System Setup	15
2.2 Optical Setup	22
Chapter 3	26
Procedure and Measurement Methodology	26
3.1 Thermodynamic Analysis	26
3.2 Current Signals Analysis	30
3.3 Optical Data Analysis	31
Chapter 4	35
4.1 Coil Charge Duration Analysis	35
Chapter 5	44
Results	44

5.1 Operative Conditions	44
5.2 Thermodynamic Results.....	46
5.2.1 Thermodynamic Results for Fixed Spark Advance (SA)	46
5.2.2 Thermodynamic Results for Fixed Lambda (λ).....	55
5.3 Optical Results.....	63
5.3.1 Optical Results for Fixed Spark Advance (SA)	64
5.3.2 Optical Results for Fixed Lambda (λ).....	71
5.4 Flame Front Velocity Analysis	78
Chapter 6.....	81
GT-Power Model	81
6.1 Overall Calibration of the GT-Power Model	83
6.2 Combustion Sub-Model Calibration.....	85
6.3 Simulation Model Results	90
Conclusive Remarks	96
References	98

List of Figures

Chapter 1 Figures

Figure 1. 1, World energy consumption by source (1994-2019).....	1
Figure 1. 2, Global energy-related CO ₂ emissions by sector (March 2021) [2].	2
Figure 1. 3, GHG emissions evolution for EU (1990-2018) [4].....	3
Figure 1. 4, Expected Demand Growth Increase to 2030 in the EV Industry [6].....	4
Figure 1. 5, (a) Schematic diagram of Bowditch's slotted, extended piston design from [11],	7
Figure 1. 6, Left: Double Fine Wire spark plug, Right: oval-J spark plug [19].	10
Figure 1. 7, On the top, from left to right: Counter-flow, Cross-flow, on the bottom: Cross-flow (for the oval-J this configuration is set to 100° respect to the vertical), Uniflow [19].....	10
Figure 1. 8, Laminar burning velocity for several fuels as function of equivalence ratio, [17].	12
Figure 1. 9, Different types of DISI combustion system [26].	13

Chapter 2 Figures

Figure 2. 1, Schematic representation of the experimental setup [29].	16
Figure 2. 2, (a) Magneti Marelli Injector, (b) Injector nozzle.....	16
Figure 2. 3, AVL ETU pulse generator.....	17
Figure 2. 4, Injection control unit.	17
Figure 2. 5, (a) CROSSFLOW configuration, (b) UNIFLOW configuration, (c) COUNTERFLOW configuration.	18
Figure 2. 6, Engine experimental setup.....	20
Figure 2. 7, Electric motor/brake coupled with the engine (49.7 kW power, 230 Nm maximum torque). .	21
Figure 2. 8, 3D render visualization of piston crown.	22
Figure 2. 9, Schematic representation of a Bowditch extended piston [35].....	23
Figure 2. 10, High-speed camera CMOS, CamRecord 5000 by Optronis [37].	24
Figure 2. 11, Camera gating for acquiring 25 images per cycle.	24

Chapter 3 Figures

Figure 3. 1, LabView script for in-cylinder pressure analysis.....	26
Figure 3. 2, Simplified cylinder geometry [17].	27
Figure 3. 3, Primary and secondary current intensity signals.	30
Figure 3. 4, Steps of the NI Vision script used for image processing.	32
Figure 3. 5, Flame front propagation comparison of two consecutive frames.	33

Chapter 4 Figures

Figure 4. 1, Secondary current signal during discharge phase, $\lambda=1.00$.	36
Figure 4. 2, Secondary current signal during discharge phase, $\lambda=1.15$.	36
Figure 4. 3, Secondary current signal during discharge phase, $\lambda=1.30$.	37
Figure 4.4, COV-Is for $\lambda=1.00-1.15-1.30$.	38
Figure 4. 5, In-Cylinder Pressure Traces, IMEP for COV_{IMEP} for $\lambda=1.00$.	40
Figure 4. 6, In-Cylinder Pressure Traces, IMEP for COV_{IMEP} for $\lambda=1.15$.	41
Figure 4. 7, In-Cylinder Pressure Traces, IMEP for COV_{IMEP} for $\lambda=1.30$.	42

Chapter 5 Figures

Figure 5. 1, In-Cylinder pressure traces, $\lambda=1.15$, Spark Advance 12 CAD.	45
Figure 5. 2, In-cylinder Pressure traces for $\lambda=1.00$.	46
Figure 5. 3, In-cylinder Pressure traces for $\lambda=1.15$.	47
Figure 5. 4, In-cylinder Pressure traces for $\lambda=1.30$.	47
Figure 5. 5, IMEP and COV_{IMEP} for $\lambda=1.00-1.15-1.30$.	49
Figure 5. 6, P max and $COV_{P_{MAX}}$ for $\lambda=1.00-1.15-1.30$.	50
Figure 5. 7, Mass Fraction Burned for $\lambda=1.00-1.15-1.30$.	52
Figure 5. 8, COV-Is for $\lambda=1.00-1.15-1.30$.	54
Figure 5. 9, In-cylinder Pressure traces for $\lambda=1.15$ and SA 8 CAD.	55
Figure 5. 10, In-cylinder Pressure traces for $\lambda=1.15$ and SA 12 CAD.	56
Figure 5. 11, In-cylinder Pressure traces for $\lambda=1.15$ and SA 16 CAD.	56
Figure 5. 12, In-cylinder Pressure traces for $\lambda=1.15$ and SA 20 CAD.	57
Figure 5. 13, In-cylinder pressure traces for $\lambda=1.15$ and SA 24 CAD.	57
Figure 5. 14, IMEP and COV_{IMEP} values for the Spark Advance sweep, $\lambda=1.15$.	59
Figure 5. 15, $COV_{P_{MAX}}$ values for the spark timing sweep, $\lambda=1.15$.	60
Figure 5. 16, Mass Fraction Burned for $\lambda=1.15$ and Spark Advance from 8 to 24 CAD.	62
Figure 5. 17, COV – Secondary Current Intensity, $\lambda=1.15$.	62
Figure 5. 18, Volume Fraction Burned comparison with normalized area, $\lambda=1.15$, SA16 CAD, Counterflow configuration.	64
Figure 5. 19, Flame image sequence during the flame propagation stage, $\lambda=1.00$, SA12 CAD.	65
Figure 5. 20, Flame image sequence during the flame propagation stage, $\lambda=1.15$, SA12 CAD.	65
Figure 5. 21, Flame image sequence during the flame propagation stage, $\lambda=1.30$, SA12 CAD.	66
Figure 5. 22, Displacement along the vertical axis respect to the spark plug center, (a) frame at 14 CAD ASOS, (b) frame at 16.4 CAD ASOS.	67
Figure 5. 23, Displacement along the horizontal axis respect to the spark plug center, (a) frame at 14 CAD ASOS, (b) frame at 16.4 CAD ASOS.	67
Figure 5. 24, (a) Percentages of Up-Down events, (b) Percentages of Right-Left events for frame at 14 CAD ASOS, SA12 CAD.	68
Figure 5. 25, Radial displacement of flame area center respect to the spark plug center for frames at 14-16.4 CAD ASOS.	68

Figure 5. 26, Flame area center locations for the Uniflow configuration for frame at 16.4 CAD ASOS, SA12 CAD.	69
Figure 5. 27, Flame area center locations for the Crossflow configuration for frame at 16.4 CAD ASOS, SA12 CAD.	69
Figure 5. 28, Flame area center locations for the Counterflow configuration for frame at 16.4 CAD ASOS, SA12 CAD.	70
Figure 5. 29, Flame image sequence during the flame propagation stage, SA8 CAD, $\lambda=1.15$	71
Figure 5. 30, Flame image sequence during the flame propagation stage, SA12 CAD, $\lambda=1.15$	72
Figure 5. 31, Flame image sequence during the flame propagation stage, SA16 CAD, $\lambda=1.15$	72
Figure 5. 32, Flame image sequence during the flame propagation stage, SA20 CAD, $\lambda=1.15$	73
Figure 5. 33, Flame image sequence during the flame propagation stage, SA24 CAD, $\lambda=1.15$	73
Figure 5. 34, Displacement along the vertical axis respect to the spark plug center, (a) frame at 14 CAD ASOS, (b) frame at 16.4 CAD ASOS.	74
Figure 5. 35, Displacement along the horizontal axis respect to the spark plug center, (a) frame at 14 CAD ASOS, (b) frame at 16.4 CAD ASOS.	74
Figure 5. 36, (a) Percentages of Up-Down events, (b) Percentages of Right-Left events for frame at 14 CAD ASOS, $\lambda=1.15$	74
Figure 5. 37, Radial displacement of flame area center respect to the spark plug center for frames at 14-16.4 CAD ASOS, $\lambda=1.15$	75
Figure 5. 38, Flame area center locations for the Uniflow configuration, $\lambda=1.15$, frame at 16.4 CAD ASOS.	75
Figure 5. 39, Flame area center locations for the Crossflow configuration, $\lambda=1.15$, frame at 16.4 CAD ASOS.	76
Figure 5. 40, Flame area center locations for the Counterflow configuration, $\lambda=1.15$, frame at 16.4 CAD ASOS.	76
Figure 5. 41, Frame Front speed, SA8 CAD.	78
Figure 5. 42, Frame Front speed, SA12 CAD.	79
Figure 5. 43, Frame Front speed, SA16 CAD.	79
Figure 5. 44, Frame Front speed, SA20 CAD.	80

Chapter 6 Figures

Figure 6. 1, Gt-Power simulation model.	82
Figure 6. 2, In-Cylinder Pressure during the intake-stroke, motored condition.	83
Figure 6. 3, In-Cylinder Pressure Traces Comparison, motored condition.	84
Figure 6. 4, Optimizer parameters setting.	86
Figure 6. 5, SITurb parameters effect on In-Cylinder pressure.	88
Figure 6. 6, Factors range limit setting.	89
Figure 6. 7, In-cylinder Pressure traces comparison, $\lambda=1.15$, SA8 to 24 CAD BTDC.	91
Figure 6. 8, In-cylinder Pressure traces comparison, SA12 CAD BTDC, $\lambda=1.00-1.15-1.30$	92
Figure 6. 9, In-Cylinder Pressure traces for $\lambda=1.30$, SA 12 CAD.	93

Figure 6. 10, Simulated (solid lines) and measured flame area (lines with symbols) for variable spark timing and air-fuel ratio.....	94
--	----

List of Tables

Table 2. 1, Engine Specifications.....	15
Table 3. 1, Flame area morphology parameters.....	34
Table 3. 2, Standard deviation and COV of main parameters of flame area Morphology.	34
Table 4. 1, Parameters set for Coil Charge Duration investigation.....	35
Table 5. 1, Engine operative conditions.....	44
Table 6. 1, Calculated parameters error, $\lambda=1.15$, SA8 to 24 CAD BTDC.	91
Table 6. 2, Calculated parameters error, SA12 CAD BTDC, $\lambda=1.00-1.15-1.30$	92

Acronyms and Symbols

AFR Air Fuel Ratio

ASOS After Star of Spark

ATDC After Top Dead Center

BDC Bottom Dead Center

BTDC Before Top Dead Center

CAD Crank Angle Degree

CCD Coupled Charge Device

CCV Cycle-to-Cycle Variability

CFD Computational Fluid Dynamics

COV Coefficient of Variation

DOI Duration of Injection

GHG Greenhouse Gas

ICE Internal Combustion Engine

PM Particulate Matter

UHC Unburned Hydrocarbons

DISI Direct-Injection Spark-Ignition

EV Electric Vehicle

EVC Exhaust Valve Closing

EVO Exhaust Valve Opening

IMEP Indicated Mean Effective Pressure

IVC Intake Valve Closing

IVO Intake Valve Opening

MBT Maximum Brake Torque

MFB Mass Fraction Burned

NHRR Net Heat Release Rate

ON Octane Number

PFI Port Fuel Injection

SA Spark Advance

SOI Start of Injection

TDC Top Dead Center

VFB Volume Fraction Burned

WFA Wetted Flame Area

ZEV Zero Emission Vehicle

Introduction

Background

Internal Combustion Engines (ICE) are an integral and fundamental part of road transportation; this statement applies to Europe as well as to the US and China but looking at the information given by media it seems that the era of ICE is nearing its technological sunset. Complete vehicle electrification is imminent and with it most of the problems related to the Greenhouse Gas (GHG) emissions produced by this sector will be solved (at least at tail-pipe level); this is the daily message that can be read in a magazine or via web. Due to this demonization of the IC engine by the media, there are more and more people who are convinced that this information is true, but the reality is quite different. A statistical Review of the World Energy 2020 journal [1] has calculated that the total demand of fossil fuel oil grew by 0.9 million barrels per day (b/d) in 2019, slightly lower than the 10-year average of 1.3%. The largest increase in consumption was registered in China, while as an oil producer the US experienced an increase higher than any country for the third consecutive year. Although renewable energy has undergone important growth (more than 40% increase respect to previous years), as can be seen in figure 1.1, oil is the primary source of energy.

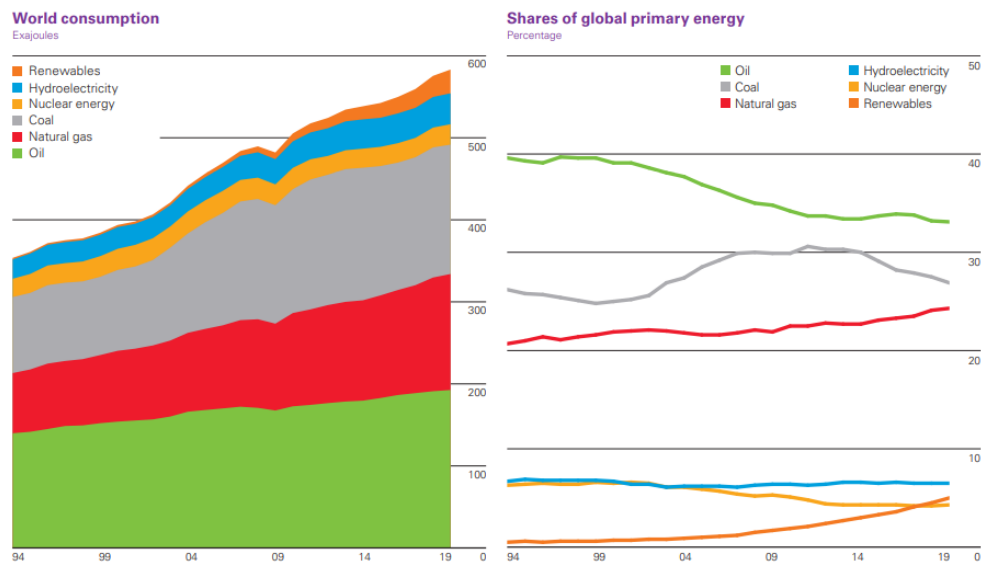


Figure 1. 1, World energy consumption by source (1994-2019).

The oil fuel is the first used energy source with 33.1% [1].

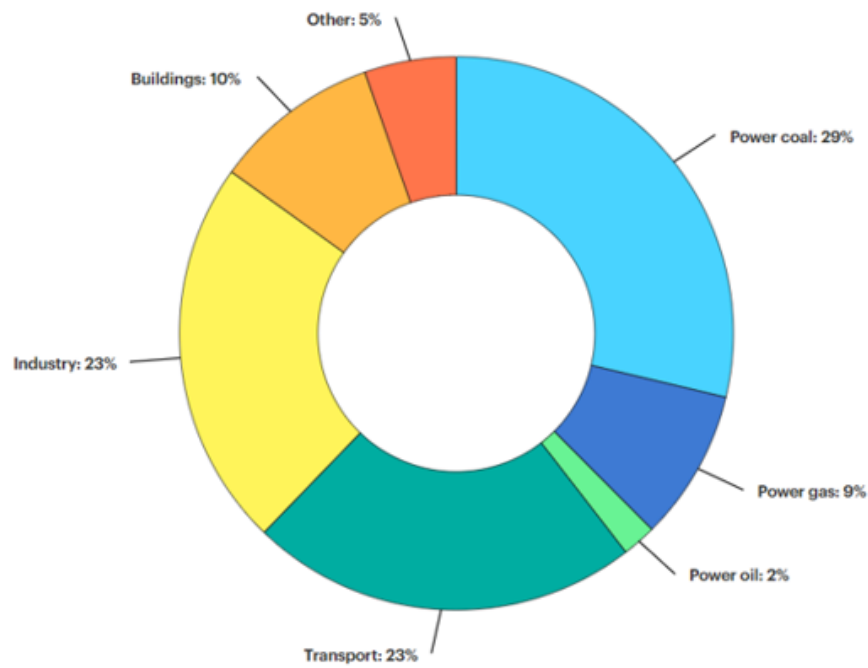


Figure 1. 2, Global energy-related CO₂ emissions by sector (March 2021) [2].

Replacing ICEs with the Zero Emission Vehicles (ZEV's) is showed as something of acceptable and imminent, and consequently the new generations of students tend to be distant and disinterested in this technology. The massive attack that the ICE technology is undergoing, however, is not matched by the proposal of a valid alternative. Currently, in the world there are around 1.2 billion of light-duty vehicles and 380 million of heavy-duty vehicles and the daily demand for the liquid fuels exceeds 11 billion liters. Numbers destined to increase; in fact the EIA predicts that for the US transport market alone the total number of cars and light-trucks on the road will increase by 23%, from 240 million in 2015 to 295 million in 2050. So, considering that in 2015 in the US 98.1% of light-duty vehicles were driven using gasoline, diesel, or flex/fuel ethanol and that this value will drop to 85.5% in 2050, the number of IC engines on the road will increase approximately by 47 million over the next three decades [3]. For these reasons, ICE's technology has undergone many improvements over the past decades, more than any other technology, and looking at future predictions the research for further improvements must continue. A simplified analysis on the evolving efficiency of the ICE technology and related after-treatment systems, can be obtained by comparing the European transport GHG emissions in the last three decades.

Looking at the statistics from the European Environment Agency, thanks to the ever more stringent norms in terms of GHG emissions, this value has been reduced by more than 20% [4] from the 1990. Figure 1.3 shows the evolution of GHG emissions trend.

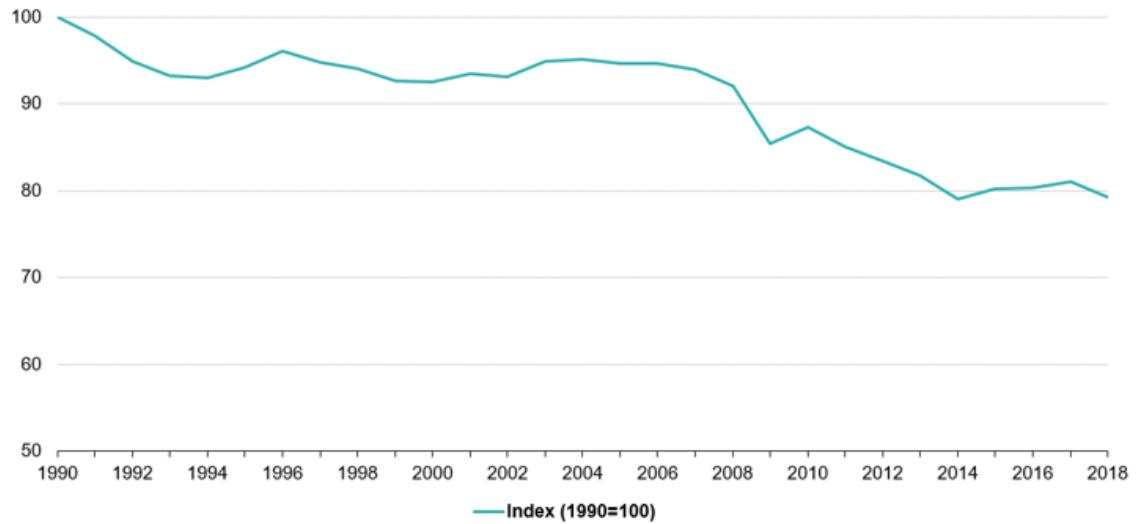


Figure 1. 3, GHG emissions evolution for EU (1990-2018) [4].

Another consideration is linked to the idea that with an Electric Vehicle (EV) it is possible to reach “zero emissions level”. This false “myth” does not take into account the fact that GHG emissions are only delocalized and not eliminated; electricity must be produced to drive EVs and for this reason fossil fuel is needed (considering that the industrial sector is strongly dependant on coal) as renewable energy sources are far from levels that can satisfy the global energy demand [1]. Finally, there are social reasons as well, for which most vehicles with ICEs cannot completely be replaced with their electric counterpart: cost (mostly upfront investment rather than operational costs). An average electric car has a much higher price than a common vehicle with the same dimension, without mentioning the problem related with the battery autonomy and consequently limited range. The causes behind such a high price are directly linked to the demand for materials used in Electric Vehicles (EV’s). Some considerations can be made on the data reported in [5,6], where the future problem linked to the growth in demand for materials for the production of batteries is also faced (figure 1.4).

Metal	Expected Demand Growth Increase to 2030 in the EV Industry
Nickel	14x
Aluminum	14x
Phosphorus	13x
Iron	13x
Copper	10x
Graphite	10x
Lithium	9x
Cobalt	3x
Manganese	3x

Figure 1. 4, Expected Demand Growth Increase to 2030 in the EV Industry [6].

After all these considerations, it is therefore intuitive that there is need a to continuously improve the efficiency of ICEs. The scientific community has made many important steps forward in the last decades, one of which has been the introduction of the Direct-Injection Spark-Ignition (DISI) engine technology. The first commercially available DISI powered vehicle was the Mitsubishi Galant in 1996 and in 2008 only the 2.3% of vehicles used DISI engine; this value has increased to over 45% by 2015 [7]. The pressure inside of a direct injection system must be higher compared to the PFI (Port Fuel Injection) system mainly due to injection time and backpressure constraints. One of the DISI engine advantages is the possibility to use the strategy of stratified charge for low load engine operative condition. With this strategy the injection timing is set near the end of the compression stroke, and this allows to have a rich mixture around the spark plug and an overall lean charge in the combustion chamber. For mid or high engine loads the stratified strategy is no longer possible due to the formation of wetting zones and consequently an increase of PM and UHC emissions [8]. There are also benefits to a DISI engine when operating in homogeneous mode. In fact, injecting during the intake phase directly into the combustion chamber, the volumetric efficiency increases (during the vaporization phase the overall mixture temperature decreases) and consequently, it is possible to take in more air (hence, more output power) [9].

In this study the experimental results, performed on an optically accessible single-cylinder DISI engine, are reported. The tests carried out in the laboratory concern different levels of Air-Fuel ratio (AFR) and Spark Advance (SA) for a set engine speed of 2000 rpm. The spark plug was kept in the configurations Uniflow, Crossflow and Counterflow. In the first one the ground electrode is

in line with the tumble motion, in the Cross the spark plug is rotated by 90 angles degree with respect to the previous orientation, while for the latter the ground electrode orientation is opposite to the tumble motion. Therefore, this work aims to study the effect on the flame kernel formation and flame front propagation for the above-mentioned operative parameters.

Chapter 1

Literature Review

1.1 Optically accessible engine history and evolution

From the beginning of the development of ICEs, the idea of being able to directly observe the phenomena that were taking place inside the combustion chamber has fascinated many researchers and scientists. This became possible with the introduction of the first model of an optically accessible engine by Nicolaus Otto [10] in 1872. This type of engine allowed to study new phenomena that until then had never even been hypothesized. Year after year, while this type of engine was “evolving” with the introduction of new models and designs that allowed ever more accurate analysis of the combustion processes, the parallel release on the market of the first simulation software gave the optically accessible engine a new role; the possibility of comparing experimental with simulated data regarding kernel growth, flame front propagation and consequently the burning turbulent velocity. Thanks to the constant innovation and upgrade of these software, combined with increasing accuracy of the measuring instruments, the research has received a strong push for the evaluation of the in-cylinder phenomena. For the work related to this thesis, more attention is given to the Bowditch design [11]. Introduced for the first time in the 1958 by F.W. Bowditch, the extended piston resembled design used by NACA [12], but the essential innovation was the presence of an inclined mirror (45 degrees to the vertical) at the base of the piston crown. This solution, combined with the quartz piston top, guaranteed the possibility to observe the inside of the combustion chamber without significant modifications to the original engine (an example was the absence of side windows as was the case of many other optically accessible engines at the time). The quartz disk was bonded to the piston seat using a high-temperature epoxy adhesive to resist the high thermal stress due to the combustion processes. However, the main issue of the Bowditch extended piston design concerned the excessive oil leakage past the valve guides. Due to these leaks, there was the eventuality of fouling the quartz on the piston top and consequently degrading the quality of visualization of the combustion

chamber. This problem was resolved with the introduction of specific valve stem seals. A similar issue was linked to the oil coming up from the crankcase and it was resolved with the introduction of special ring-pack. Finally, it is necessary to make a consideration regarding the fact that each optically accessible engine has undergone specific modifications; therefore, each engine of this type has a unique design and consequently this leads to difficulties in the comparison of the results obtained in different laboratories. Figure 1.5 illustrates the Bowditch extended piston design.

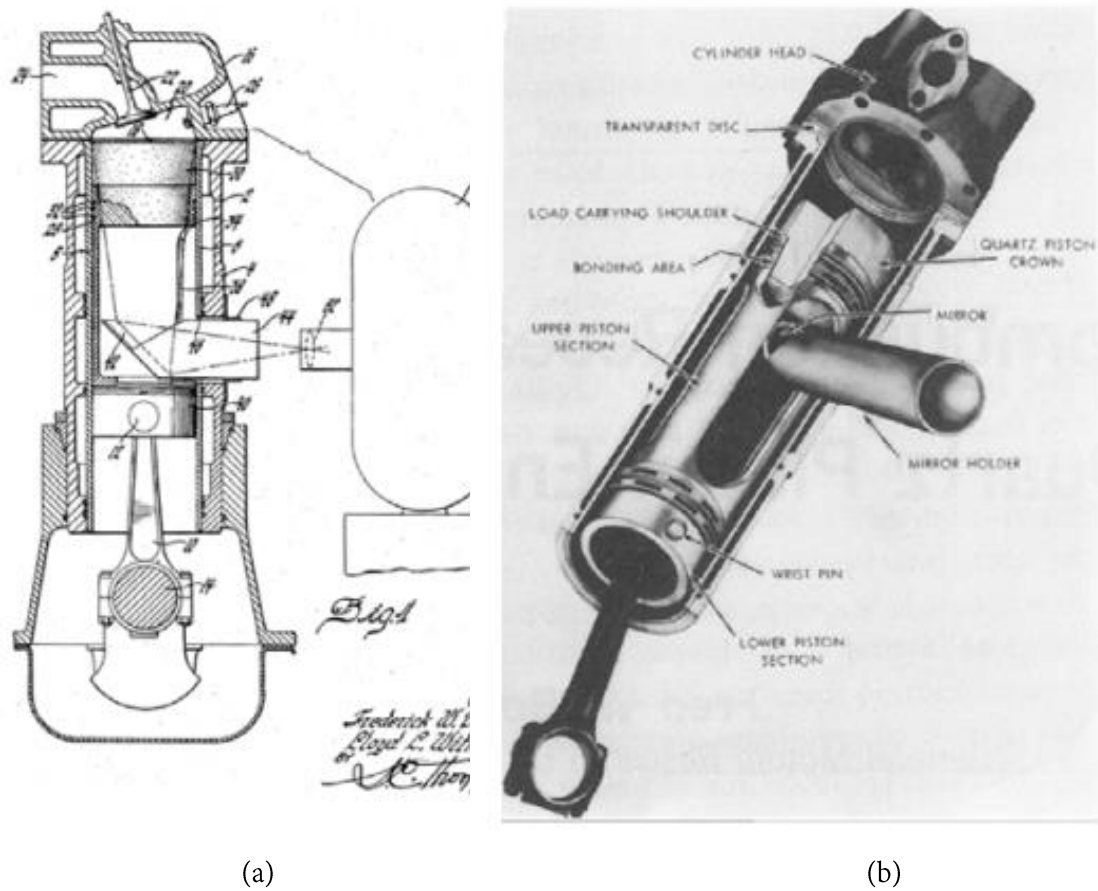


Figure 1. 5, (a) Schematic diagram of Bowditch's slotted, extended piston design from [11],

(b) 3D visualization from [13].

1.2 Cycle to Cycle Variability and Flame Kernel Growth

For many years, engine designers have been trying to reduce the instability of the combustion process in ICEs. The reduction of cycle-to-cycle variability (CCV) is a prerogative for increasing the efficiency ICEs and consequently reduce fuel consumption. Many studies [14-22] have investigated this phenomenon, but the available information regarding the causes of CCV are relatively limited and they are difficult to compare due to the differences between the optical research engines used or varying methodology. The main problem with the study of the cycle-to-cycle variability is its stochastic nature that reveals a random variation for each cycle. Therefore, there are several causes at their origin: the turbulence related to the intake flow, air-fuel ratio equivalence, the recirculated quantity of exhaust gas, spark plug orientation and many others of minor entity. The variations of these quantities are strongly related to the kernel growth; as demonstrated in [14,15] it is responsible of more than 50% of CCV. The CCV reduces the output power, in fact it is estimated that with a drastic decrease of cycle-to-cycle variation the output power and fuel consumption reduction can be improved by about 10%, [16]. This phenomenon becomes relevant for lean air-fuel mixtures [17] and consequently it is possible to observe an important increase of vibrations and noise. The main factors that determine the levels of CCV can be identified by applying a 0D/1D modelling approach [18]. The first influence is related to the variations of mean flow (hence, the in-cylinder turbulence) across the combustion chamber; in fact, through the optimization of tumble and swirl motions can reduce CCV by up to 66%. The second most important factor is linked to the equivalence ratio; without the variations of mixture composition the CCV can be reduced by up to 13.7%. The latter factor is related to the flow angle. The impact on the CCV of this parameter is reduced to 3.8%. The authors; in [19], studied the effect on the flame kernel growth and consequently the CCV for three spark plug orientations with two different electrodes designs in an optically accessible single-cylinder engine. The two spark plugs used feature respectively a “Double Fine Wire” and “Oval-J” designs, (Figure 1.6). The authors divided the results obtained in two groups, A and B, where for the first group the initial flame kernels were located to the exhaust side (in concurrence to the designed tumble design) while for group B the flame kernels were located to the intake side, opposite to the designed tumble direction. The results of group A showed that for the crossflow configuration the

flame kernel propagation is faster for each spark plug design (90° for Double Fine Wire and 100° for the oval-J, figure 1.7) while the counter-flow is the “slowest” configuration. Group B showed instead that there is no significant advantaged for each orientation (the oval-J spark plug for the 0° index orientation produces fastest propagating flame kernels).

For the work carried out for this thesis, the optically accessible engine used has already been object of many studies. In the papers [20,21], the authors reported the effect on the flame kernel displacement and dimension of the arc between the two electrodes for many operative conditions including the variation of engine speed and Air-Fuel ratio (AFR). Among the main conclusions, the authors noted that there is the possibility to use leaner mixture for low engine speed, due to the fact that lower rotational velocity featured higher stability of the combustion process. Another evidence is given by the analysis of linear correlations between mean piston speed and COV_{IMEP} that has revealed that the chemical kinetics part also has a determining role in this sense. The analysis of the flame kernel and relationship with the air-fuel ratio was studied in [22], where the connection between the level of cyclic variability and Air-Fuel ratio using a crank angle resolved method is explained. CCV was measured with the evolution of IMEP and peak pressure for each engine cycle and it was demonstrated that there is a strong correlation between the IMEP and the first phases of combustion process (the range examined was up to 5% of MFB), practically when the flame kernel is taking form. After these considerations, it is quite evident that there is a the need to continue to study the phenomena underlying the cyclic variability to improve the combustion process. Specifically, thanks to the similarity of the studies (in terms of purpose) performed in [19], this thesis aims to enrich and compare the results obtained with those already published in this specific research field.

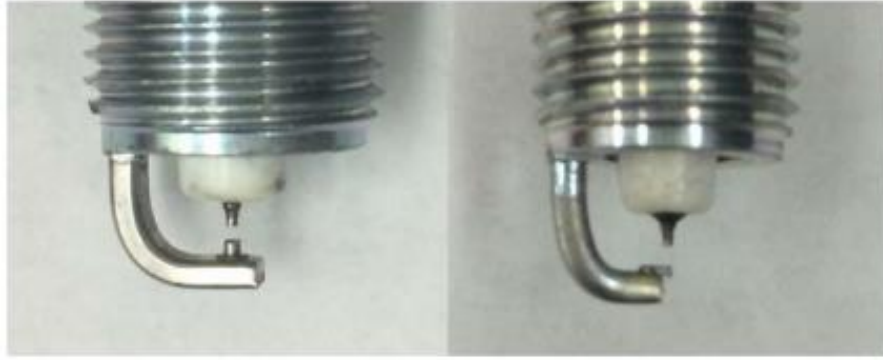


Figure 1. 6, Left: Double Fine Wire spark plug, Right: oval-J spark plug [19].

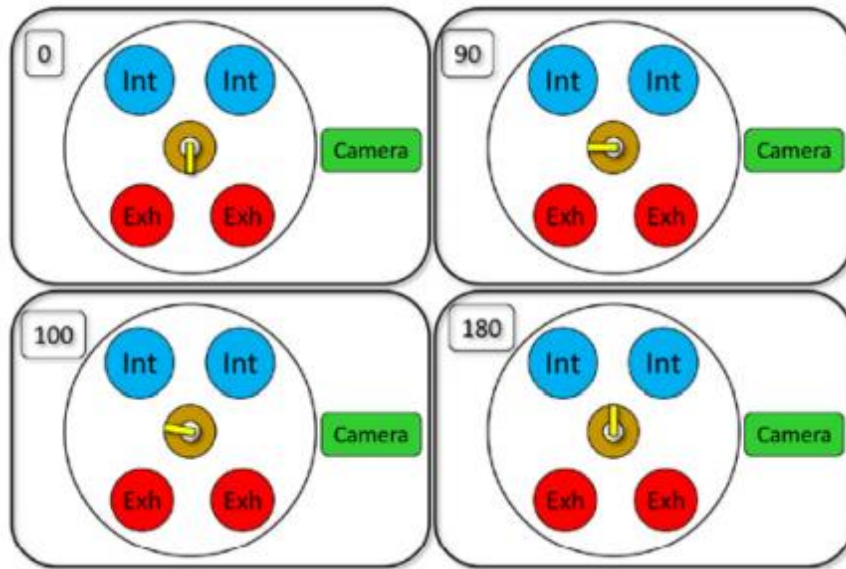


Figure 1. 7, On the top, from left to right: Counter-flow, Cross-flow, on the bottom: Cross-flow (for the oval-J this configuration is set to 100° respect to the vertical), Uniflow [19].

1.3 Homogeneous charge injection strategy

The combustion process in a Spark-Ignition (SI) engine is known as pre-mixed turbulent combustion [17] and the heat release rate (HRR) is strongly related to the turbulent burning velocity. The latter is a function of the laminar burning velocity which in turn depends strongly on the AFR, (figure 1.8). What has been said is related to what was anticipated in the introduction paragraph, or the development of GDI technology that has allowed the implementation of various strategies of injection. In this thesis the attention will be focused on the homogeneous charge injection strategy. Therefore, in a SI engine, to obtain a homogeneous mixture it is necessary to start the injection long before reaching the firing top dead centre, TDC [23]. This large advance is needed to give the time to the injected fuel to completely breakup (the phenomenon that leads the flow of fuel to crush the droplets into smaller ones), vaporize and mix with the air flow coming from the intake manifold. Fuel delivery during the intake stroke is generally employed, to ensure high velocity and turbulence. Normally this type of strategy is used for operative conditions related to mid or high level of engine load. In these cases, stratified operation is not optimal due to possibility of presence of overmixed zones, that can promote the formation of UHC, and undermixed regions (for example near the spark plug electrodes) that increase the PM emissions [8]. However, if the stratified strategy is not feasible, the possibility of using lean Air-Fuel mixtures is limited. Looking at these constraints, it would appear that the homogeneous strategy does not have margins of improvement in terms of fuel consumption. Nonetheless, researchers are seeking ways to find out how this operative condition can be optimized. In addition to the advantage related to the reduction of charge temperature during the vaporization phase, there is also the possibility to split the injection [23]. In fact, one of the main downsides of this approach is due to the long duration of the injection, to accommodate the high load operative conditions, that causes the over penetration of fuel jet and consequently the impingement on the piston crown. In fact, despite the increased pressure of a DISI system (that allows to have smaller droplet size and consequently good atomization), the long duration of injection increases the spray momentum and makes the fuel droplets travel across the combustion chamber. More accurate studies have been carried out in [24,25] for the evaluation of the effect of split and delayed injection on the cycle-to-cycle variation, PM, CO and UHC emissions. In this study, the injection strategy was

maintained as a single event per cycle approach. The start of the injection was set at 300 degrees of crank Before Top Dead Center (BTDC) for all cases performed in the laboratory. This value ensured that a homogeneous mixture was achieved at the spark timing angle.

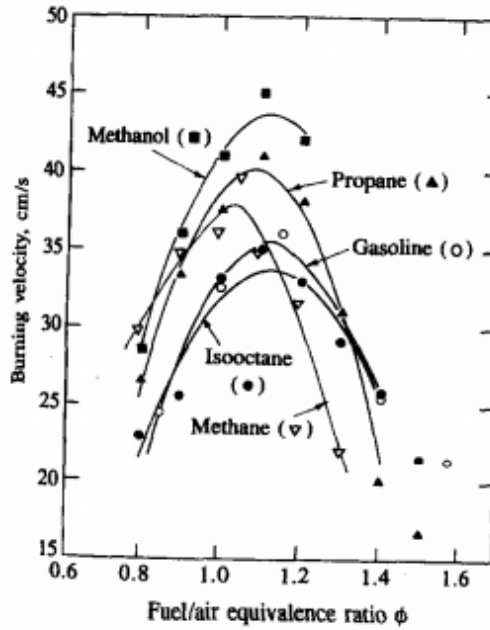


Figure 1. 8, Laminar burning velocity for several fuels as function of equivalence ratio, [17].

1.4 DISI Mixture Formation and Control

The combustion system of a DISI engine is usually classified into three categories depending on the mixture control mechanism: wall-guided (WG), air-guided (AG) and spray-guided (SG), [26].

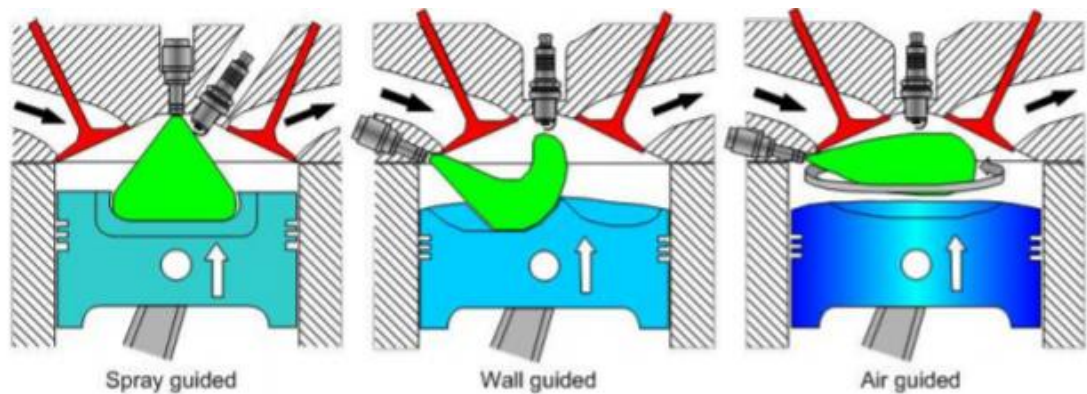


Figure 1. 9, Different types of DISI combustion system [26].

In the WG and AG mixture control configurations the injector is placed near the cylinder liner, away from the spark plug, so the fuel spray is directed toward the latter. The fluid motion in the combustion chamber is defined by the piston bowl in the WG configuration or by the air flux for the AG system. In the WG configuration the cavity on the piston top has the role of directing the fuel spray toward the spark plug to create the condition of local rich air-fuel ratio (this becomes important during the stratified charge operative condition). For the last configuration (SG) the injector is fitted near the spark plug, so this arrangement allows to obtain a strong coupling between fuel preparation and fuel injection [27]. As disadvantages of these configurations, the WG combustion system causes an increase of fuel deposits and therefore higher UHC emissions. The AG mode offers a more complicated air-fuel ratio control and distribution in the combustion chamber, and finally the SG ensures to achieve better mixture control toward the spark plug but there is the necessity of elevated turbulence inside the combustion chamber to support flame front propagation [28]. The comparison between DISI SG and WG configurations shows that for the SG combustion phasing losses are lower with a higher combustion efficiency and therefore improved fuel economy. However, the most part of these advantages are related to the possibility of adopting the stratified charge strategy, and as previous mentioned, it is possible to adopt this strategy only in low load conditions due to the issues linked with the fuel deposits and PM emissions. For the

work performed in this thesis, the optically accessible engine featured a wall-guided injection system that is representative of a large segment of the automotive engine design.

1.5 Motivation and Research Goal

Talking about the motivation and research goal behind this thesis, it is related to the understanding of in-cylinder processes, with complex dependencies between phenomena that are related to flow, thermal and chemical engineering. As previously mentioned, the main issue linked to this specific research field is the absence of a common database. Therefore, the purpose of the present work is to investigate the process of flame kernel formation and flame front propagation to compare the results obtained with the already existing information related to the studies carried out in [19]. In the latter, the authors have studied the effect of different spark plug orientation on kernel formation and flame front propagation for various operative conditions in an optically accessible GDI engine. The similarity of the mentioned work (in terms of goal) with the one performed in this thesis allows to enrich and validate this research field. Thanks to the many experimental tests carried out in the laboratory it was possible to accumulate a considerable amount of output data and these thermodynamic data, combined with the optical analysis, could be used for future implementation in a CFD model. It will allow proper calibration and provide more accurate knowledge of the phenomenon of flame front propagation, starting with the kernel formation. Furthermore, the research goal is strongly related to the improvement of combustion stability in lean conditions with the evaluation of cycle-to-cycle variability and related parameters. Particular attention is given to the operative conditions with a set engine speed of 2000 rpm for the spark plug configurations: Uniflow, Crossflow and Counterflow. Finally, for a better understanding of in-cylinder phenomenon, the observed flame behaviour are linked to the tumble characteristics.

Chapter 2

Experimental Setup

2.1 Engine System Setup

In this paragraph the engine setup and testing procedures are explained. The measurements were carried out in one of the laboratories of the “Istituto di Scienze e Tecnologie per l'Energia e la Mobilità Sostenibili” (STEMS-CNR) in Naples, on an optically accessible Direct-Injection Spark-Ignition (DISI) single-cylinder four-stroke engine. Originally, the engine head was built for a 1.4 litres Fiat 4-Cylinder turbo-charged unit in line; it was appropriately modified for the optical investigations. The engine is equipped with four-valve pent-roof head, while the crankcase is designed for a single-cylinder that features a Bowditch extended piston design, which combined with the quartz section on the piston top allows the combustion chamber to be visible through the piston crown. Table 2.1 shows the engine specifications and the valves timing setup, while figure 2.1 the schematic configuration [29].

Displacement	399 cm ³
Stroke	81.3 mm
Bore	79 mm
Connecting Rod	143 mm
Compression Ratio	10:1
Number of Valves	4
Exhaust Valves Open	153 CAD ATDC
Exhaust Valves Close	360 CAD ATDC
Intake Valves Open	363 CAD BTDC
Intake Valves Close	144 CAD BTDC
Fuel Injection System	DI-WG
Start of Injection	300 CAD BTDC

Table 2. 1, Engine Specifications.

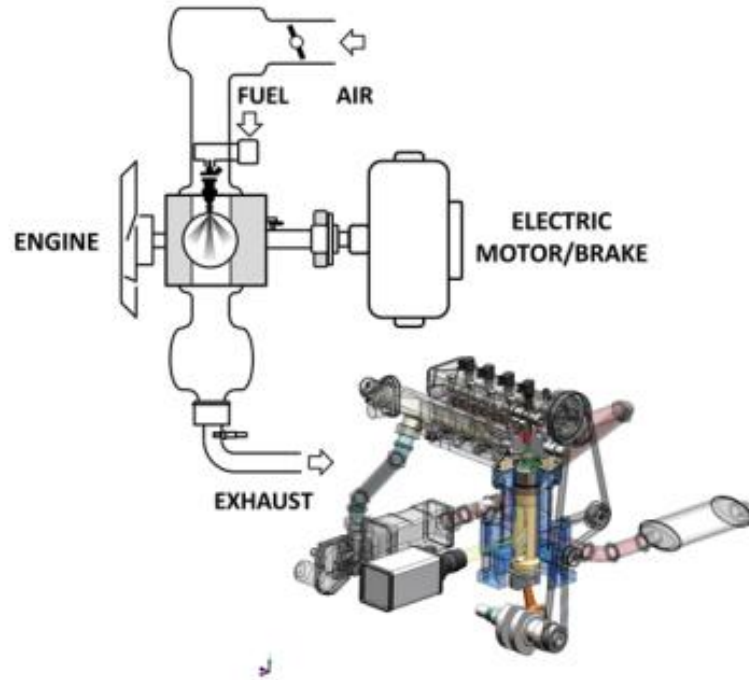


Figure 2. 1, Schematic representation of the experimental setup [29].

A 50-kW dynamometer allowed to maintain a constant engine speed for different load levels load with an error of ± 20 rpm. The crankshaft was connected to a reversible electrical motor with an elastic coupling. Mixture formation occurs in a wall-guided (WG) mode, with fuel delivery through a six-hole injector manufactured by Magneti Marelli (diameter of holes of 0.140 mm and solenoid actuation, figure 2.2) fitted between the two intake valves.



(a)



(b)

Figure 2. 2, (a) Magneti Marelli Injector, (b) Injector nozzle.

Synchronization of various control triggers for ignition, injection and camera recording start was achieved using the optical encoder mounted on the crankshaft as an external clock connected to

an AVL Engine Timing Unit (AVL, Graz, Austria). The AVL ETU (figure 2.3) is a pulse generator that synchronizes the encoder with the engine cycle and the input command used for this operation are the Trigger and CDM (Crank Degree Medium) from the encoder. The Trigger indicates the TDC position, the second one the pulses for each angle. The injection system is controlled by an additional electronic control unit (figure 2.4), where the start and duration of the injection event are fixed using the digital input signal coming from the ETU. Apart from the output signal that drives the injector, the injection control unit also maintains a constant pressure (100 bar) in the fuel rail.



Figure 2. 3, AVL ETU pulse generator.



Figure 2. 4, Injection control unit.

The common-rail pipeline for the injection system was modified to enable only one of the four injectors and subsequently tested to ensure that there were no leaks through the seals. The injection pressure was monitored using a piezoelectric transducer flash-installed at one of the rail's extremities. The fuel supply system features a continuous-delivery system; therefore, it is comprehensive of a low-pressure pump which feeds the high-pressure pump. Regarding the Start of Injection (SOI), for all the cases the value reported in the Table 2.1 was used to guarantee the

condition of homogeneous charge. The spark plug mounted in the combustion chamber has the “classical” J-type electrode design (Bosch - YR7LEU) [30]. In this thesis the spark plug electrodes orientation was studied in three different configurations: Uniflow, Crossflow and Counterflow [19], where for the first the ground electrode acts as “shield” for the flow coming from the intake valves. The second one features the ground electrode rotated by 90 angles degree respect to the previous position, while for the last the position is opposite respect to the the Uniflow configuration. A peculiarity of the Uni and Counterflow configurations is the advantage linked to the fact that it allows to obtain a symmetric geometry in the combustion chamber. Therefore, including this configuration in a Computational Fluid Dynamics code, it is possible to discretize only half combustion chamber, so the numerical solution requires half the time. In figure 2.5 the three configurations above described are showed.

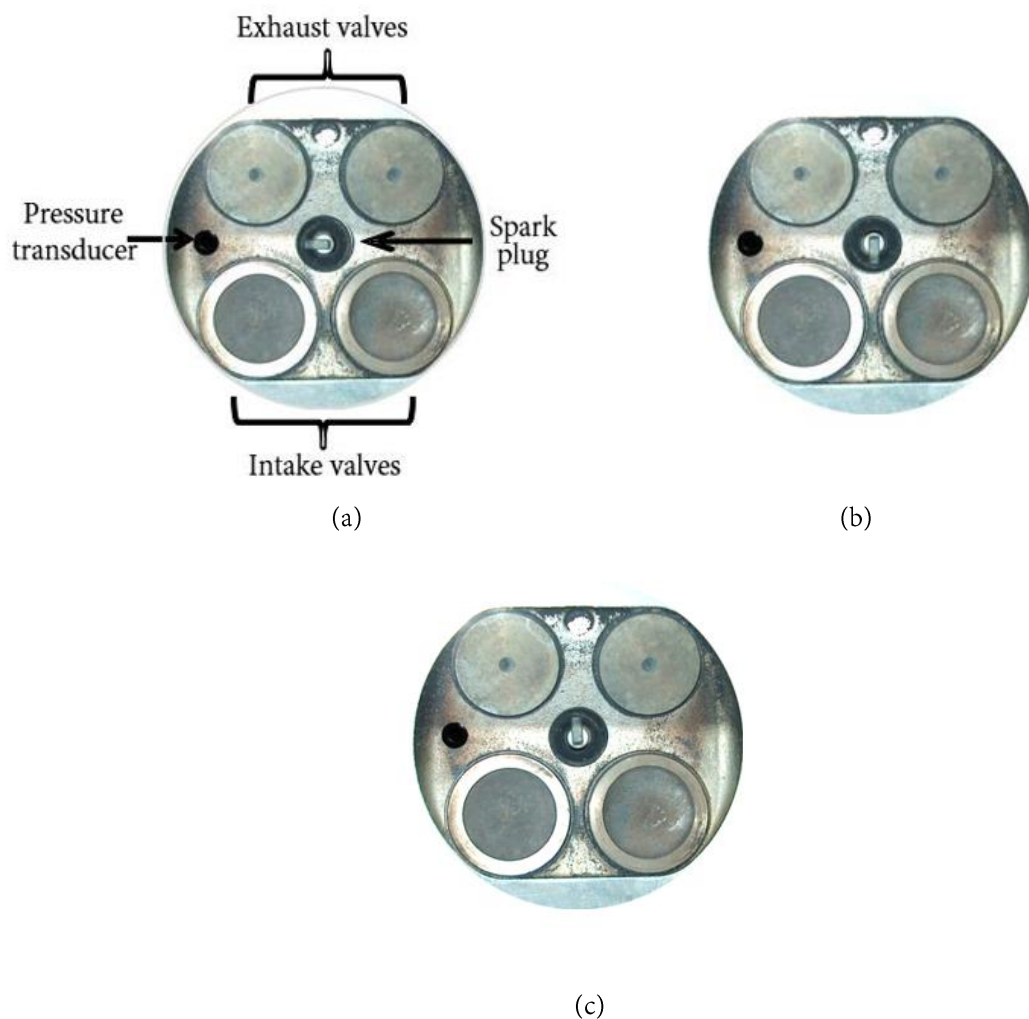


Figure 2. 5, (a) CROSSFLOW configuration, (b) UNIFLOW configuration, (c) COUNTERFLOW configuration.

Air- fuel ratio was monitored by two different devices. The first is a UEGO (Universal Exhaust Gas Oxygen) sensor with an accuracy of $\pm 1\%$ that is fitted close to the exhaust manifold. This sensor has a measurement range of 0.55-1.2 λ . The second device is located further down the exhaust line; it is a AVL DITEST GAS 4000, and it is also needed to study the composition of the combustion gas. The AVL device is not influenced by the exhaust backpressure (mainly due to the fact that it features a sampling pump, [31]) and it measures the air-fuel ratio by applying the Brettschneider's equation [32];

$$\lambda = \frac{CO_2 + \frac{CO}{2} + O_2 + \left(\frac{H_{CV}}{4} \cdot \frac{K}{K + \frac{CO}{CO_2}} - \frac{O_{CV}}{2} \right) \cdot (CO_2 + CO)}{\left(1 + \frac{H_{CV}}{4} - \frac{O_{CV}}{2} \right) \cdot (CO_2 + CO + K_1 \cdot HC)},$$

where λ is the relative air-fuel ratio and, CO_2 , CO , O_2 and HC the species concentrations with the same unit (only HC needs to be converted from ppm to percentage using the relation [ppm/10000]). H_{CV} is the hydrogen to carbon ratio (1.73 for gasoline), K water gas equilibrium constant, O_{CV} the oxygen to carbon atomic ratio and K_1 the flame ionization detector FID/NDIR conversion factor. Regarding emissions measurement, the principle is based on the non-dispersive infrared (NDIR) for CO , CO_2 and HC concentrations, and electro-chemical for NO_x and O_2 . The AVL equipment features an overall accuracy of around 3% [33], the error may increase with the measured value, but in any case, not more than 5%. The fuel used is a common gasoline with a RON (Research Octane Number) of 95 [34]. Regarding the intake pressure, it was maintained on the same level for all cases analysed (1 bar, to recreate in the laboratory the usual operative conditions for an automotive engine) and the air-fuel ratio was varied from stoichiometric to lean blends. The regulation of these parameters was made possible using a dedicated control system for each component. The engine speed was set by regulating the electrical motor speed with a feedback control loop capable of switching between motor – generator regimes. Acting on the throttle valve opening level it was possible to set the intake pressure, while for the variation of AFR the (DOI) was increased or reduced. The intake air temperature was around 300K and monitored

by a thermocouple placed in the intake manifold. A Bosch absolute pressure sensor was used for measuring the intake pressure with an accuracy of $\pm 1\%$. Oil and water temperatures were managed and regulated by a thermal conditioning system comprehensive of an electric heater and a heat exchanger. It permitted to maintain a wall of the cylinder liner temperature between 330-335K. Under normal conditions for the engine, it was necessary to maintain a moderate temperature to protect the elongated piston-bore assembly that features high tolerance specific for optical engines. Finally, a transducer (AVL GH12D) was used to measure the in-cylinder pressure with an accuracy of $\pm 1\%$ and resolution of 0.2 CAD. Piezoelectric pressure sensor working principle is based on the electrical charge output of quartz crystal under mechanical load. Therefore, the output charge is proportional to the pressure difference applied, and it is converted to a voltage signal by a charge amplifier (AVL FI Piezo-Amplifier). The pressure trace used for the thermodynamic analysis, for the different cases, was obtained as an average of 200 recorded cycles. Figures 2.6 and 2.7 show the different components of the experimental setup.

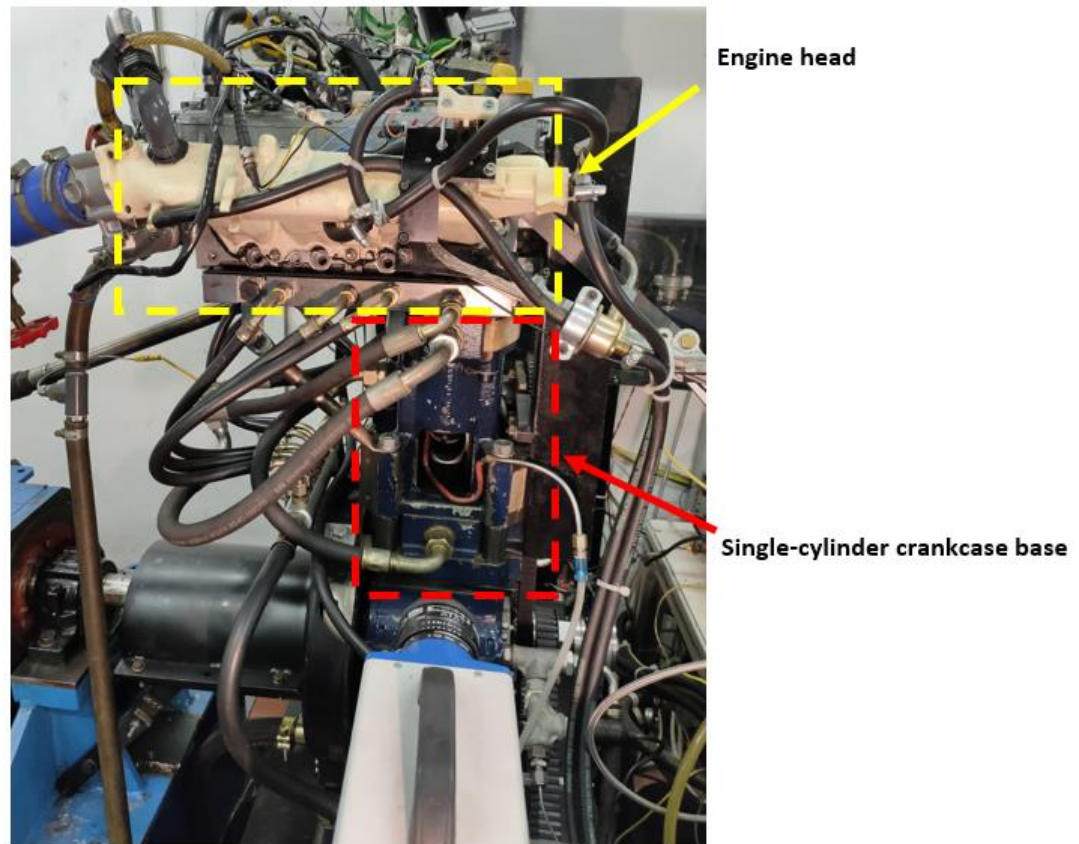


Figure 2. 6, Engine experimental setup.

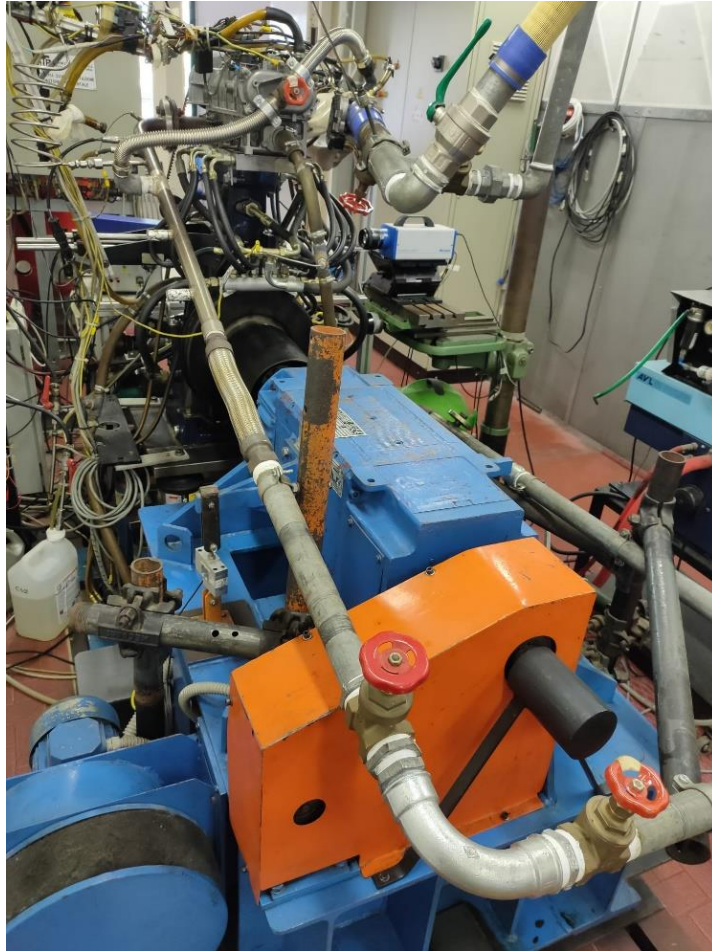


Figure 2. 7, Electric motor/brake coupled with the engine (49.7 kW power, 230 Nm maximum torque).

2.2 Optical Setup

A Bowditch extended piston replaces the original metal piston for this research engine to allow the combustion chamber to be visible through the piston crown. Thanks to a mirror, inclined at 45 degrees with respect to the vertical, fitted at the base of the elongated piston, it is possible to observe and study the phenomena inside the combustion chamber during all the firing phases. Therefore, this kind of solution involves the use of a piston whose head section is replaced by a quartz window and consequently the quality of recorded images is strongly influenced by its degree of cleaning. So, it is recommended to acquire the necessary optical data with the minimum number of operative tests but even with these precautions the piston top needs to be removed and cleaned after a certain number of tests performed. The piston quartz window ensured a field of view of 62 mm in diameter, corresponding to 60% of the piston cross section. Slotted graphite piston rings were used to provide oil-less lubrication with uninterrupted bronze–Teflon rings used for sealing. The Bowditch piston produces a lower effective compression ratio and in addition the bowl of piston results flat. Compared to the original piston used in the four in-line engine, the resulting geometry can be considered as representative of automotive applications. The Bowditch piston involves the use of three stock piston rings (figure 2.8) and to reduce the heat transferred to the quartz, and consequently its overheating, normally the time of tests in the laboratory cannot last more than a few minutes. Due to these numerous mechanical limitations, laboratory tests have sometimes been repeated for a more accurate analysis of data. A schematic representation of a Bowditch extended piston design is reported in the figure 2.9 [35].



Figure 2. 8, 3D render visualization of piston crown.

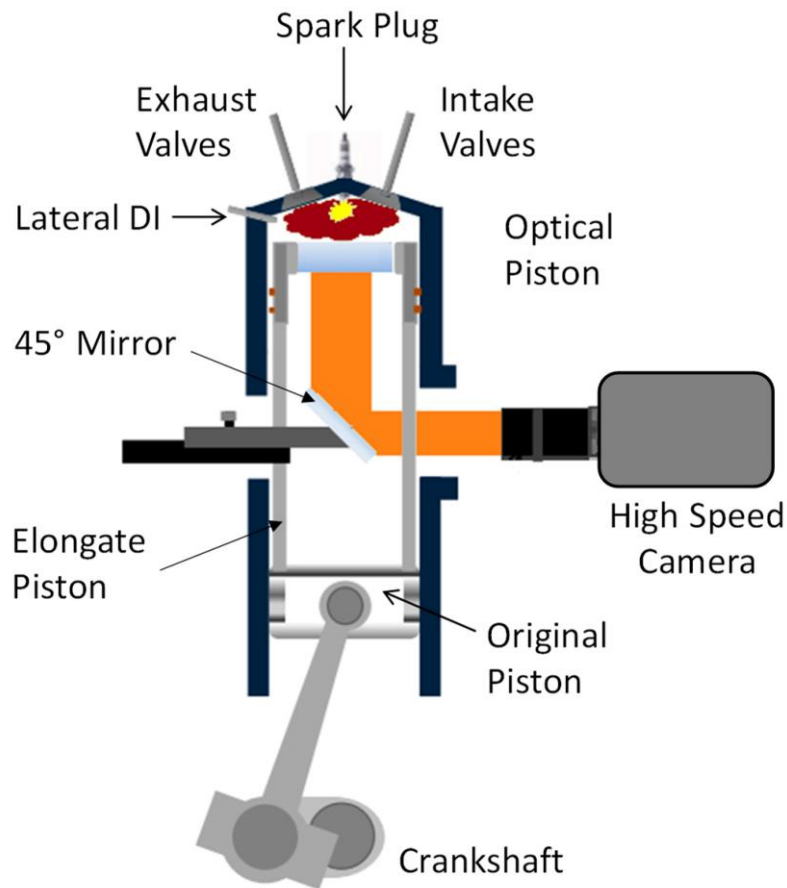


Figure 2. 9, Schematic representation of a Bowditch extended piston [35].

To avoid excessive thermal expansion of the piston top, the housing of quartz window is made of steel (ck45). Finally, thanks to the presence of two balancing shafts in the crankcase, the vibrations which normally would occur for a common single-cylinder engine, were significantly reduced. Flame front propagation was investigated through cycle resolved digital imaging. Acquisition of images was carried out with a high-speed CMOS camera (CamRecord 5000, 8-bit, $16\ \mu\text{m} \times 16\ \mu\text{m}$ pixel size by Optronis, Kehl, Germany, figure 2.10 [37]) equipped with a 50 mm Nikon objective. The camera was set in full chip configuration with a resolution of 512×512 pixel and acquisition speed of 5000 frames per second, with an exposure time of $167\ \mu\text{s}$. The f-stop of the objective was set at 2.8 to improve the signal-to-noise ratio without extensive saturation effects. Therefore, for the set-up allowed the images were recorded with a dwell time of 2.4 CAD at 2000 rpm and a spatial resolution of 0.19 mm per pixel.



Figure 2. 10, High-speed camera CMOS, CamRecord 5000 by Optronis [37].

For each test performed in the laboratory, the number of cycles recorded by the high-speed camera was about 10 consecutive cycles out of a total of 200 that were acquired for each condition. Each sequence featured 25 consecutive frames with an interval of 2.4 CAD (0.2 ms) starting from the spark timing as reported in figure 2.11.

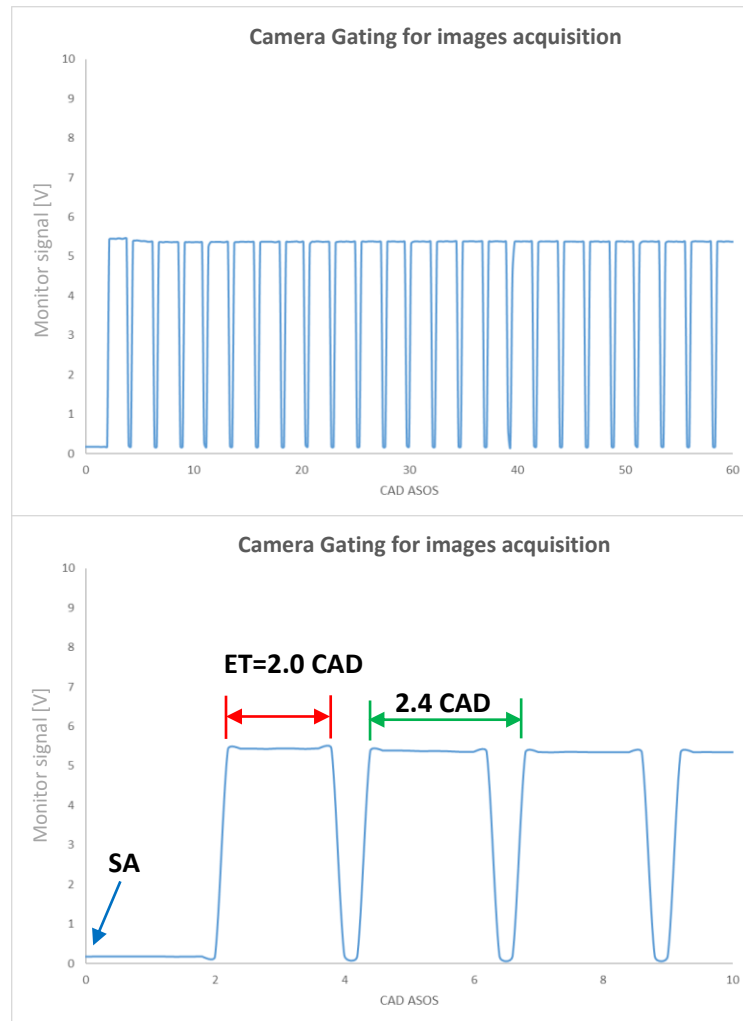


Figure 2. 11, Camera gating for acquiring 25 images per cycle.

Although deriving quantitative information about the kernel from the cycle resolved images seems in principle quite a simple task, in reality the uncertainties related to the presence of the spark plug and the possible obstruction of the actual flame kernel must be carefully considered. In fact, in this phase the kernel tends to be hidden by the ground electrode, so the software is cannot “see” anything and returns a frame without any object visualized. Therefore, it is intuitive to note the the importance of the subjective “sensibility” imposed during this type of analysis and the subsequent choice of parameters when using the NI Vision software to optimize the recorded images.

Chapter 3

Procedure and Measurement Methodology

3.1 Thermodynamic Analysis

The signals recorded by the acquisition system were: in-cylinder pressure, intake pressure, equivalence ratio, signals of primary and secondary current of the ignition system. The thermodynamic analysis started from the in-cylinder pressure analysis; to do this a dedicated script built in National Instrument LabView software was used. The latter was necessary to summarize the information coming from 200 cycles in a single average signal with the steps reported in figure 3.1.

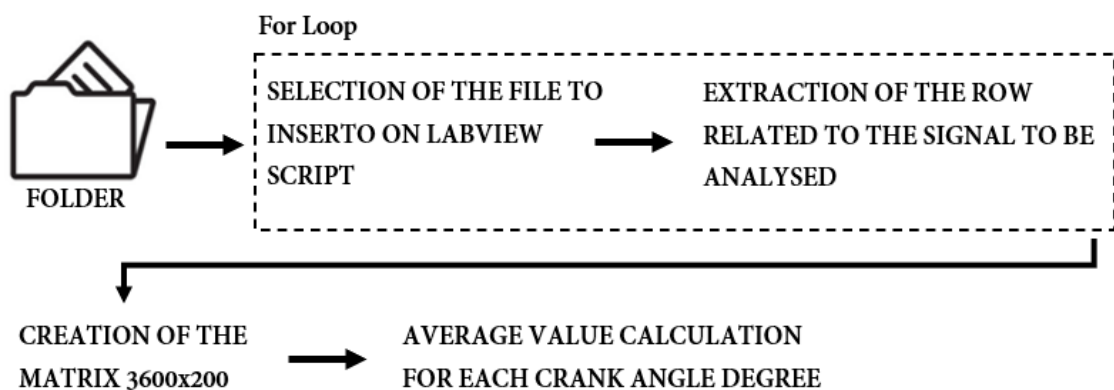


Figure 3. 1, LabView script for in-cylinder pressure analysis.

However, before plotting the average in-cylinder pressure signal it is necessary to equalize the value of the latter at 180 CAD BTDC to the intake pressure average signal (obtained with the same procedure as for the in-cylinder pressure). This correction is necessary due to the measurement principle (the in-cylinder pressure is calculated as an increment, so a referring point must be defined). Therefore, this correction is performed using the measured pressure in the intake manifold at 180 CAD BTDC point. After this step, it is possible to study and compare the average pressure traces for each case that was analysed. The work carried out in this phase provides the comparison of the results for different values of AFR, spark plug orientations and Spark Advance (SA), to study which parameter had a significant effect on CCV. One of the first parameters

investigated was the Indicated Mean Effective Pressure value, IMEP. As a first step, to calculate these parameters the cylinder volume is also required. Therefore, the first step was to obtain the clearance volume calculated with the compression ratio and displacement values.

$$V_c = \frac{V_D}{(CR - 1)}$$

The equation reported above is simplified as it does not take into account the crevices volume and the variation of the compression ratio due to the elongated piston. For this reason, a thermal analysis was carried on the engine to verify the expansion levels of components during the motored and firing operative conditions. Therefore, the in-cylinder free volume for any crank angle degree can be obtained with the relation:

$$V = V_c + \frac{\pi B^2}{4} * (l + a - s)$$

where “B” is the bore, “l” the connecting rod length, “a” the crank radius and “s” the distance between the crank axis and piston axis, this last is given by:

$$s = a \cos \theta + (l^2 - a^2 \sin^2 \theta)^{\frac{1}{2}}$$

A schematic representation of cylinder geometry is showed in figure 3.2 [17].

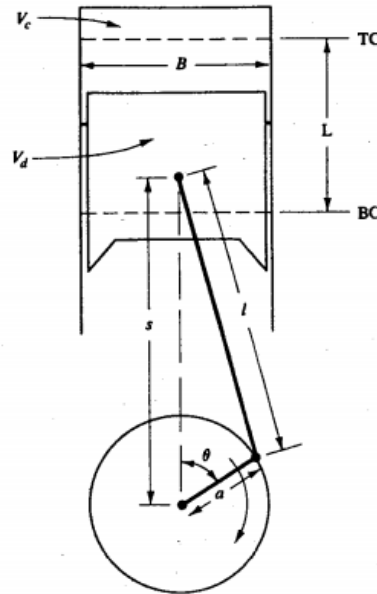


Figure 3. 2, Simplified cylinder geometry [17].

Now it is possible to calculate the W_{ci} (Indicated Work per Cycle) for each set of 200 cycles with the following relation [17],

$$W_{c,i} = \oint p dV$$

where “p” is the in-cylinder pressure measured in Pa and dV the instantaneous variation of the in-cylinder volume. Using a loop block in LabView it was possible to calculate this value for each of 200 cycles and consequently obtain the IMEP. The following equation allows to calculate the IMEP,

$$IMEP = \frac{W_{c,i}}{V_D}$$

where V_D is the displacement of single-cylinder engine, reported in the table 2.1. Consequently, it was possible to estimate the stability of combustion process, for the recorded series of data, with the evaluation of the related COV_{IMEP} . The latter was calculated for population of 200 values of IMEP with the relation below,

$$COV_{IMEP} = \frac{\sigma_{IMEP}}{\mu_{IMEP}} * 100$$

where the “ σ_{IMEP} ” indicates for the Standard Deviation, while “ μ_{IMEP} ” is the average value for the 200 cycles under analysis. A similar procedure was used for calculating the pressure peak reached in the combustion chamber and relative COV. With the referenced and averaged pressure signals, it is possible to calculate the Mass Fraction Burned values (MFB), and subsequently the Volume Fraction Burned, VFB. Heat Rate Release analysis was performed with a simplified approach of the first law of thermodynamics, using the equation,

$$dQ = \frac{\gamma}{\gamma - 1} * p * dV + \frac{1}{\gamma - 1} * V * dP$$

where Q is the net heat rate release measured in joule for crank angle, p the in-cylinder pressure in Pa, V is the instantaneous in-cylinder free volume in m^3 , and the ratio of specific heats γ was set to 1.35. Mass fraction burned (MFB) was calculated based on the integral of heat release,

$$MFB = \frac{Q_k - Q_{ST}}{Q_{EVO} - Q_{ST}}$$

Where subscript “k” is related to the current crank angle position while “ST” means spark timing crank angle and EVO the exhaust valve opening. With the MFB trend it is possible to divide the combustion into several stages and recognize the fundamental points of the process. The CA window that corresponds to 0–10% MFB is related to the flame development angle, 10–90% MFB corresponds to the rapid burning angle, and 0–90% MFB is the overall duration of the process. Finally, with the MFB50% point is possible to understand if, for the parameters set, the engine is close to working at the MBT condition, that is Maximum Brake Torque. Once MFB was known, it was possible to calculate the evolution of the burned volume fraction using the relation,

$$VFB = \frac{1}{\left[\frac{1}{MFB} - 1 \right] * \frac{\rho_b}{\rho_u} + 1}$$

where the density ratio between the burned and unburned mixture is set to 0.25 as representative of most of operative conditions of a SI engine [17].

3.2 Current Signals Analysis

Regarding the analysis of the current signals, it was carried out with the same logic seen for the in-cylinder pressure. The results obtained and reported in the dedicated chapter (Chapter 4) concern only the analysis of the discharge phase and related COV. Hence, the attention is focused on the current signal of the secondary circuit and not of the primary. It was found that the latter is not influenced by the phenomena in the combustion chamber (turbulence, different values of AFR, etc.). Therefore, the primary signal tends to remain stable for all the cases analysed. Finally, the attention is focused not only on different charge strategies for the primary circuit coil, but also on combined effect of the latter with the different orientations of the spark plug, with the purpose of analysing how it affects kernel formation (in terms of displacement) and flame front propagation (in terms of flame morphology). Figure 3.3 shows typical intensity current signal for the primary and secondary circuit.

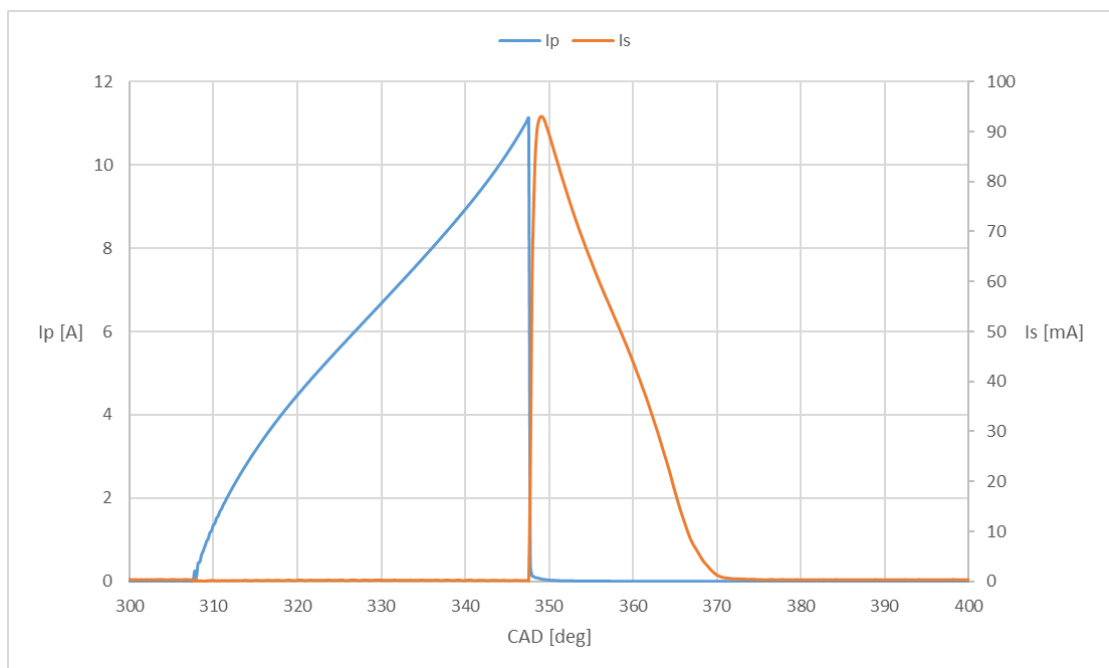


Figure 3. 3, Primary and secondary current intensity signals.

3.3 Optical Data Analysis

A script built in NI Vision for evaluating flame kernel displacement and flame morphology based on the recorded optical data was used. The steps behind each optical analysis are the same for all cases that were evaluated. The procedure starts with the use of processing function “Measure” that is needed to convert pixels in millimetres (the ratio is about 5.2 pixels per millimetre) and define the position of the centre of the spark plug for subsequent considerations on flame kernel velocity, displacement and flame front propagation direction. After this initial step, a circular mask was applied to the images coming from the sequences, so as to limit the investigated area to the quartz window fitted on the piston top and to cut light from reflections at the boundaries of the optical access. Note that the parameters used for these first two steps can change from a series of cases to another (for example two series of tests performed in different days) due to possible variations of the position of the high-speed camera with respect to the crankcase (e.g., for working on the engine). Next step the “Color Plane Extraction” function was used. In this way, by selecting the HSI command, it is possible to extract the three color properties: hue, saturation and intensity. After this phase it is possible proceed with improving image quality by employing the “Brightness” and “Look up table” functions. The first one, combined with the second, was used two times to have improved contrast, gamma and brightness (set respectively at 1.00, 53.30 and 128 for both functions repeated in the script) and subsequently a reduction of signal-noise ratio. Finally, a threshold level was applied to obtain binary images. The choice of the latter parameter is strongly linked to the user sensibility; in fact, defining a level of grey on a scale from 1 to 256 it is possible to indicate to the software when to “see” or not a determined pixel. Therefore, it is intuitive that setting a lower value of grey on the scale can be helpful for the analysis of the first stage of combustion process but not for fully developed flames; in fact for the latter many small objects that are not part of the flame front would form during the visualization phase, with the risk that the software confuses one of these “small objects” with the main flame area. This is a situation to avoid given that during the results export stage the software would save the objects coming from the signal-noise first, and not the main flame, with consequent errors on the successive analysis. Therefore, for the operative conditions with $\lambda=1.00-1.15$, the threshold was fixed at

33/256. Instead, for the cases with leanest AFR the grey scale was set at 24/256 so as to improve the image processing quality. Finally, using the “FFT filter” and “Advanced morphology” functions, it is possible to reduce the signal-noise ratio and fill any eventually holes in the foreground figures. Further clarifications are required for the FFT filter function, with respect to the “error” that occurs with the original frame parameters. The modality of filtration was set on “low pass” with a truncation level of 20% and it was observed that the error between the flame area morphology parameters (before and after the correction) is less than 2%. As the final steps of the procedure, the remaining functions that were used are linked to the necessity to save the information on flame kernel morphology. The sequence of steps applied for performing the analysis is illustrated in figure 3.4.

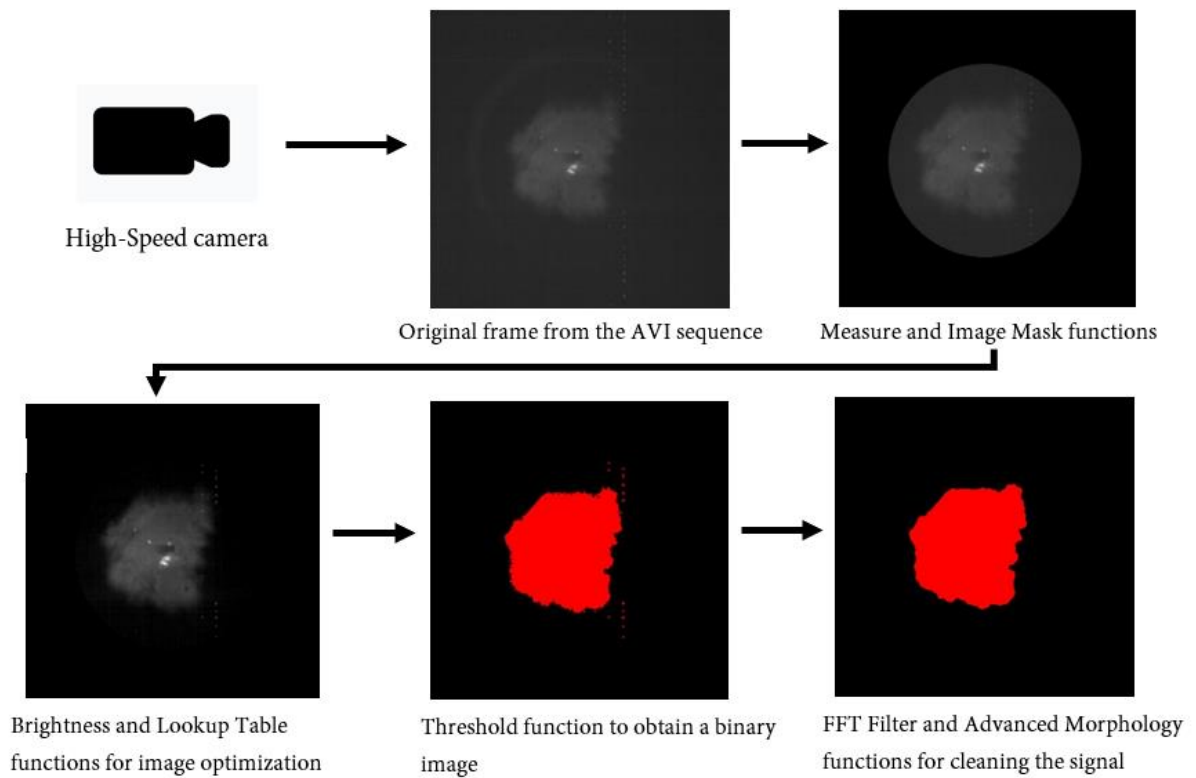


Figure 3. 4, Steps of the NI Vision script used for image processing.

Previous studies identified preferential directions for flame propagation, due to fluid motion phenomena (tumble and swirl) as well as temperature gradients and non-homogeneity of the mixture inside the combustion chamber [35]. To better characterise the previously mentioned effects, the “Max Clamp” specific function was added to the NI Vision script; this allowed the

evaluation of flame front propagation and whether there was a preferred direction. Therefore, knowing the temporal gap between each frame, the horizontal and vertical velocity were calculated, and the following equations were used to compare the trend on the two axes,

$$\frac{Intake}{Exhaust} = \frac{L_{Intake}}{L_{Exhaust}},$$

$$\frac{Left}{Right} = \frac{L_{Left}}{L_{Right}},$$

$$Clamp_x = L_{Left} + L_{Right},$$

$$Clamp_y = L_{Intake} + L_{Exhaust},$$

where, L_{Intake} , $L_{Exhaust}$, L_{Left} and L_{Right} indicated the position of extreme side of the flame area in each direction with respect to the spark plug. Figure 3.5 shows an example of comparison between two consecutive frames.

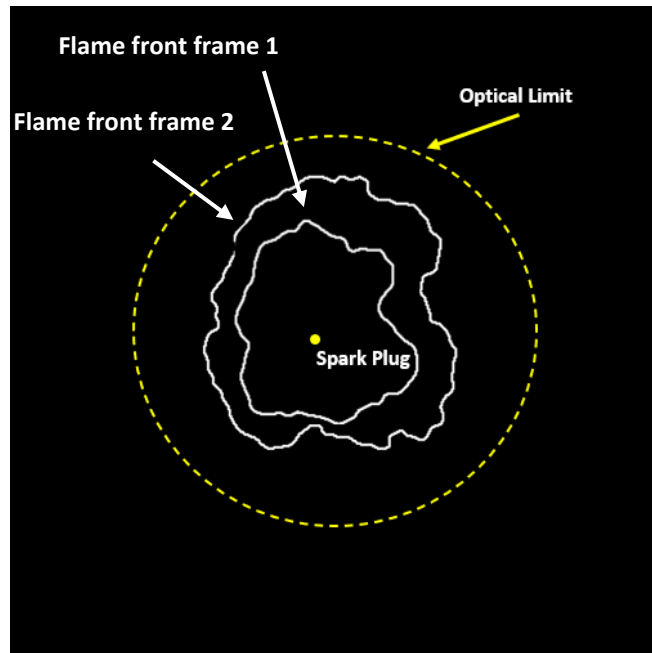


Figure 3. 5, Flame front propagation comparison of two consecutive frames.

Finally, to have a better understanding of the extent of cyclic variability recorded during the trials, it may be useful to show the parameters obtained with the NI Vision script. The dimensions reported in the table 3.1 are in pixels, except for the area; they are related to five frames, at the same crank angle degree, during five consecutive sequences for the same operative condition: $\lambda=1.15$, spark advance 12 CAD and wide open throttle.

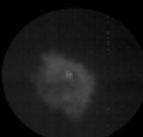

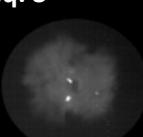

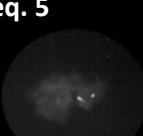
		Center of Mass X	Center of Mass Y	Perimeter	Feret Diameter	Area [mm ²]
Seq. 1		233.7	277.5	512.6	179.8	633
Seq. 2		261.5	235.1	450.0	143.3	377
Seq. 3		244.2	246.8	774.8	232.7	1423
Seq. 4		256.3	233.7	730.8	237.5	1268
Seq. 5		232.5	254.8	492.2	168.3	504

Table 3. 1, Flame area morphology parameters.

	CDM X	CDM Y	PERIMETER	FERET DIAMETER	AREA
Standard Deviation	11.6	16.0	133.5	36.9	423
Coefficient of Variation	4.7%	6.4%	22.5%	19.2%	50.2%

Table 3. 2, Standard deviation and COV of main parameters of flame area Morphology.

Observing the position of the center of mass, the cyclic variability is contained but the same observation is not valid for the parameters related to the area and its morphology. The latter show high cyclic variability, well beyond the error values due to the use of the previously mentioned filter function.

Chapter 4

4.1 Coil Charge Duration Analysis

Before proceeding with more detailed analysis of the results, it is necessary to make several considerations on the coil charge duration parameter and its effect on the flame kernel formation. Maintaining the Uniflow configuration of the spark plug, this parameter was varied from a minimum that ensured successful ignition to the maximum dwell time that was close to the peak current that could be achieved with the coil that was used. The related results showed that there was no clear and consistent trend in the thermodynamic and optical data. The primary circuit electric current signal showed the same trend for all the operative conditions set (evidently with lower peak current as coil charge duration as reduced), so attention was focused on the secondary current signal. Table 4.1 shows the parameters set for the investigation of the Coil Charge Duration are shown:

λ	Intake Pressure [bar]	Engine Speed [rpm]	Coil Charge Duration [CAD]	Spark plug Configurati
$\lambda=1.00$	1 (WOT operating condition)	2000	07-10-20-30-40	Uniflow
$\lambda=1.15$	1 (WOT operating condition)	2000	07-10-20-30-40	Uniflow
$\lambda=1.30$	1 (WOT operating condition)	2000	10-20-30-40	Uniflow

Table 4. 1, Parameters set for Coil Charge Duration investigation.

Spark Advance (SA) was fixed at 12 CAD for all the cases analysed. Furthermore, another difference can be seen by looking at the Coil Charge Duration value for the leaner mixture. In fact, for the latter the lower limit does not reach 7 CAD as with such a lean mixture and low intensity of spark misfiring events were detected. The reasons why the leaner mixture featured lower capability of generating a stable combustion process with a reduced Coil Charge Duration is related to the fact that in this operative condition the molecular density of the fuel between the two electrodes is low and therefore chemical reactivity is reduced. The secondary current signals are showed in figures 4.1, 4.2 and 4.3.

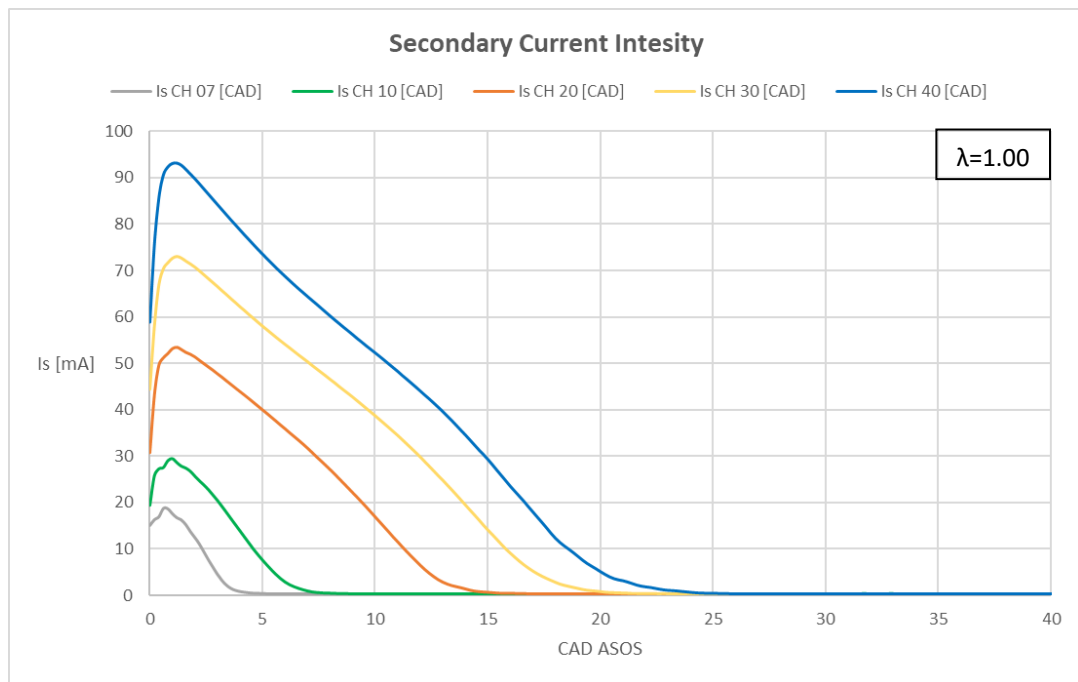


Figure 4. 1, Secondary current signal during discharge phase, $\lambda=1.00$.

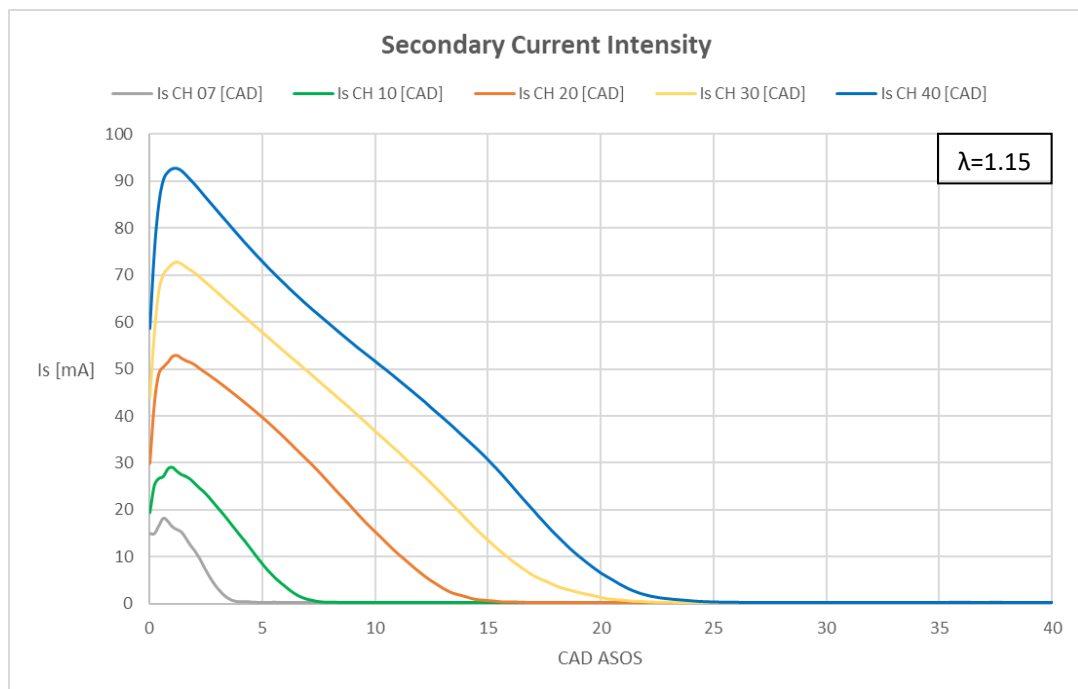


Figure 4. 2, Secondary current signal during discharge phase, $\lambda=1.15$.

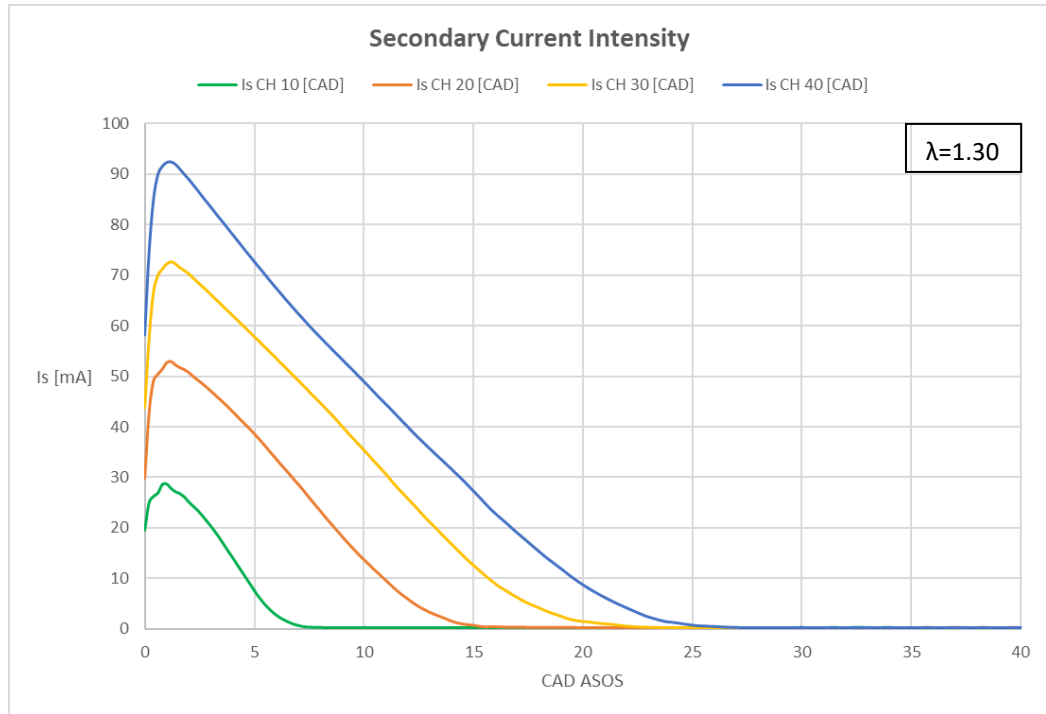


Figure 4. 3, Secondary current signal during discharge phase, $\lambda=1.30$.

The secondary current intensity signals show the same trend for all the air-fuel ratio levels examined. The fluctuations are very moderate and looking at the start of discharge phase for reduced Coil Charge Duration it is possible to observe how the trend tends to be slightly irregular. This phenomenon is linked to the fact that the stored energy in the primary circuit is low and the breakdown voltage that occurs between the two electrodes begins to become unstable. Practically, the engine is near the misfiring limit. More information can be obtained with the COV of signals calculated on an interval of 40 CAD starting from the spark ignition advance angle; this parameter is shown in figure 4.4.

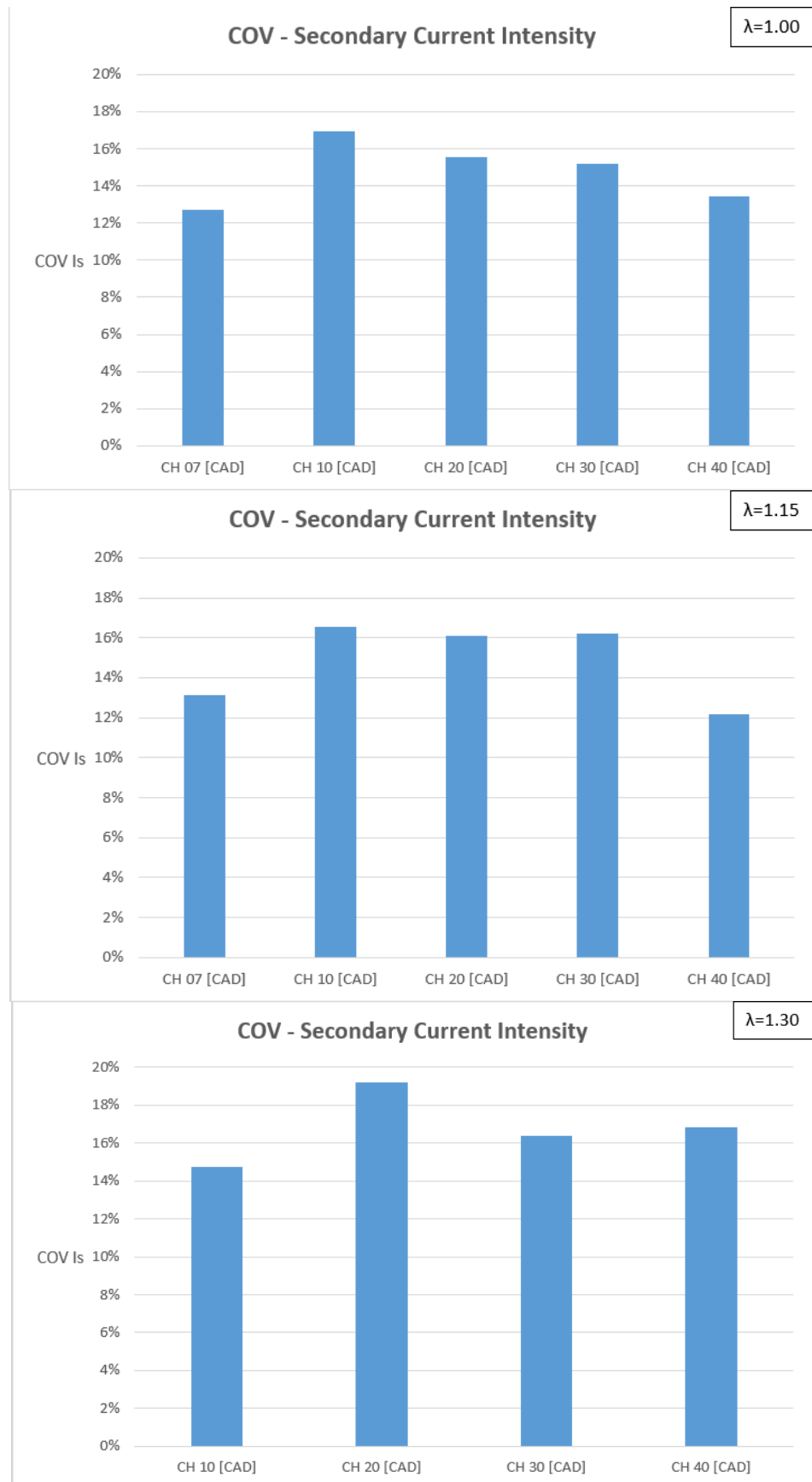


Figure 4.4, COV-Is for $\lambda=1.00-1.15-1.30$.

For the analysis of the COV-Is there is the necessity clarify the fact that looking at the above reported figures it seems that the lowest value of coefficient of variation is reached for the shortest Coil Charge Duration. As previously said, it is precisely in this condition that the engine is close to the no-spark condition. The phenomenon is linked to the fact that with such reduced spark intensity the average level of secondary current intensity is just enough to ensure ignition (In the interval of 40 CAD under analysis), there is little interaction with the fluid flow and consequently the COV tends to decrease. Hence, the reduction of COV-Is for the shortest Coil Charge Duration can be interpreted as the misfiring limit. After this clarification, as expected, it is possible to note that the average trend of COV-Is is slightly decreasing with the increase of Coil Charge Duration. This can be expected, given that more energy charged to the coil results in stronger spark and thus more stable ignition.

More detailed analysis of the combustion characteristics was performed based on in-cylinder pressure traces, IMEP and COV_{IMEP} (figures 4.5 to 4.10).

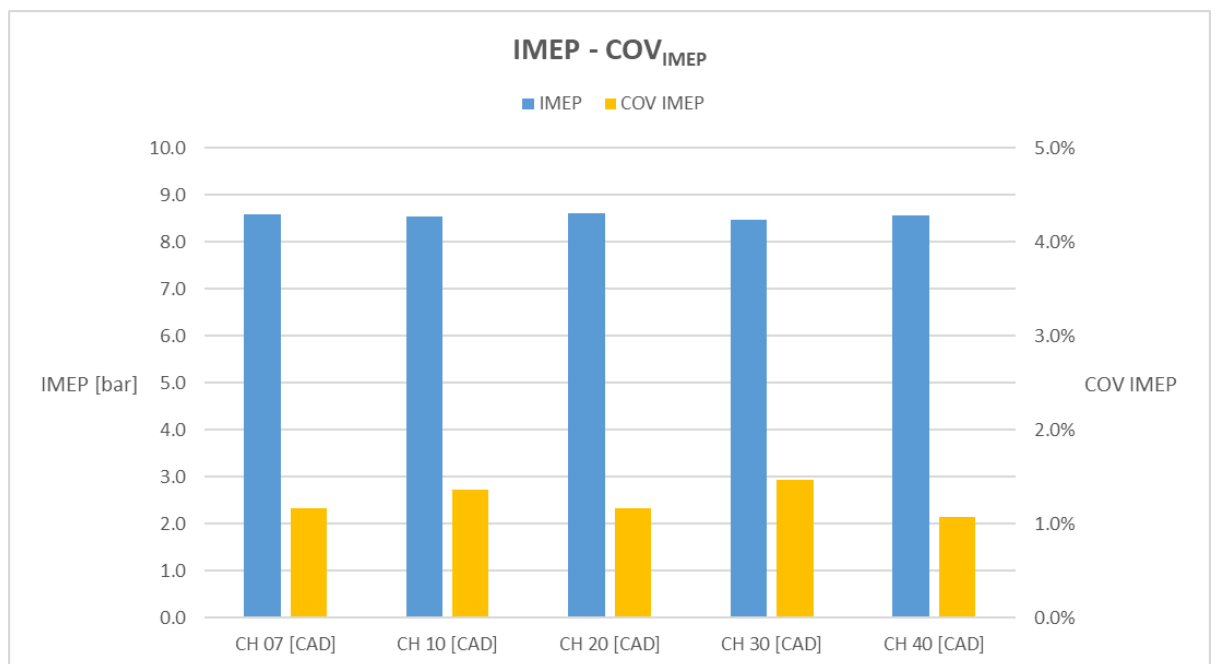
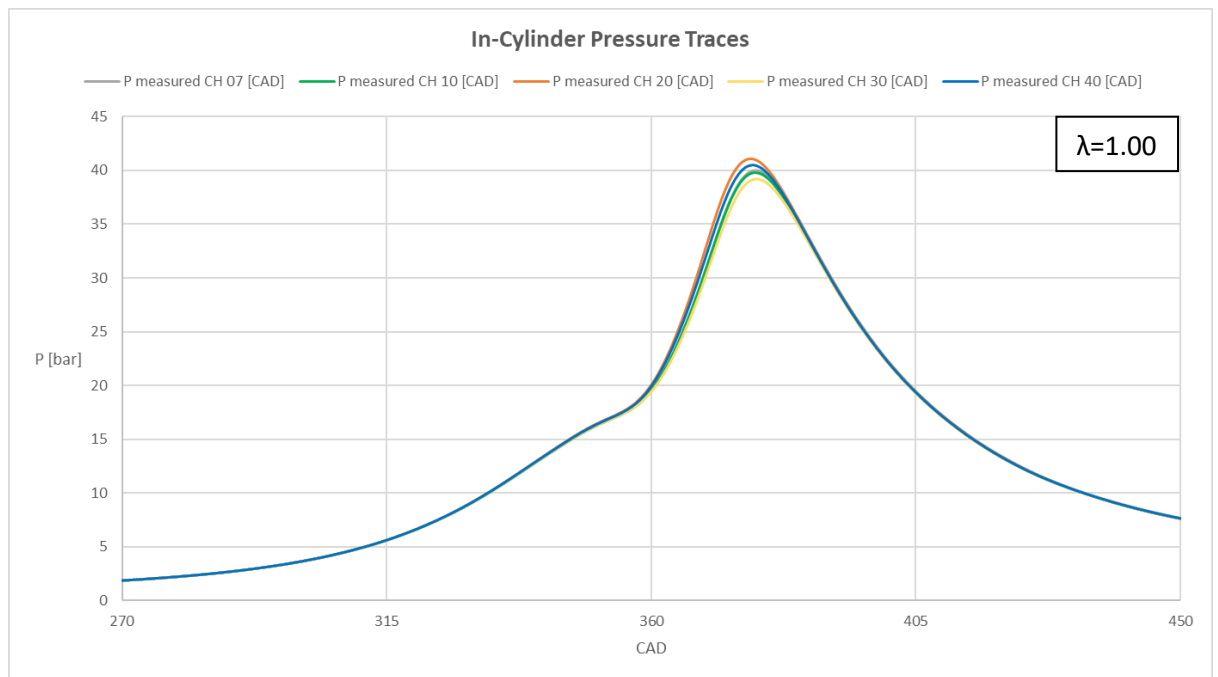


Figure 4. 5, In-Cylinder Pressure Traces, IMEP for COV_{IMEP} for $\lambda=1.00$.

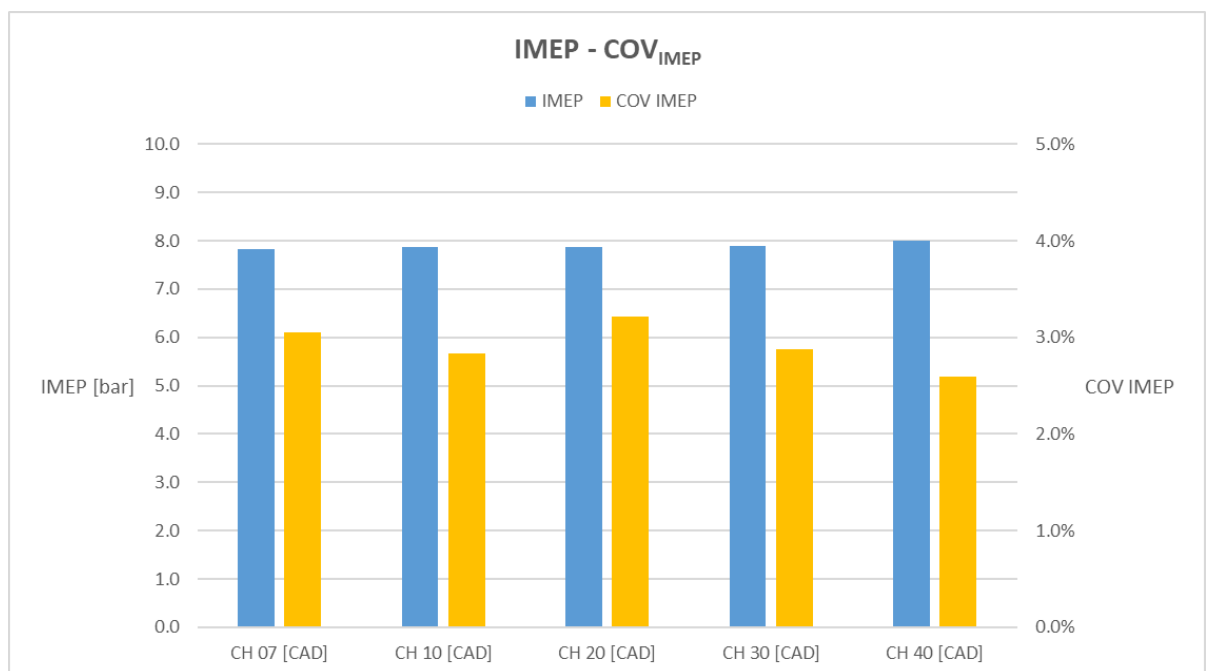
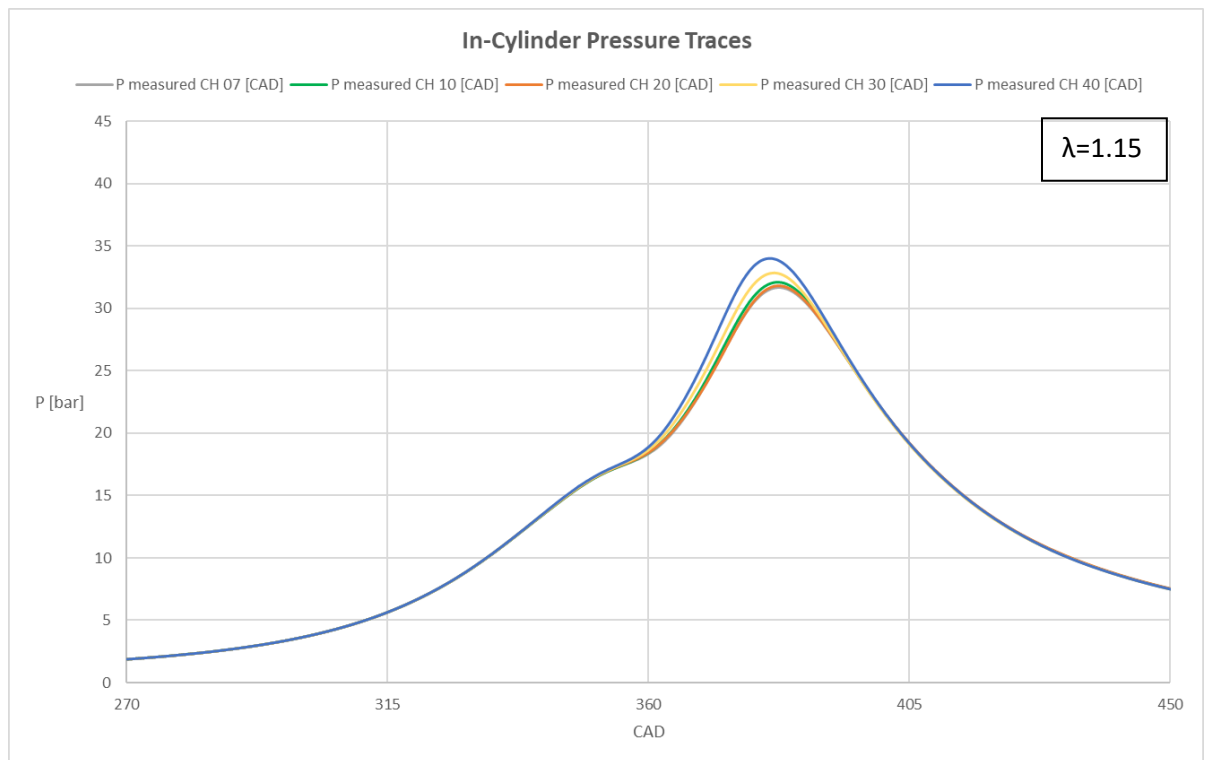


Figure 4. 6, In-Cylinder Pressure Traces, IMEP for COV_{IMEP} for $\lambda=1.15$.

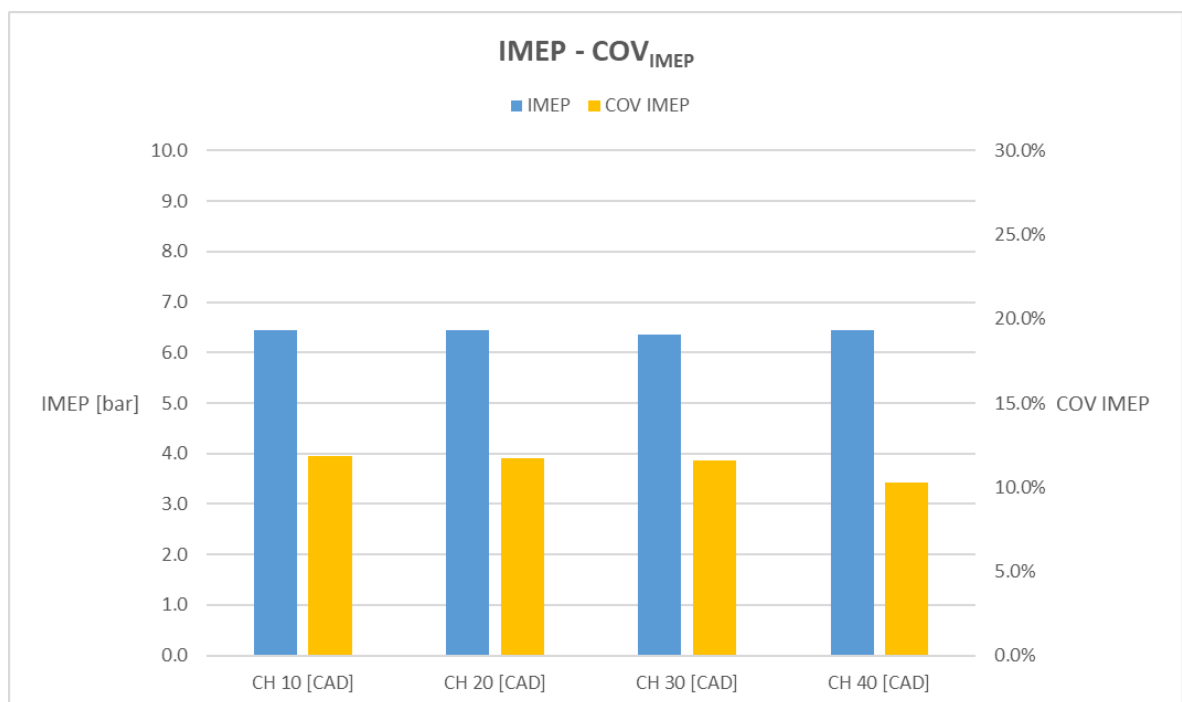
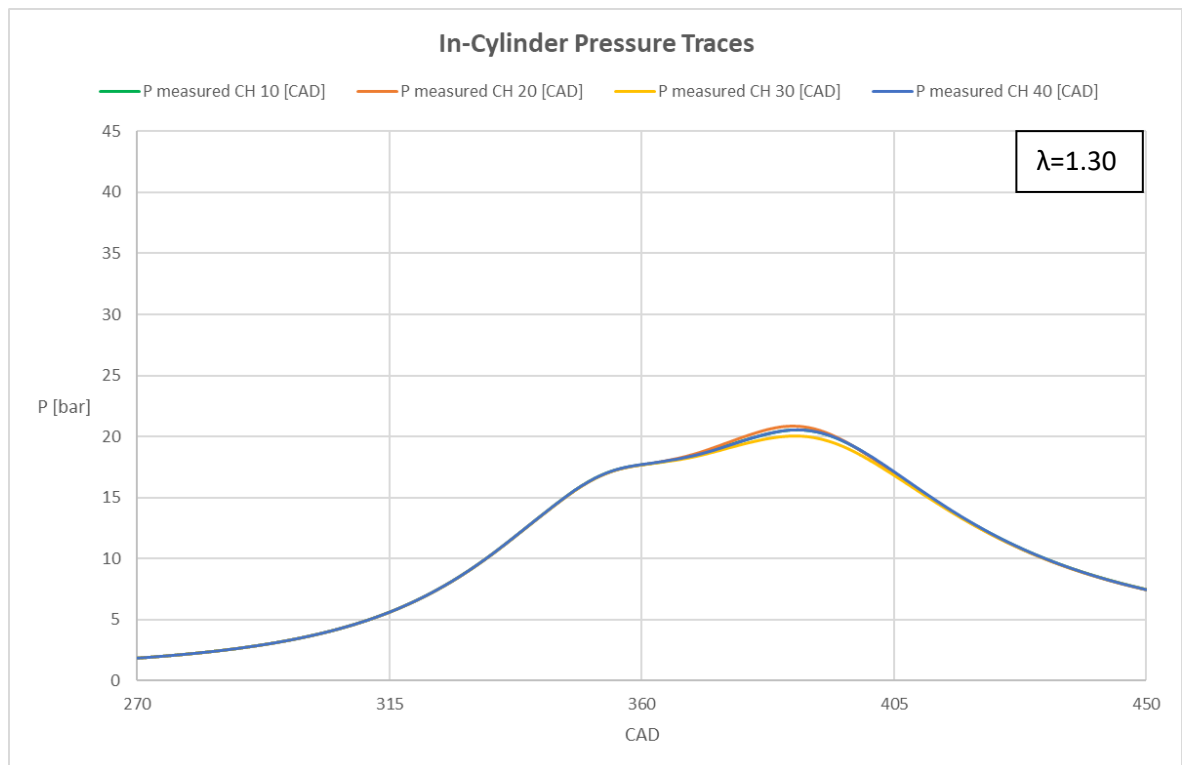


Figure 4. 7, In-Cylinder Pressure Traces, IMEP for COV_{IMEP} for $\lambda=1.30$.

The pressure traces do not show a preferential trend in terms of changes in peak pressure for different values of Coil Charge Duration (Figure 4.5 to 4.7). A similar conclusion can be drawn for the IMEP that practically remains stable for each case examined (Figures 4.6-4.8-4.10). Looking at COV_{IMEP} , as expected with richer AFR there is an evident improvement of stability for the combustion process. The effect of Coil Charge Duration values was more prominent for the mixtures with an air-fuel ratio of $\lambda=1.30-1.15$, for which it is possible to observe an overall decrease of COV_{IMEP} as dwell time was increased. For the stoichiometric blend the COV tends to remain stable. To conclude, based on this initial analysis Coil Charge Duration was fixed at 40 CAD for all conditions that were investigated, so as to ensure good ignition stability and avoid misfiring events.

Chapter 5

Results

5.1 Operative Conditions

Following the initial analysis aimed at identifying eventual coil charge duration effects, more detailed investigations were focused on CCV and the correlation between in-cylinder thermodynamic parameters and flame characteristics. Operative conditions entailed a sweep of air-fuel ratio (AFR), spark advance (SA) and spark plug configuration. Table 5.1 lists these settings for all the cases that were analysed, and it is possible to notice the Coil Charge Duration is not mentioned since as explained in the previous chapter, the effect of the latter on flame kernel formation and front propagation was not appreciable and did not show a well-defined trend in their variation. For these reasons, the Coil Charge Duration was fixed at 40 CAD.

λ	Intake Pressure [bar]	Engine Speed [rpm]	Spark Advance [CAD]	Spark plug Configuration
$\lambda=1.00$	1 (WOT operative condition)	2000	12	Uniflow - Crossflow - Counterflow
$\lambda=1.15$	1 (WOT operative condition)	2000	8	Uniflow - Crossflow - Counterflow
			12	
			16	
			20	
$\lambda=1.30$	1 (WOT operative condition)	2000	24	Uniflow - Crossflow - Counterflow
			12	

Table 5. 1, Engine operative conditions.

Data acquisition followed a procedure that provided some steps to ensure comparable results even if measurements were performed in numerous sessions. The first one concerned the evaluation of intake air temperature (equal to that of the ambient, therefore the tests were carried out in the same period to avoid the problem related to the possibility of having appreciable variations in its value) which was around 300K. The second step involved monitoring the coolant system temperature (controlled using a thermal condition unit) in a range between 50-55K, for the input/output water-flow respectively. The last step was related to the continuous evaluation of piston seals wear to ensure that blow-by leaks were kept in a narrow range. Each series of tests

performed in the laboratory provided the acquisition of cycles in the same motored and fired conditions at the beginning and at the end of each session so as to confirm the validity of recorded data. An even more detailed evaluation was to verify that the in-cylinder pressure at spark timing was as close as possible for all configurations that featured the same advance setting. To do this, once the average pressure signals were obtained with the use of the LabView script, these traces were compared (as shown in Figure 5.1) and any cases that were out of the chosen range were discarded.

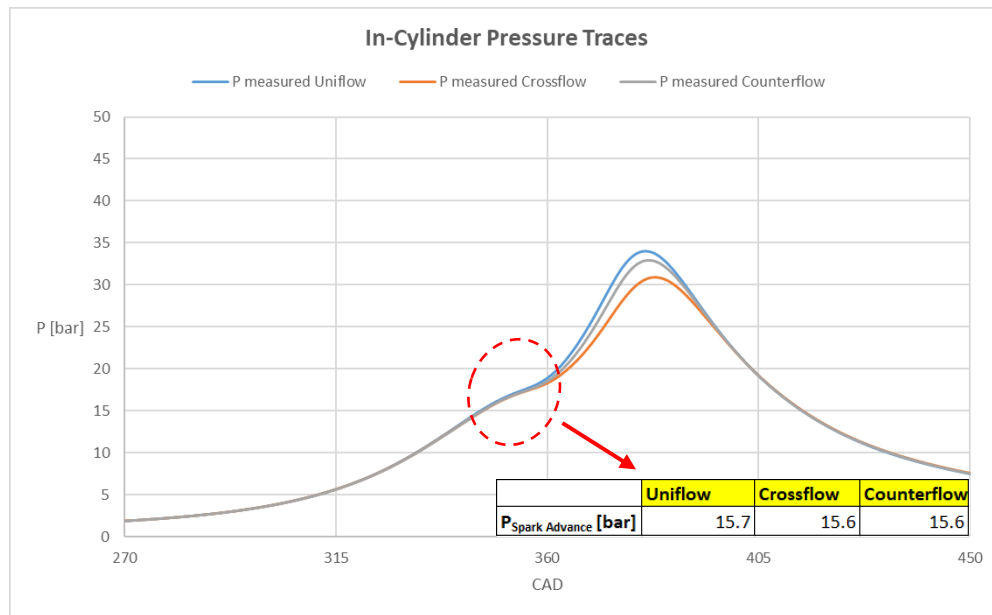


Figure 5. 1, In-Cylinder pressure traces, $\lambda=1.15$, Spark Advance 12 CAD.

For the example shown in Figure 5.1, obtained with lean air-fuel mixture ($\lambda=1.15$) and fixed Spark Advance (SA) of 12 CAD, it is possible to note that the gap at spark timing is less than 0.1 bar, a negligible difference.

5.2 Thermodynamic Results

The following results reported below are divided by spark plug configuration. Therefore, the first series of cases refer to the operative conditions of Spark Advance (SA) fixed at 12 CAD and variable air-fuel ratio (λ). Afterwards, the AFR was fixed for obtaining a lambda value of 1.15 and spark timing could be varied in a wider range (i.e. with stoichiometric fuelling maximum spark advance was limited by knock, while for lambda 1.30 the range of ignition settings was reduced due to stability issues, similar to the effects observed in [38]). In this way, each effect could be quantified in conditions that entail a certain cause, while other influences were reduced as much as possible.

5.2.1 Thermodynamic Results for Fixed Spark Advance (SA)

The main idea behind fixing the ignition setting was to ensure that flame kernel initiation occurs in similar conditions with respect to tumble and turbulence intensity. This emphasizes the effects of the chemical composition, thus the reactivity of the mixture and time characteristics as well as the influence of spark plug orientation with respect to the interaction with fluid motion.

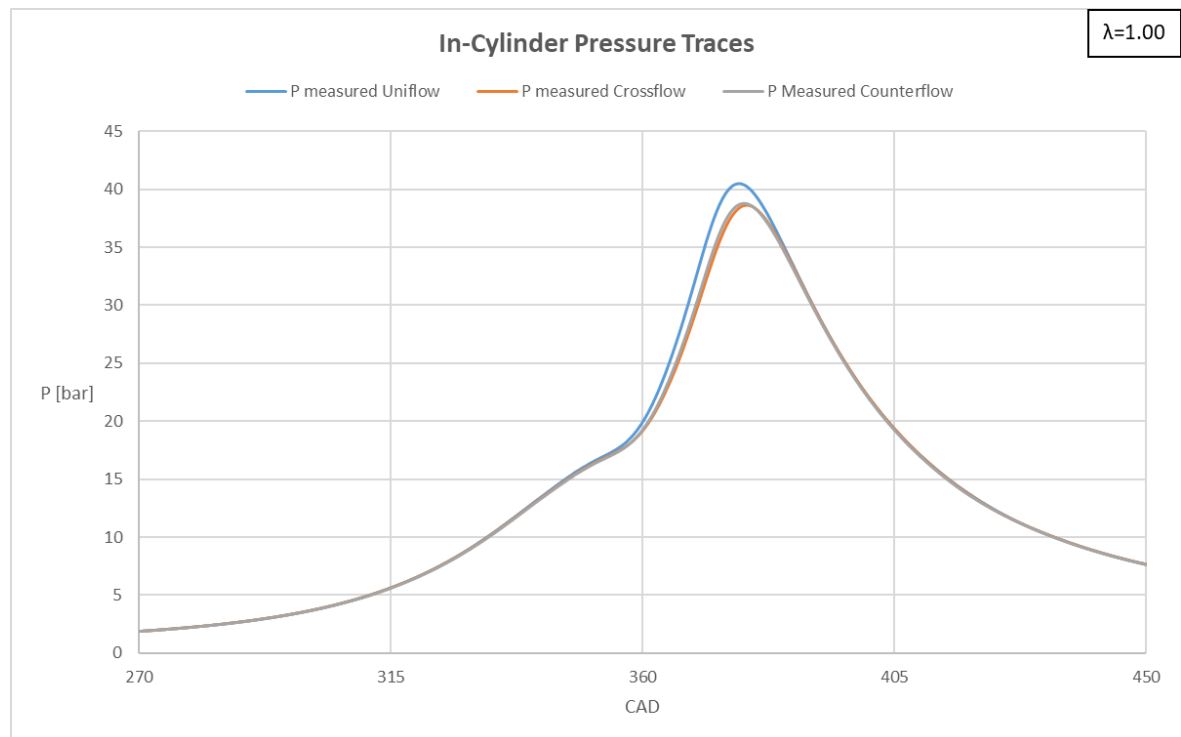


Figure 5. 2, In-cylinder Pressure traces for $\lambda=1.00$.

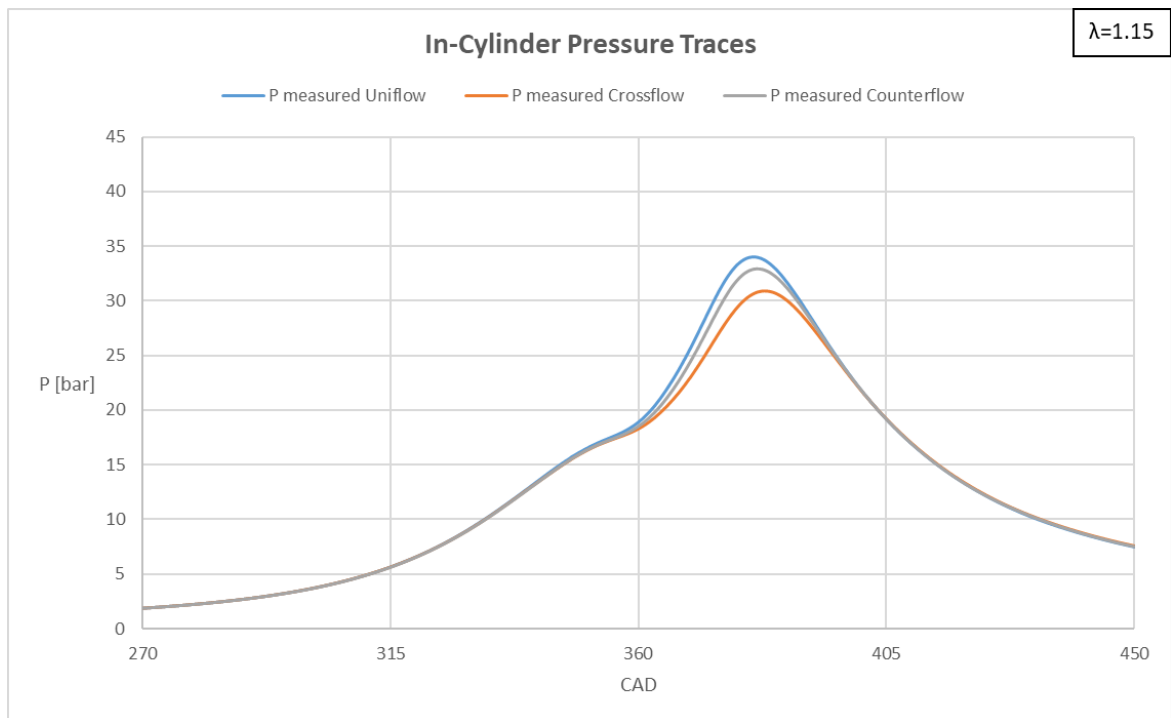


Figure 5. 3, In-cylinder Pressure traces for $\lambda=1.15$.

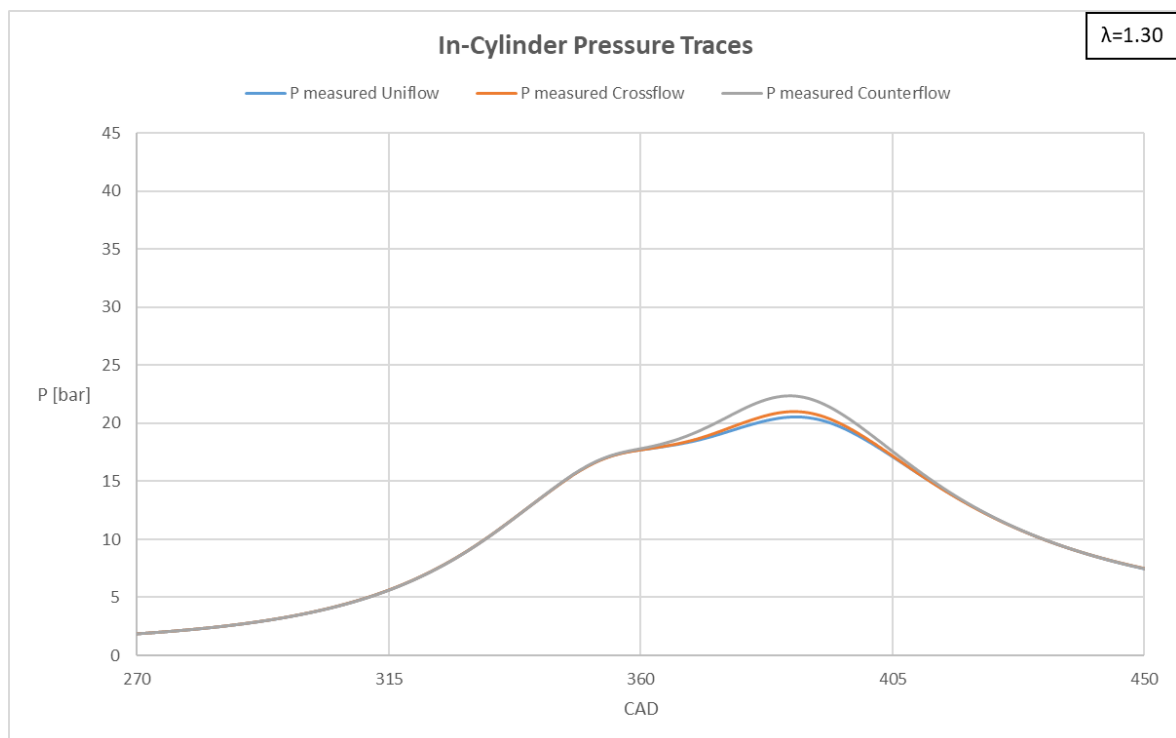


Figure 5. 4, In-cylinder Pressure traces for $\lambda=1.30$.

Looking at the graphs showing the average in-cylinder pressure (Figure 5.2 - 5.3 - 5.4), no well-defined trend was observed. Peak pressure values appear to be influenced in a contained way by the Uniflow and Counterflow configurations; overall the Crossflow configuration seemed to

feature lower peak pressure compared to the other two orientations. As expected, with richer air-fuel mixtures, there is an increase in terms of IMEP values (figure 5.5) as a direct consequence of larger injected fuel quantity and higher-pressure peak reached during the combustion phase. Furthermore, it is interesting to observe the gap between the three traces during the first stage of the combustion process, an indication that there was high cycle to cycle variability. For better understanding of CCV effects, COV_{IMEP} gives an overview of engine output, while $COV_{P_{MAX}}$ is more closely related to the actual variability of combustion. The latter are shown in figures 5.5 and 5.6.

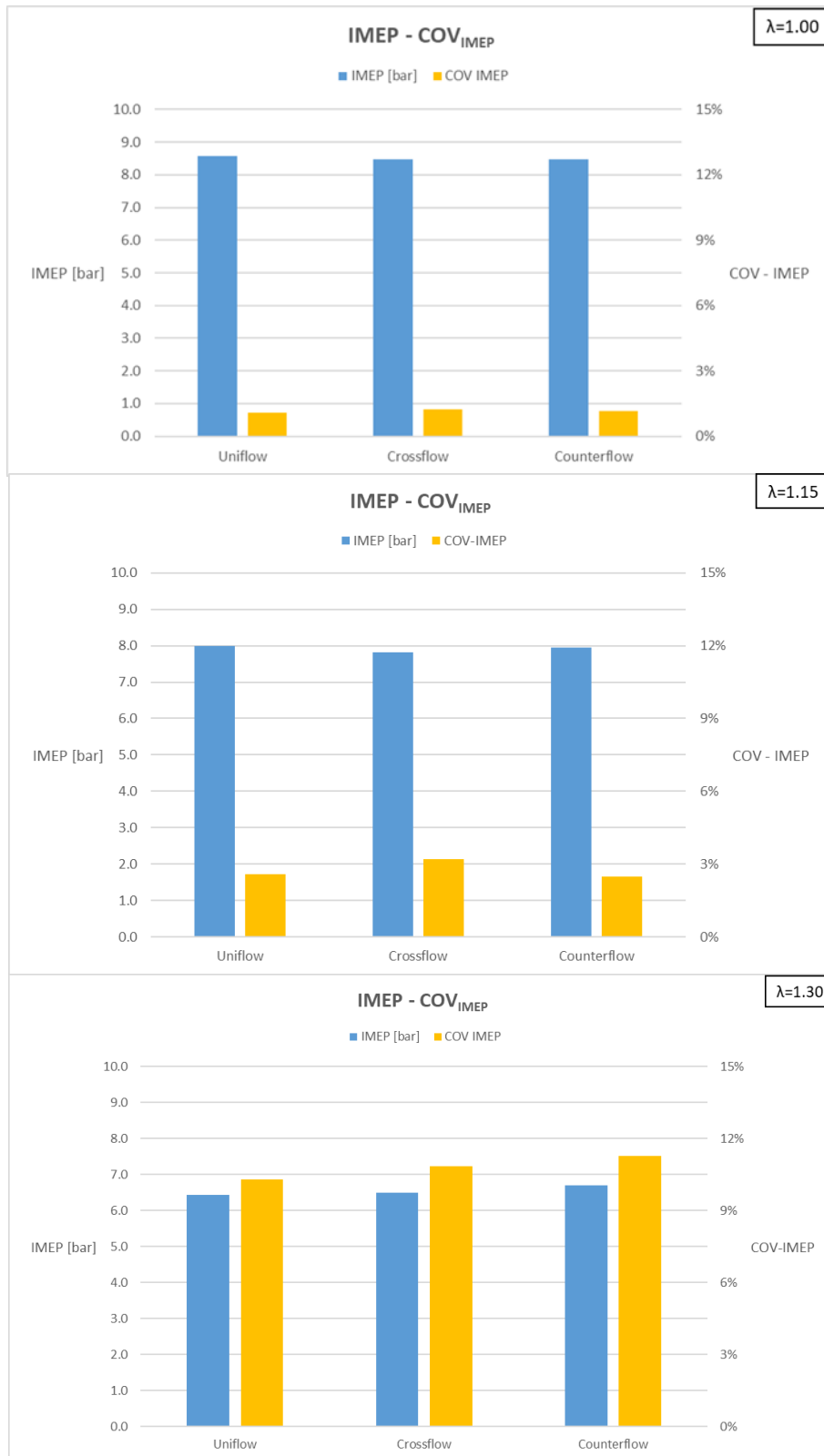


Figure 5. 5, IMEP and COV_{IMEP} for $\lambda=1.00-1.15-1.30$.

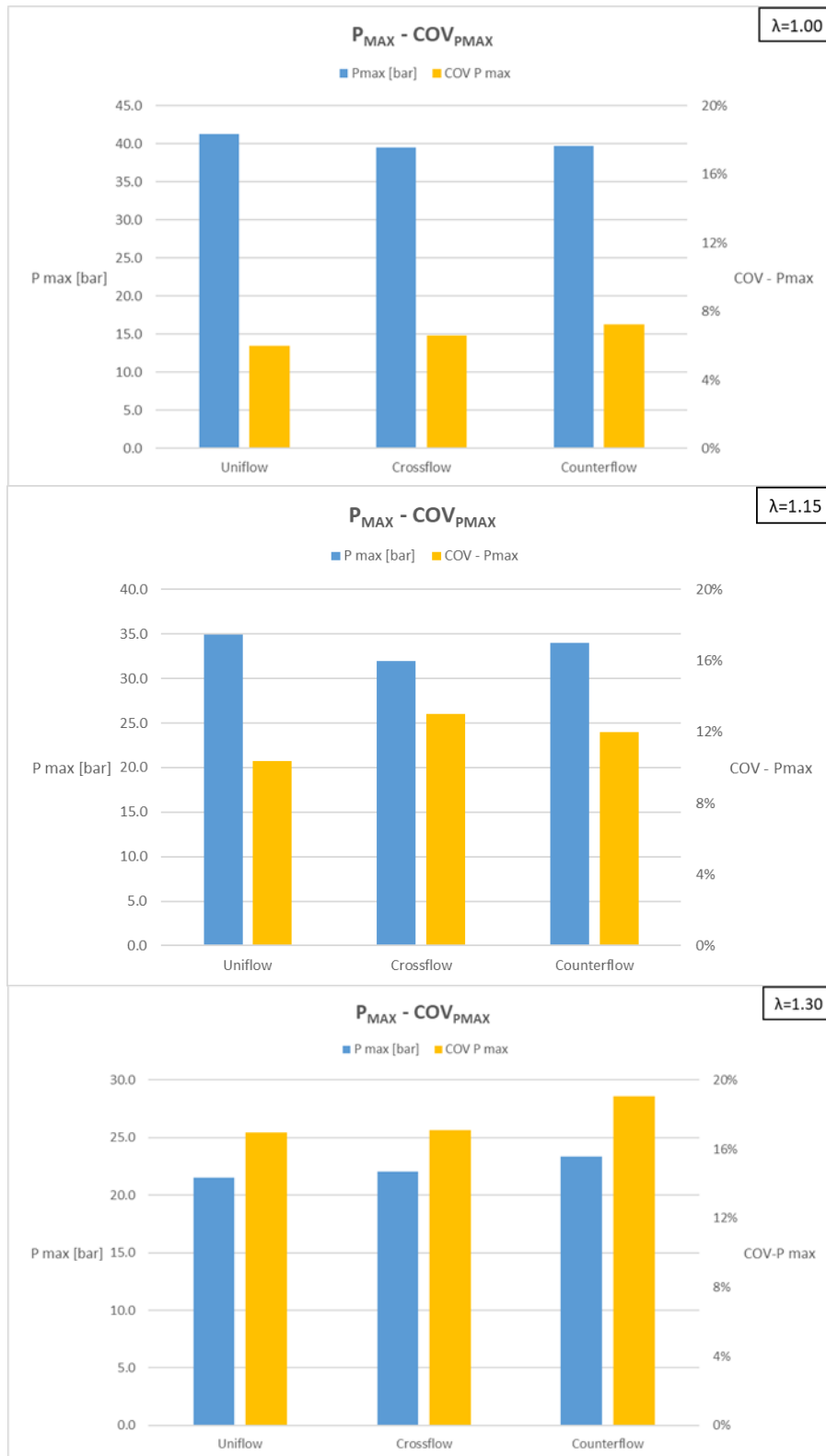


Figure 5. 6, P_{\max} and $COV_{P_{\max}}$ for $\lambda=1.00-1.15-1.30$.

As a direct influence of “slower” combustion (therefore considering the cases with lean mixtures, longer chemical time scales are characteristic) increased effects of turbulence-flame interactions and larger COV are expected. Looking at the reported COV_{IMEP} values (Figure 5.5), it can be seen that for the operative condition with the leanest mixture the Counterflow configuration shows the highest cyclic variability (around 11.8%) if compared with the other two (respectively 9.8% for Uniflow and 10.2% for Crossflow). For the air-fuel ratio $\lambda=1.15$ and $\lambda=1.00$, a different situation was evident, in fact for the latter there is an alternation between the Crossflow and Counterflow configuration in terms of higher values of COV_{IMEP} . The Uniflow configuration appears more “stable” for each case, (probably related to the fact that the electrode “J” acts as “shield” for the tumble motion, therefore the kernel formation results more stable and consequently the flame front propagation as well). In line with what was previously observed for the overall shape of in-cylinder pressure traces, with richer mixtures the overall IMEP value tends to increase while the trend for the COV_{IMEP} and $COV_{P_{MAX}}$ is obviously opposite (i.e., reduced stability was recorded for lean operation). The cyclic variability for the leanest AFR is very high (an overall value around 10%), therefore the combustion process is unstable and events such as misfiring or partial burning can occur. It should be noted that only the latter phenomenon was present for the sets of data recorded for this study. With the increase of the Duration of Injection, from 30 to 39 CAD (therefore the operative conditions corresponding from $\lambda=1.30$ up to the stoichiometric one) there is an evident reduction of COV_{IMEP} (Figure 5.5), a sign that the cyclic variability was much more contained (lower than 3.5% for $\lambda=1.15$ and around 1% for $\lambda=1.00$). Peak pressure variability, i.e., $COV_{P_{MAX}}$ (Figure 5.6) featured relatively higher values, mostly due to the fact that the IMEP parameter is integrated over 720 CAD, thus reducing the actual influence of combustion stability itself. Other phenomena related to the optical engine characteristics (listed in the Chapter 2 in the dedicated paragraph) can also contribute to variations in terms of cyclic repeatability (e.g. the large top-land region volume can significantly influence the final part of the combustion process). Looking at the absolute values, for the leanest blend this value stands at more than 15% (with a peak of almost 19% for the counterflow configuration) and decreases to around 12% for $\lambda=1.15$ and finally to 6% for the stoichiometric operative condition. An overall trend of highest $COV_{P_{MAX}}$ for the counterflow configuration can be observed (the only exception is for $\lambda=1.15$).

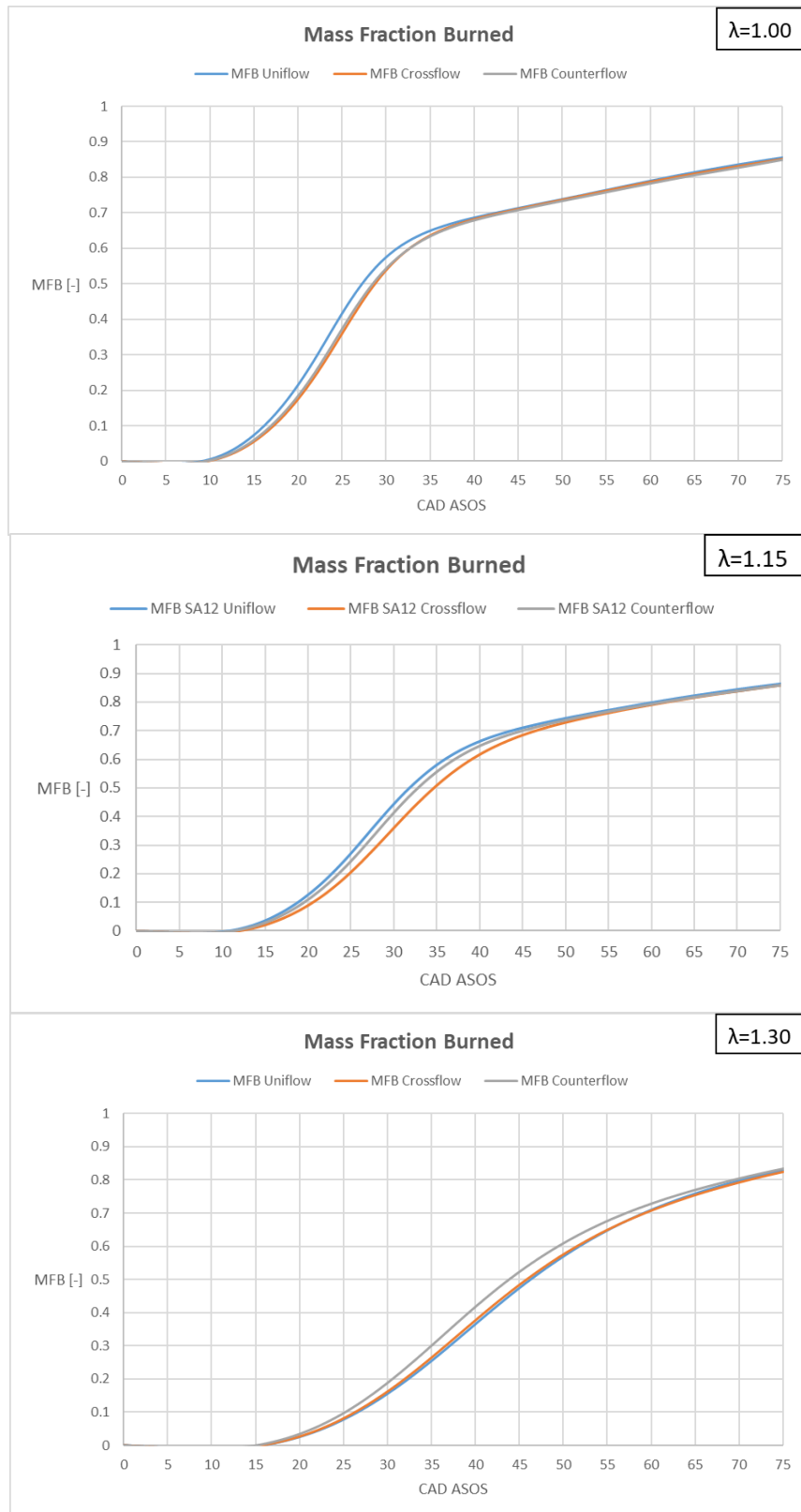


Figure 5. 7, Mass Fraction Burned for $\lambda=1.00-1.15-1.30$.

The in-cylinder MFB traces show an increasing burning rate as the duration of injection was increased (figure 5.7). In line with what was previously said, it is possible to observe an alternation between the Counter and Uniflow configurations in terms of higher flame front propagation speed. In terms of burned mass, the location of 50% (MFB50) is reached in comparable times by each configuration (respectively around 45 CAD ASOS for $\lambda=1.30$, 31 CAD ASOS for $\lambda=1.15$ and 28 CAD ASOS for the stoichiometric operative condition). For the Spark Advance set at 12 CAD, the MBT operative condition is close to being reached for $\lambda=1.15$ -1.00 (for this engine the MBT was found to feature an MFB50 location around 18 CAD ATDC). Moreover, the maximum gap between the three traces was registered when passing from the Uniflow configuration to Crossflow for $\lambda=1.15$; in fact, in the latter condition a gap of 3 CAD was observed. Finally, as expected, with a leaner charge, the duration of the early stage of flame front development (0-10% MFB) is extended (25 CAD for $\lambda=1.30$, 19 CAD $\lambda=1.15$ and 17 CAD for the stoichiometric condition), mainly due to the lower reactivity of the mixture.



Figure 5. 8, COV-Is for $\lambda=1.00-1.15-1.30$.

Observing the figures related to the COV of secondary current intensity signals (Figure 5.8) for the three configurations, it is possible to note that the Crossflow configuration has the highest variability for all the air-fuel ratio levels examined. The cause is related to the position of spark plug that in this configuration exposes the “space” between the two electrodes to the tumble motion more than the others two configurations, therefore the secondary current intensity signals that is directly correlated to the electric arc results more instable.

5.2.2 Thermodynamic Results for Fixed Lambda (λ)

The following part of the analysis features the operative condition for fixed DOI/ λ and variable Spark Advance (SA). As previously explained, the intermediate level of AFR ensured the widest range for sweeping the ignition timing, without the risk of knocking and acceptable level of stability. The following results are related to the operative condition for a fixed Duration of Injection (DOI) of 34 CAD corresponding to $\lambda=1.15$ and variable Spark Advance (SA) from 8 to 24 CAD with a step of 4 CAD between each case.

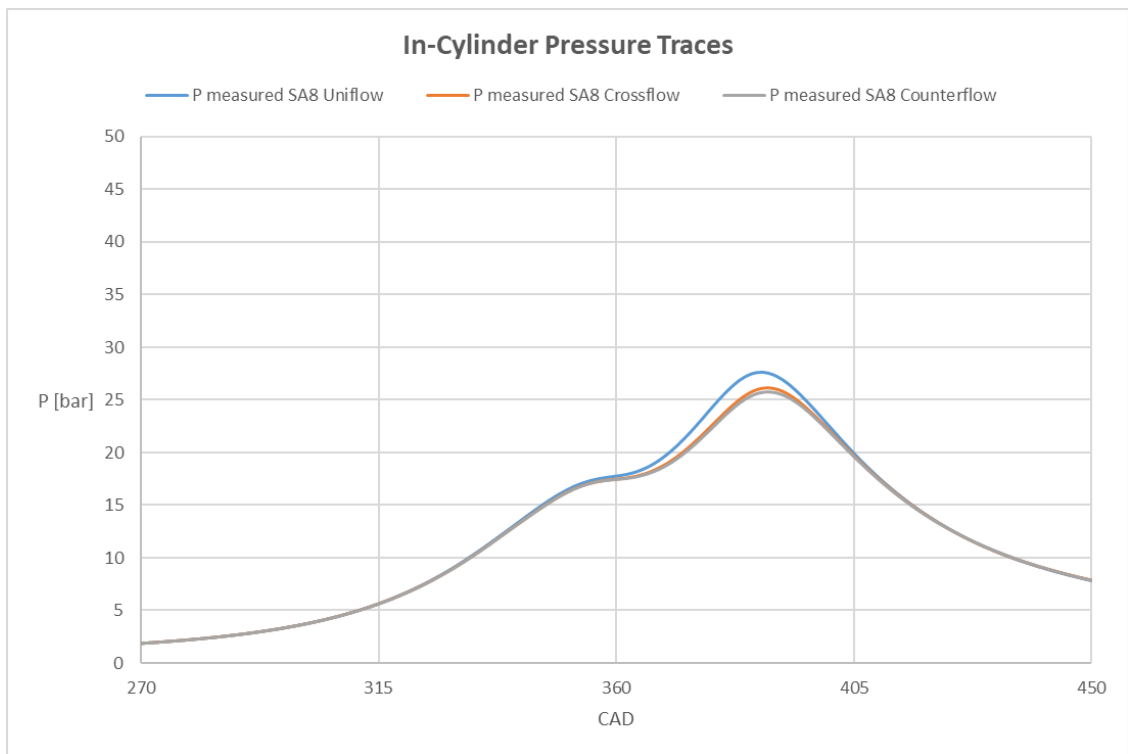


Figure 5. 9, In-cylinder Pressure traces for $\lambda=1.15$ and SA 8 CAD.

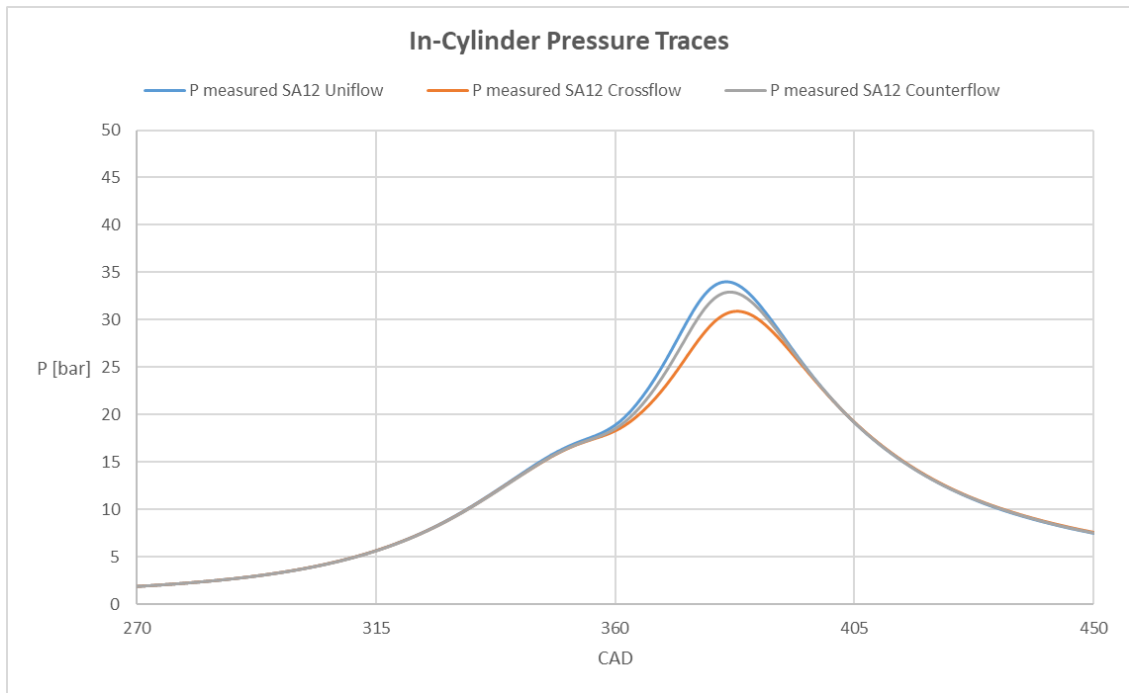


Figure 5. 10, In-cylinder Pressure traces for $\lambda=1.15$ and SA 12 CAD.

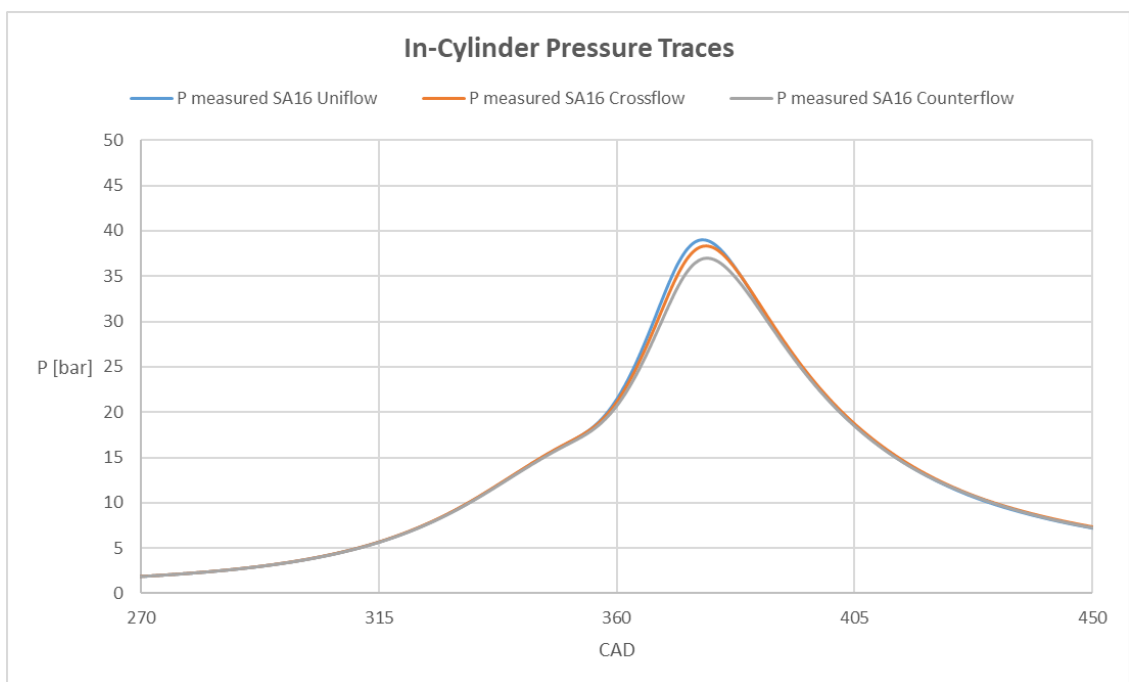


Figure 5. 11, In-cylinder Pressure traces for $\lambda=1.15$ and SA 16 CAD.

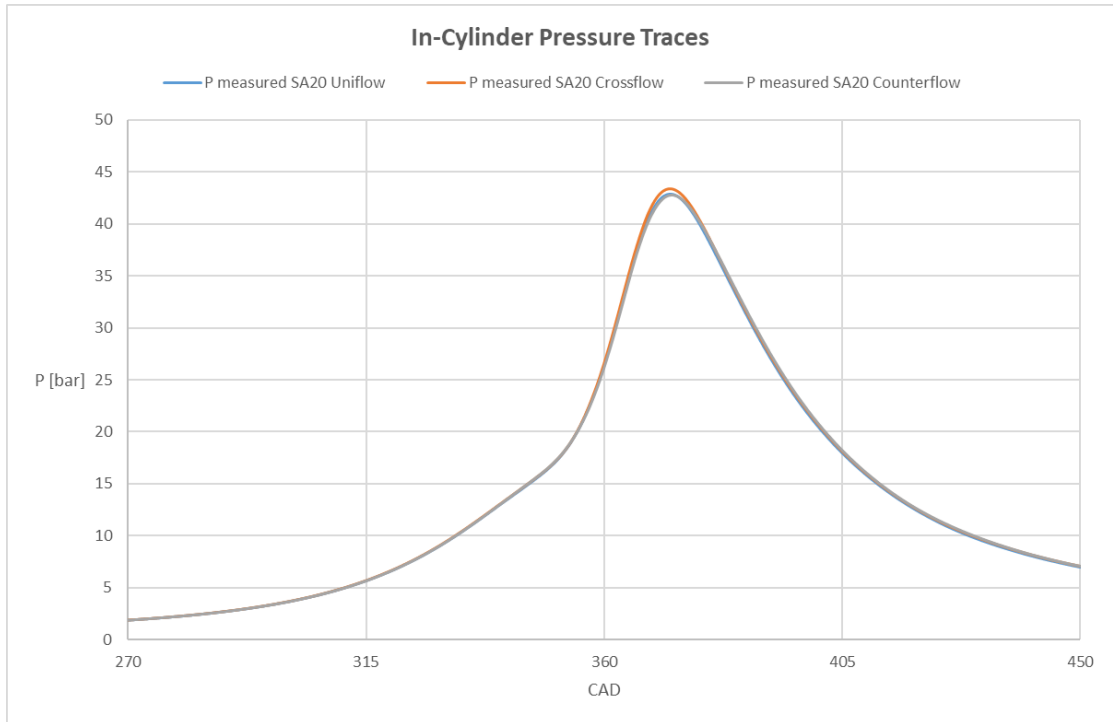


Figure 5.12, In-cylinder Pressure traces for $\lambda=1.15$ and SA 20 CAD.

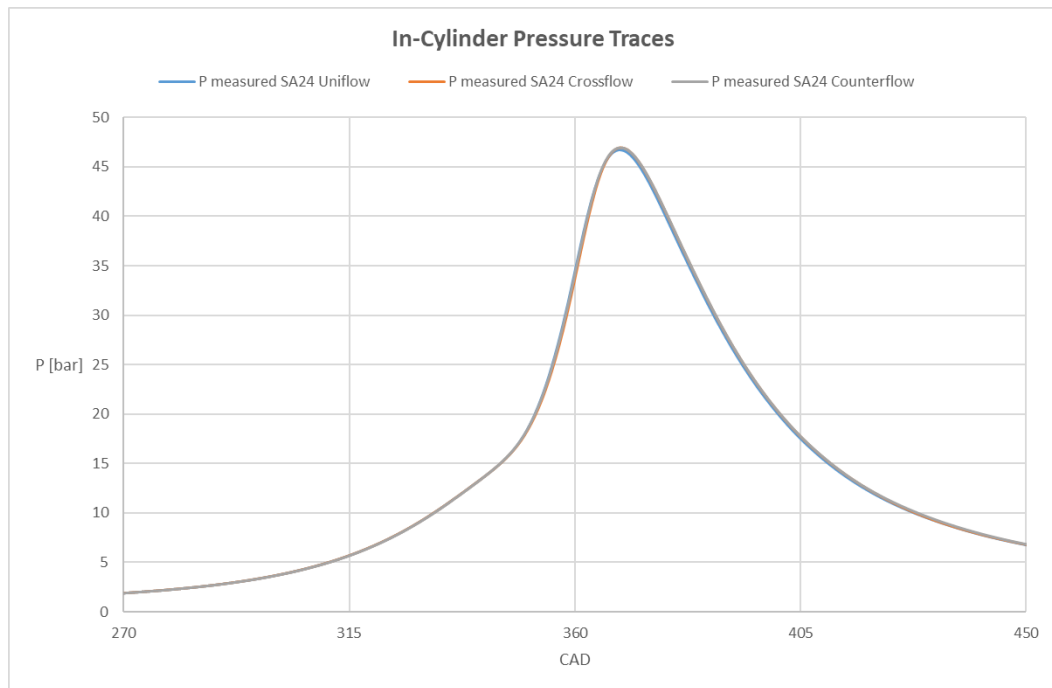


Figure 5.13, In-cylinder pressure traces for $\lambda=1.15$ and SA 24 CAD.

As ignition was advanced, peak pressure reached higher values (Figure 5.9 to 5.13). In fact, anticipating the spark timing angle, combustion will start earlier during the compression stroke, therefore the compression related to the flame front propagation added to that due to the piston motion will result in increased in-cylinder peak pressure. On the other hand, anticipating the

ignition event results in higher compression work, thus increasing counter torque to the crankshaft (without mentioning problems related to the onset of knocking phenomenon, especially for stoichiometric fuelling). It may therefore be useful to refer to a parameter that allows to have an idea on the quality of the combustion process. This parameter corresponds to Maximum Brake Torque operative condition (MBT). In a common automotive engine, it corresponds to the 50% of MFB reached around 8-10 CAD ATDC. For this particular optically accessible engine this value was found to be around 15-18 CAD ATDC, mainly due to the high blow-by losses through the piston seals. Furthermore, looking at the in-cylinder pressure trace, it is interesting to observe how the three signals, one for each different spark plug configuration, feature a visible gap between each other for the operative conditions related to delayed spark ignition timing. This gap tends to reduce with the increase of Spark Advance since the combustion process begins in a part of the cycle with more stable organized flow (i.e. tumble) and consequently has better repeatability. Finally, in terms of pressure peak, the Uniflow configuration shows the highest values for each case examined (the only exception is for SA20 CAD).

In line with previous claims about the in-cylinder pressure, the increase of the Spark Advance corresponds to higher IMEP values up to an optimum point that was found to be around 16 CAD (Figure 5.14). In accordance with the definition of Maximum Brake Torque operative condition (corresponding to the higher value of IMEP and acceptable level of COV_{IMEP}), it is reached at SA 16 CAD for the Uniflow and Crossflow configuration, while for Counterflow at SA 20 CAD. The COV_{IMEP} values for the three configurations are comparable, but for delayed Spark Advance the Counterflow and Crossflow configurations seem to have higher cyclic variability (respectively 4.2% and 3.8% against 3.3% of Uniflow); anticipating the spark ignition event reverses the trend, with the Uniflow COV_{IMEP} that decreases slower than other two (2.1% versus 2% for crossflow and 1.7% for Counterflow). Finally, for the most anticipated spark ignition condition the three configuration tends to stabilize on equal values (around 2%).

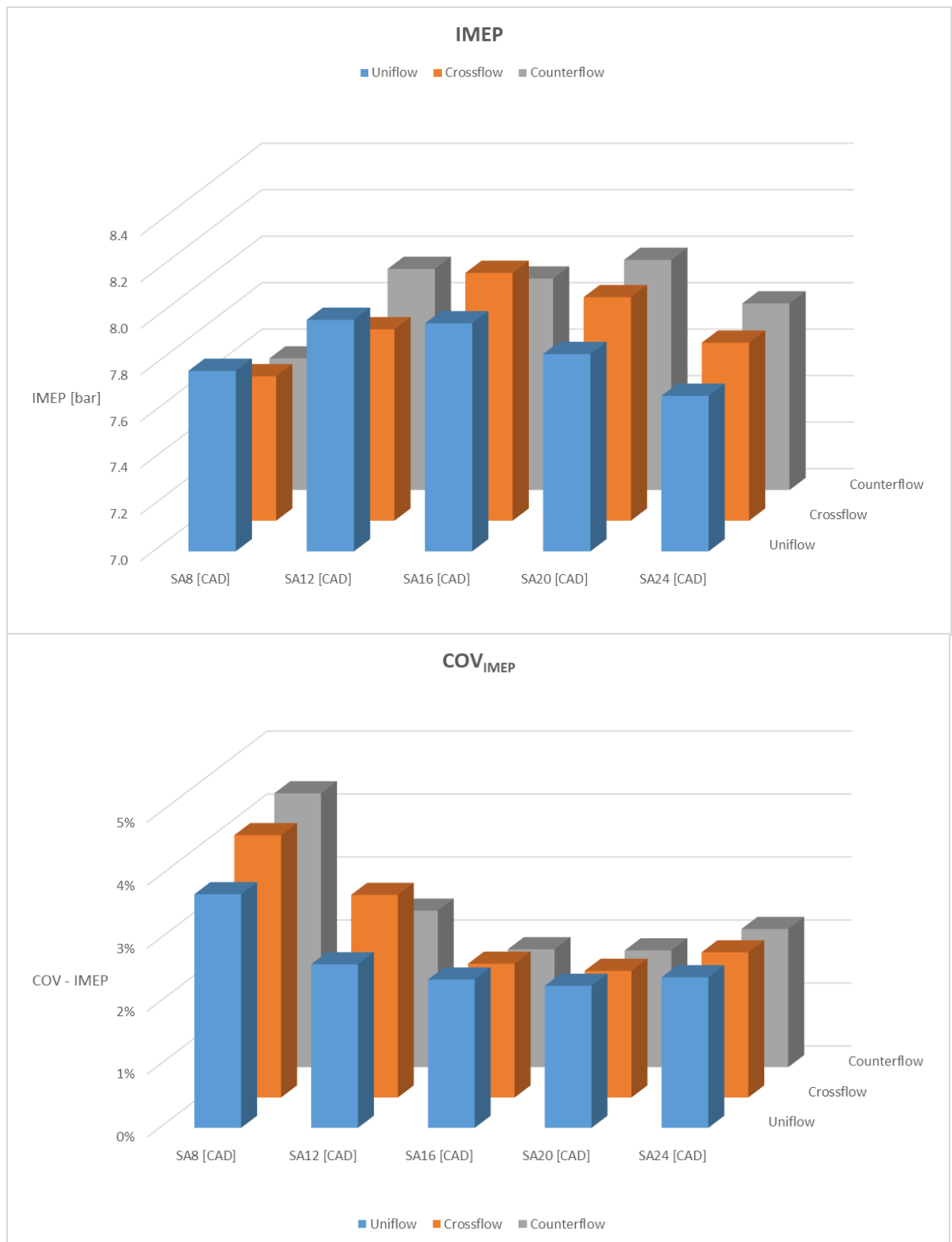


Figure 5. 14, IMEP and COV_{IMEP} values for the Spark Advance sweep, $\lambda=1.15$.

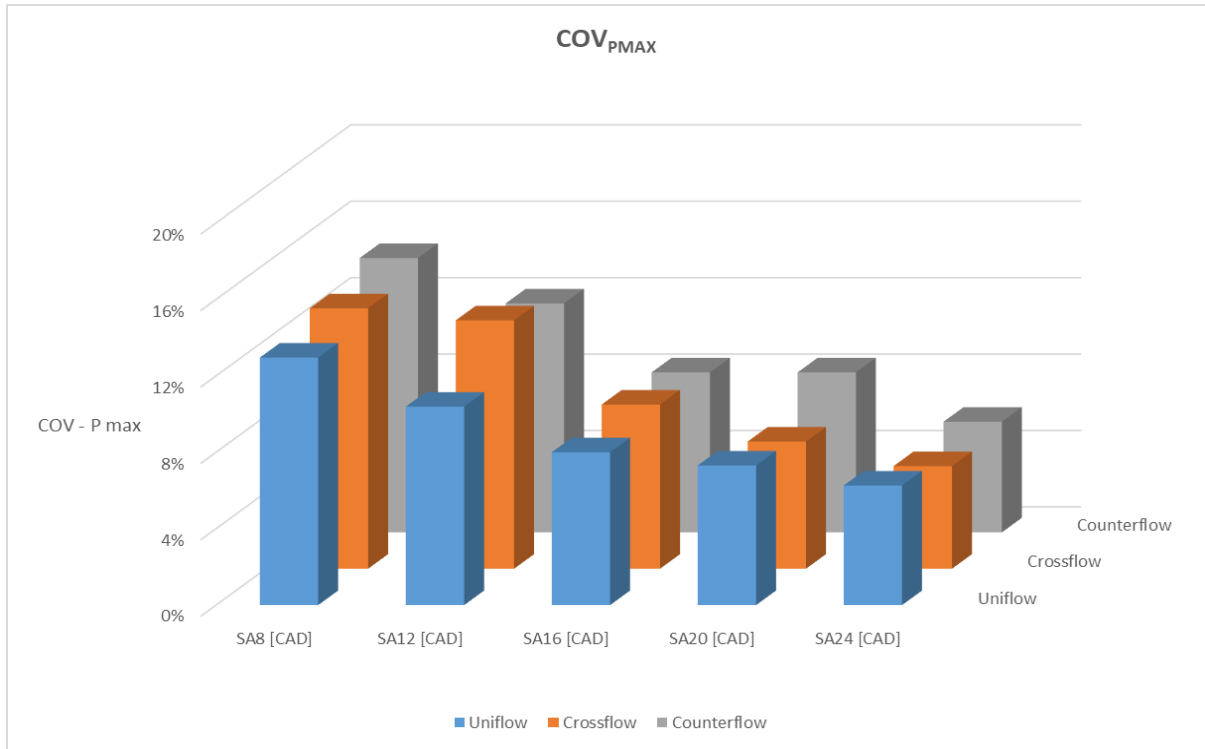


Figure 5. 15, $COV_{P MAX}$ values for the spark timing sweep, $\lambda=1.15$.

Unlike the COV_{IMEP} , the $COV_{P MAX}$ shows an overall continuously decreasing trend with the increase of Spark Advance, for the investigated range. In line with the results of in-cylinder pressure, a reduced $COV_{P MAX}$ corresponds to a good cyclic repeatability and in fact looking at the pressure traces for SA 24 CAD (Figure 5.13) the gap between the signals is very contained when switching from one plug orientation to another.

Figure 5.16 shows calculated MFB traces of the three plug configurations for each spark timing. Negative MFB values are due to the simplified approach that was employed. A more complex analysis that includes heat transfer and blow-by modelling would have resulted in more plausible results, but this procedure was preferred. In fact, calculating the VFB from the MFB the intent was of correlating the thermodynamic (i.e. the cycle most representative for an average in-cylinder evolution) and optical data; the latter category provides much more valuable information on the spatial distribution of the reacting and burned gas, as well as insight into the interaction with the working fluid. As expected, the evolution results “slower” for the most delayed Spark Advance (SA).

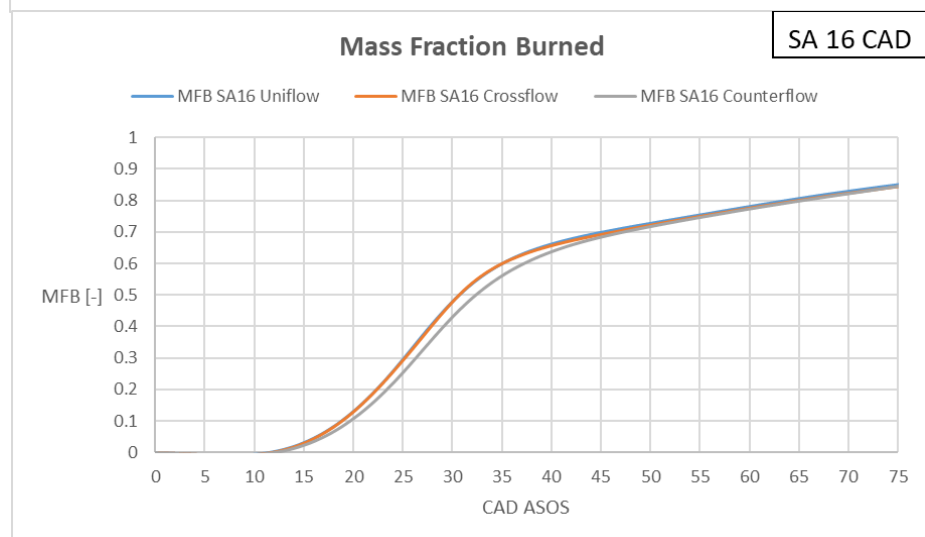
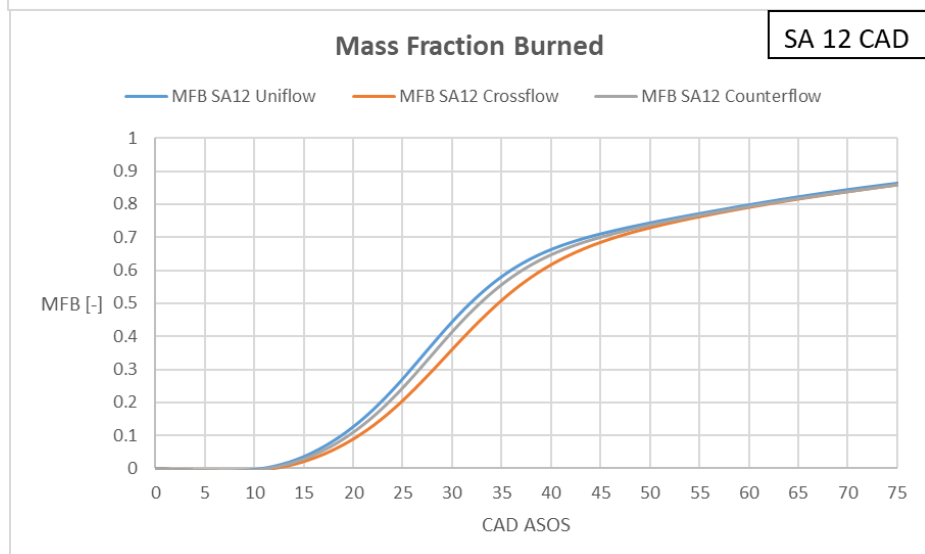
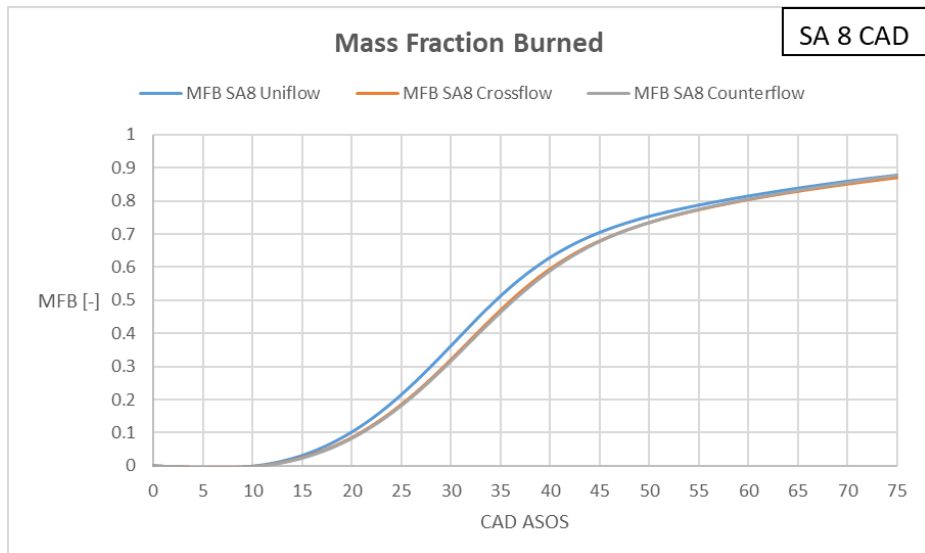




Figure 5. 16, Mass Fraction Burned for $\lambda=1.15$ and Spark Advance from 8 to 24 CAD.

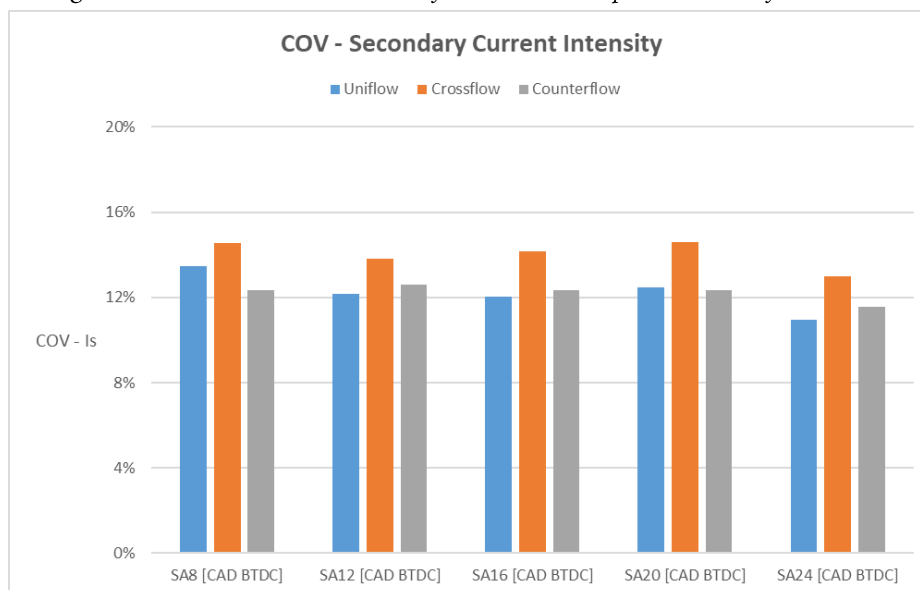


Figure 5. 17, COV – Secondary Current Intensity, $\lambda=1.15$.

Observing the secondary current intensity signals (Figure 5.17), the Crossflow configuration shows the highest variability for the Secondary Current Intensity signal (mainly due to the fact that with this orientation of the spark plug, the space between the two electrodes is more exposed to the tumble motion compared to the other two configurations), while an overall decreasing trend can be seen with the increase of Spark Advance.

5.3 Optical Results

To gain further insight into the evolution of combustion related phenomena, a detailed analysis of cycle resolved visualization images was performed, through the post-processing procedure previously described. A detailed morphology characterization of the flame kernel and flame front were performed. In this results section, after the global thermodynamic analysis of the combustion process, the sequence of images acquired with the high-speed camera were post-processed and analysed to have a better understanding of the spatial behaviour of the combustion process. As previously said, the optical analysis is strongly dependant on user sensitivity in setting the required parameters for running the NI Vision script. Therefore, a further validation measure to ensure that the greyscale parameter (that directly influences the flame detection sensitivity of the software) was correct and not overestimated or underestimated, the Volume Fraction Burned traces obtained from the Thermodynamic analysis of 200 consecutive cycles was compared with the VFB of the cycle (one of ten recorded by the high-speed camera) that was closest to the average trace. Then, from this sequence it is possible to obtain the evolution of the normalized flame area and compare it with the VFB derived from thermodynamic evaluations. This simplified

method allows a rapid check of the correct settings for greyscale value, given that the evolution of the flame area is directly related to the sensitivity of the NI Vision script; an example is shown in figure 5.18.

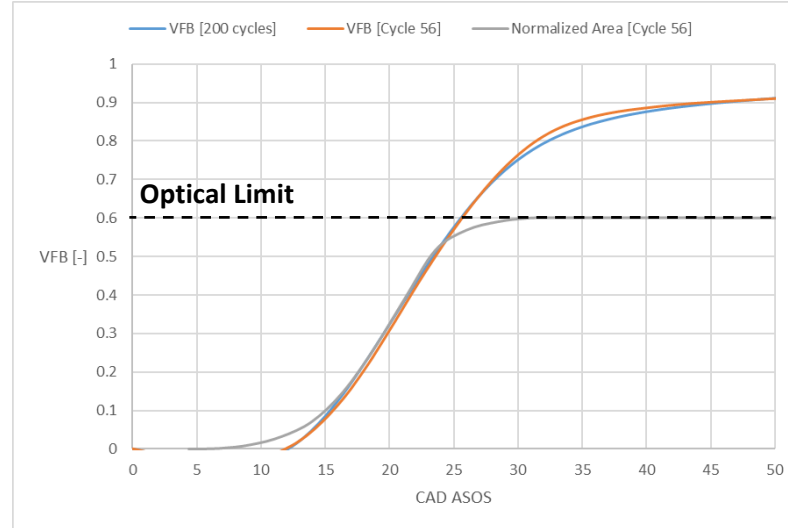


Figure 5. 18, Volume Fraction Burned comparison with normalized area, $\lambda=1.15$, SA16 CAD, Counterflow configuration.

The optical results, like the thermodynamic ones, are divided by parameters settings (table 5.1) and the first series of data reported below refers to the operative conditions for fixed spark advance (SA) set at 12 CAD and variable air-fuel ratio (AFR).

5.3.1 Optical Results for Fixed Spark Advance (SA)

When making considerations related to the observed trends, results corresponding to the acquisitions made at 14 and 16.4 CAD ASOS (1.2 ms and 1.4 ms from spark ignition) were taken as input data. This was decided so as to be sure to have a good quality of the frames that were acquired (i.e., high enough intensity with respect to the early flames that were biased by the presence of the spark arc, and small enough to be completely contained by the field of view) and to reduce the cases without any object visualized.

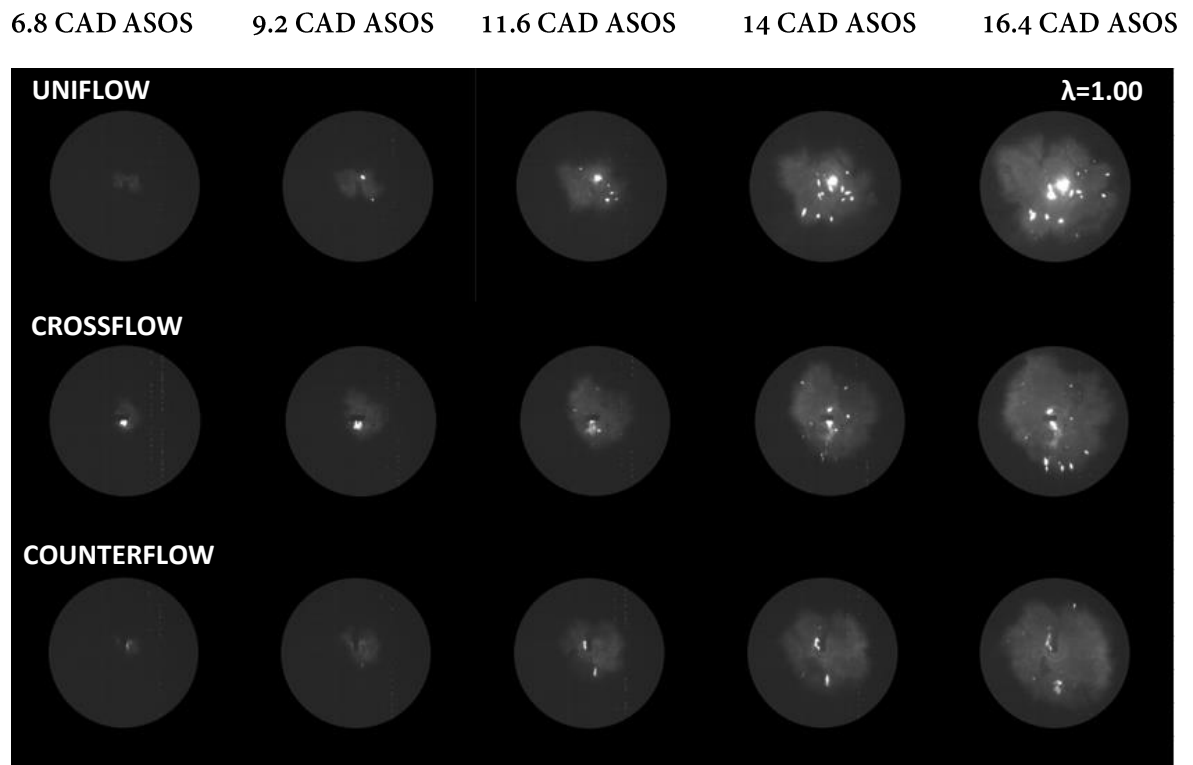


Figure 5. 19, Flame image sequence during the flame propagation stage, $\lambda=1.00$, SA12 CAD.

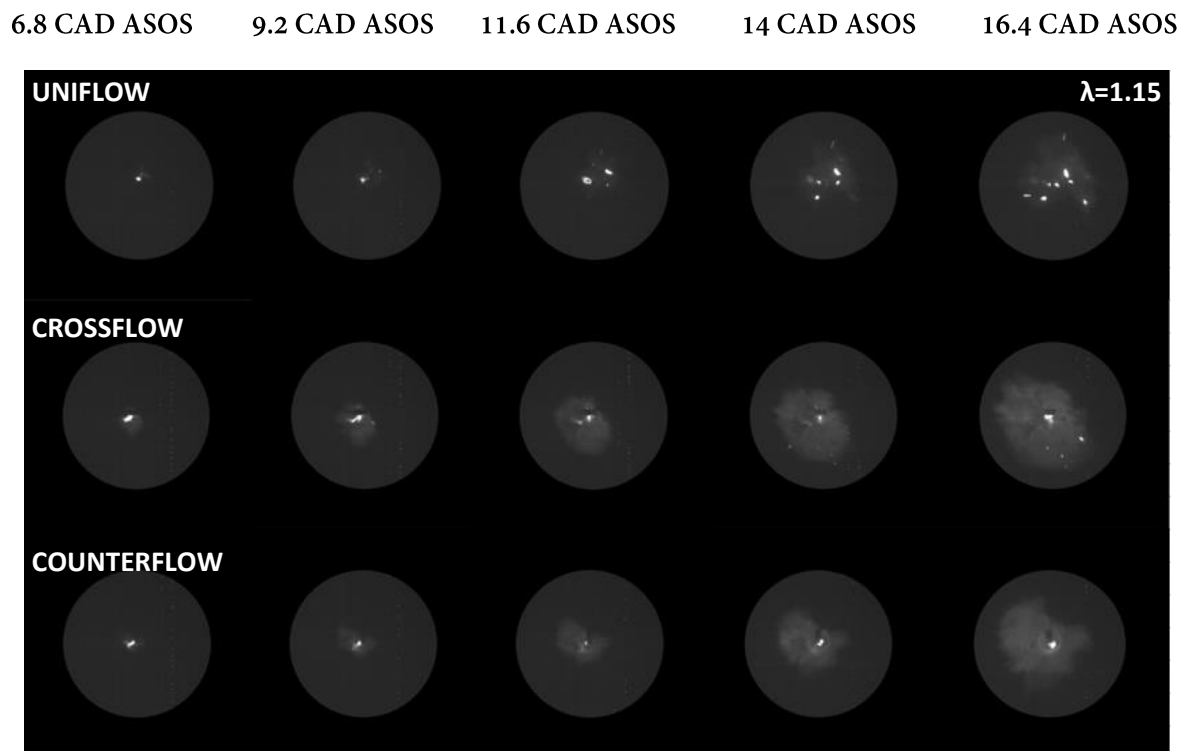


Figure 5. 20, Flame image sequence during the flame propagation stage, $\lambda=1.15$, SA12 CAD.

6.8 CAD ASOS 9.2 CAD ASOS 11.6 CAD ASOS 14 CAD ASOS 16.4 CAD ASOS

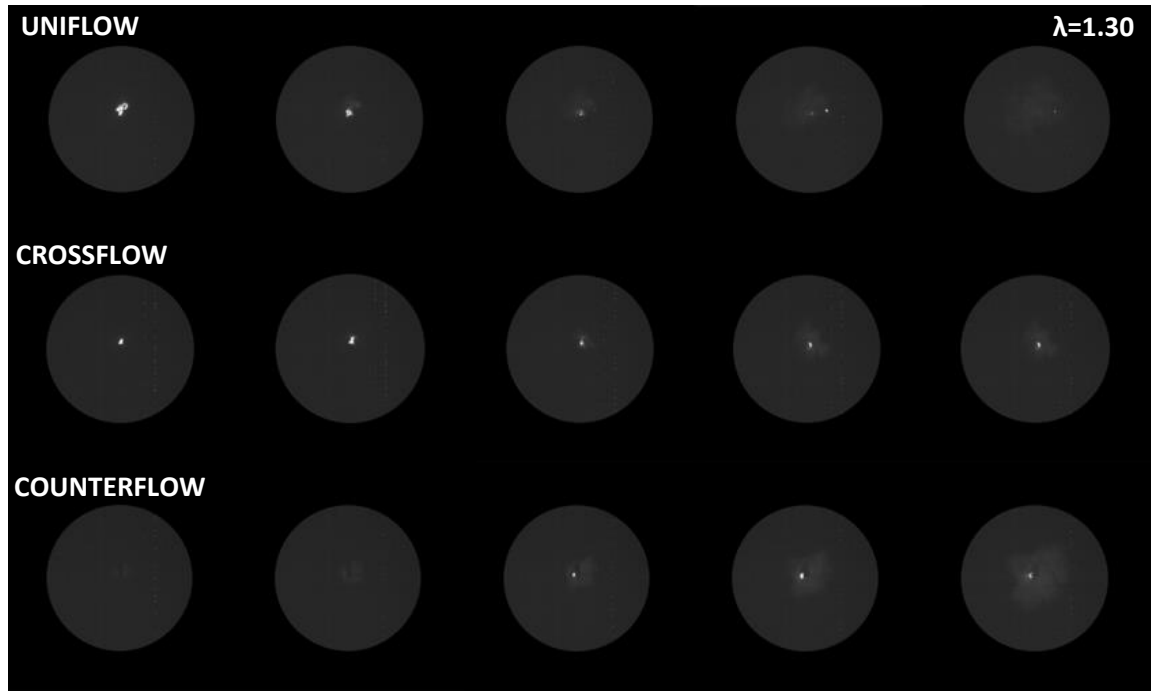


Figure 5. 21, Flame image sequence during the flame propagation stage, $\lambda=1.30$, SA12 CAD.

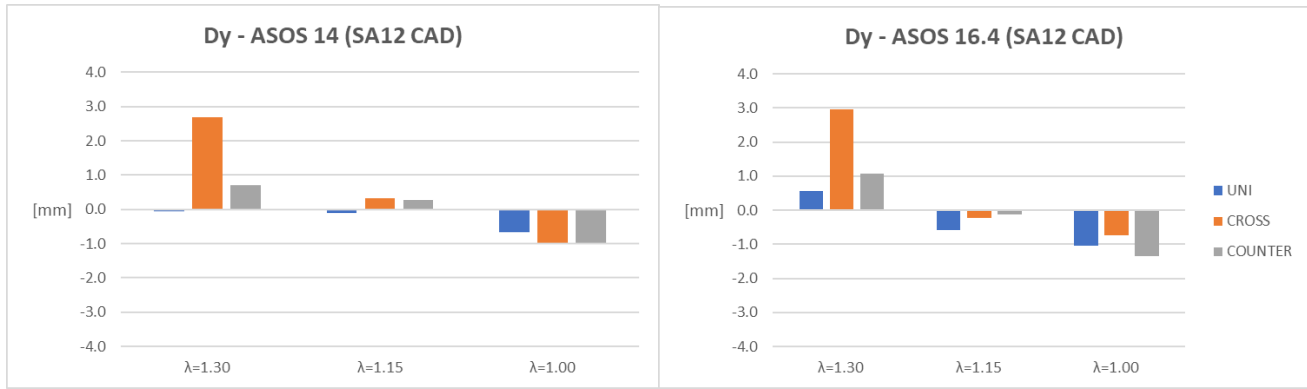
The flame sequences reported in Figures 5.19 to 5.21 correspond to the cycles with the Volume Fraction Burned (VFB) traces closest to the average. It is intuitive to state that the operative condition with the leanest blend caused the greatest difficulty in the optical analysis. Poor luminosity of the reaction zone it impossible to use the first frames after spark ignition. For this reason, to compare the images (therefore the flame area morphology) corresponding to the same Crank Angle Degree, it was decided to analyse the frames related to 14 and 16.4 CAD ASOS. The next step concerned the analysis of flame area center positioning during the early stages of combustion. To do this, it was necessary to define a point of reference starting from the position of the spark plug (rendered possible by the use of the “Measure” function in NI Vision) and to know the relative location of the flame area instant by instant. To calculate the dislocation along the horizontal and vertical axis of the flame area with respect to the spark plug, the following equations were used,

$$Dx = (X_{Flame\ Area\ Center} - X_{Spark\ Plug\ Center}) * 0.187,$$

$$Dy = -(Y_{Flame\ Area\ Center} - Y_{Spark\ Plug\ Center}) * 0.187,$$

where the coordinates of flame area center were obtained using a specific tool in NI Vision (function “Particle Analysis”), while the last term is used to convert the dimension from pixels to millimetres (5.3 pixels \sim 1 mm). Finally, looking at the equation used for calculating the displacement along the vertical axis, the inversion of sign is related to the fact that in NI Vision the reference system sees the y coordinate increase downwards (i.e., the 0,0 coordinates are located in the upper-left corner of the user interface). Now it is possible to proceed with the evaluation of the displacements along the horizontal and vertical axis with respect to the spark plug center and by these calculate the radial displacement with the following equation,

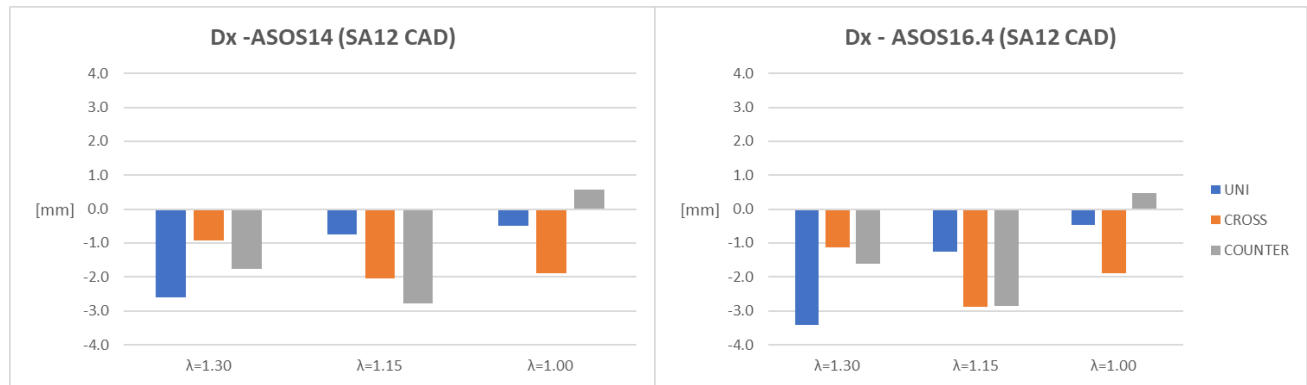
$$R = \sqrt{Dx^2 + Dy^2}$$



(a)

(b)

Figure 5. 22, Displacement along the vertical axis respect to the spark plug center, (a) frame at 14 CAD ASOS, (b) frame at 16.4 CAD ASOS.



(a)

(b)

Figure 5. 23, Displacement along the horizontal axis respect to the spark plug center, (a) frame at 14 CAD ASOS, (b) frame at 16.4 CAD ASOS.

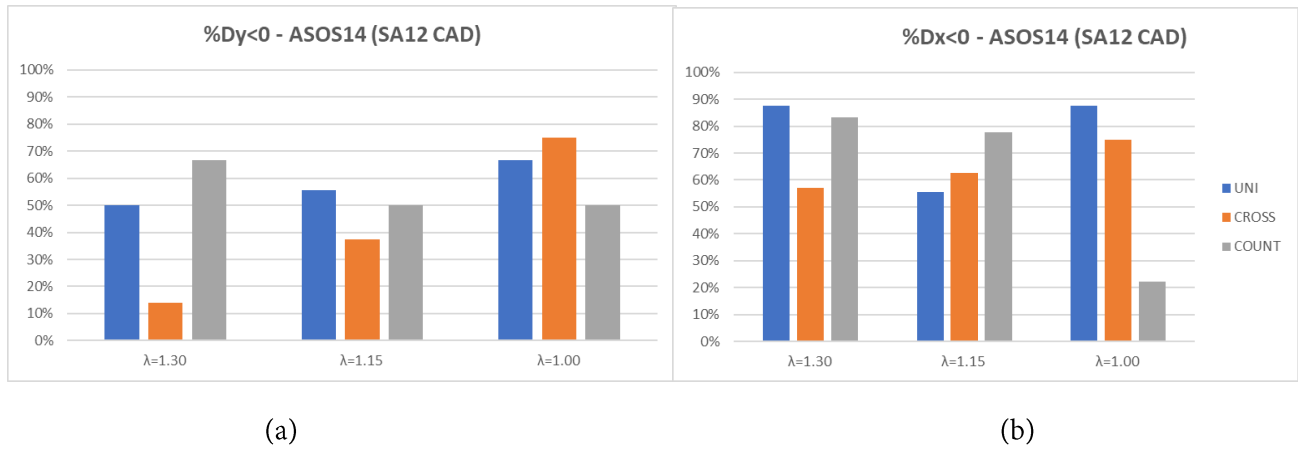


Figure 5. 24, (a) Percentages of Up-Down events, (b) Percentages of Right-Left events for frame at 14 CAD ASOS, SA12 CAD.

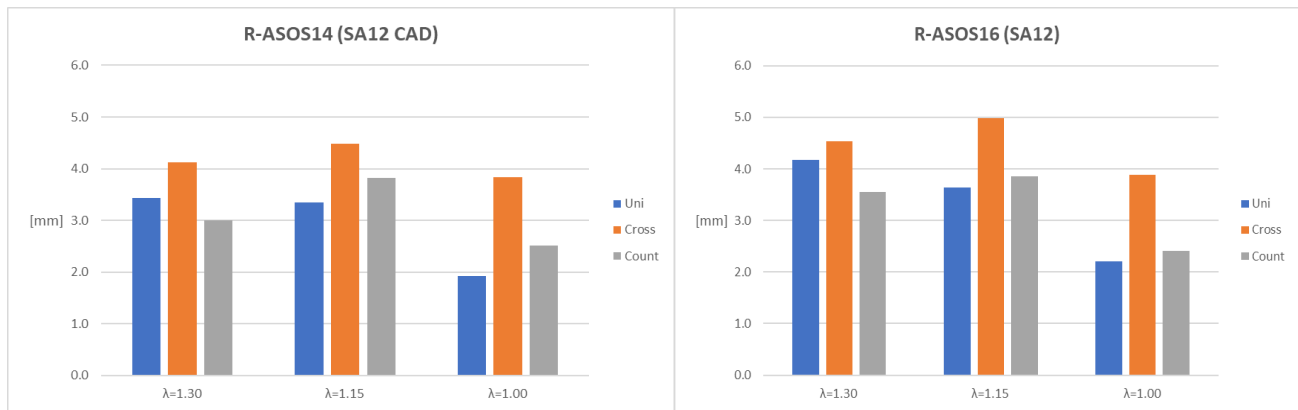


Figure 5. 25, Radial displacement of flame area center respect to the spark plug center for frames at 14-16.4 CAD ASOS.

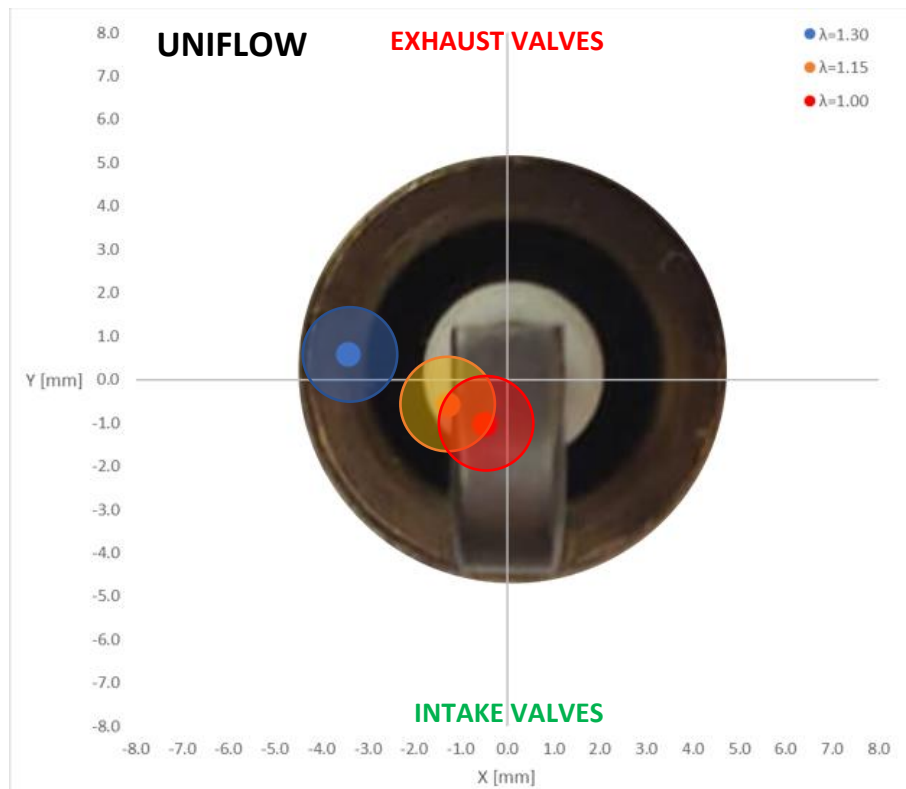


Figure 5. 26, Flame area center locations for the Uniflow configuration for frame at 16.4 CAD ASOS, SA12 CAD.

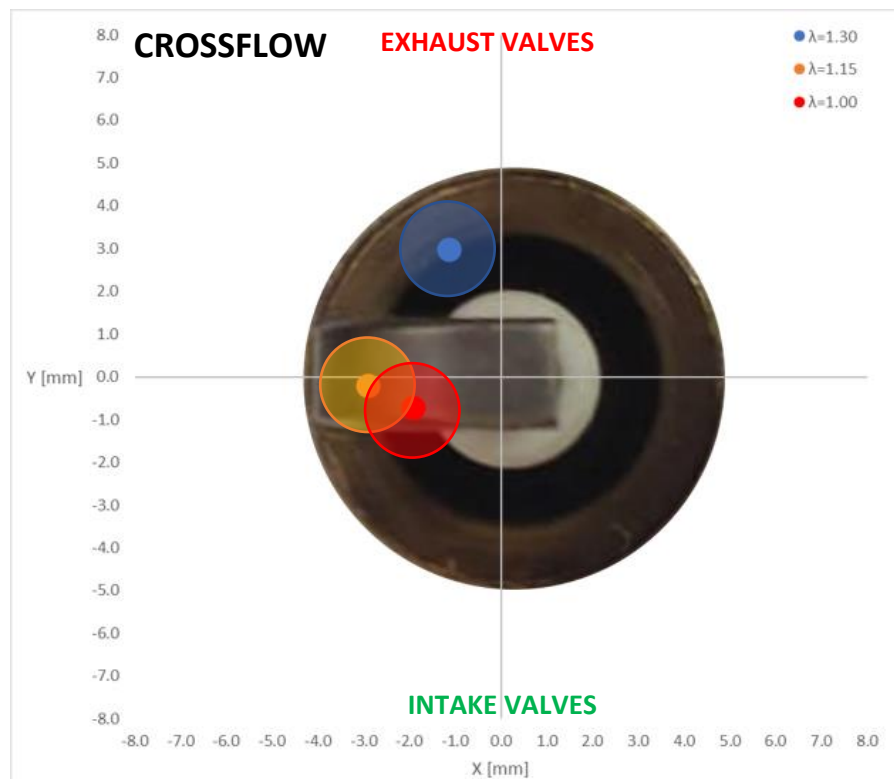


Figure 5. 27, Flame area center locations for the Crossflow configuration for frame at 16.4 CAD ASOS, SA12 CAD.

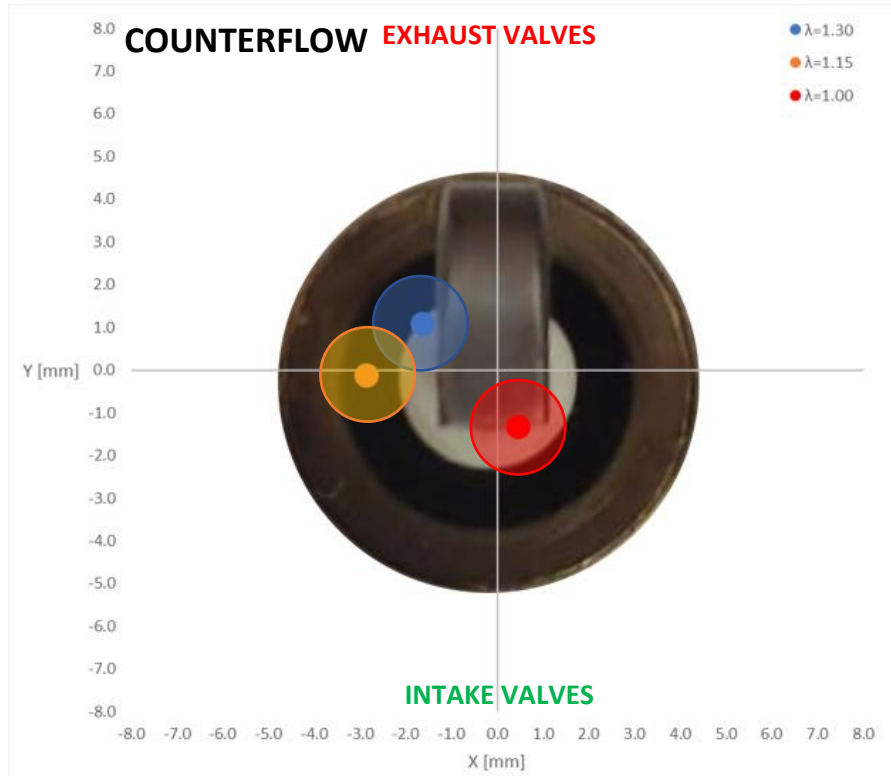


Figure 5. 28, Flame area center locations for the Counterflow configuration for frame at 16.4 CAD ASOS, SA12 CAD.

For all orientations, once the spark ignition advance is fixed, it is possible to observe (Figure 5.22, 5.26 to 5.28) the tendency of the flame kernel to move from the exhaust valves to the intake valves as the mixture ratio varies, thus passing from lean to stoichiometric. As expected, in terms of vertical displacement variation, the effect is more evident with the Crossflow configuration. In fact, the latter is more exposed to the tumble motion. Figure 5.24 shows the percentages of up-down and left-right events. Uniflow and Crossflow configurations show an increasing trend with richer blends for the first category. In Counterflow, on the other hand, the trend is decreasing. Passing to the analysis of displacement along the horizontal axis, for all configurations, an evident flame kernel displacement towards the left side of the spark plug was detected (Figure 5.23, 5.26 to 5.28), although it is not possible to identify a defined trend with the air-fuel ratio value. The only exception is represented by the Counterflow configuration which in the case of a stoichiometric mixture presents a positive value. Furthermore, with the same fluid dynamic conditions (same spark advance), no univocal trend can be observed in the percentage variation of displacements along the horizontal axis, Figure 5.24 (b). Finally, the Crossflow configuration (in line with what has been said for the evaluation of dy and in the thermodynamic results paragraph) shows the

greatest dislocation values of the center of mass with respect to the spark plug, in all cases (Figure 5.25). Overall, the distance of the flame area center from the spark plug increases passing from $\lambda=1.30$ to $\lambda=1.15$, then decreases for the stoichiometric operative condition.

5.3.2 Optical Results for Fixed Lambda (λ)

As for the thermodynamic data, the following results are related to the operative conditions for a fixed AFR and variable SA. This optical analysis allowe to have better understanding of flame-fluid interaction for different fluid-dynamic conditions.

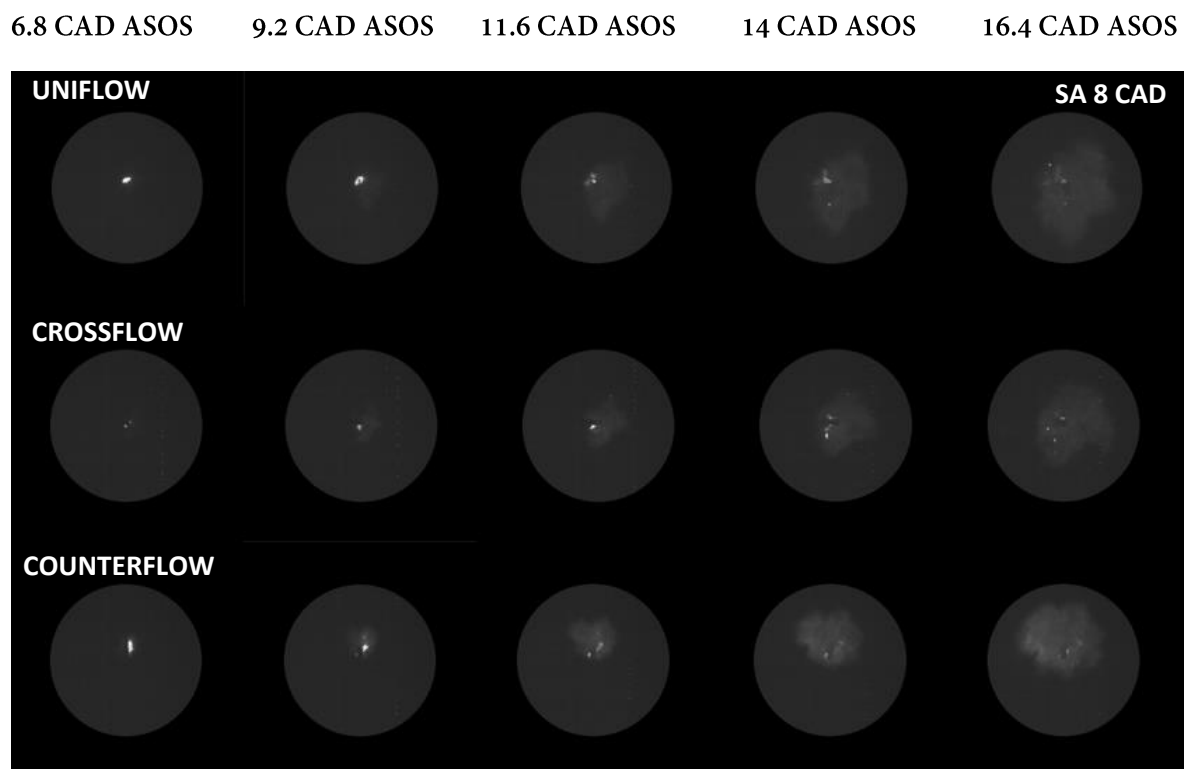


Figure 5. 29, Flame image sequence during the flame propagation stage, SA8 CAD, $\lambda=1.15$.

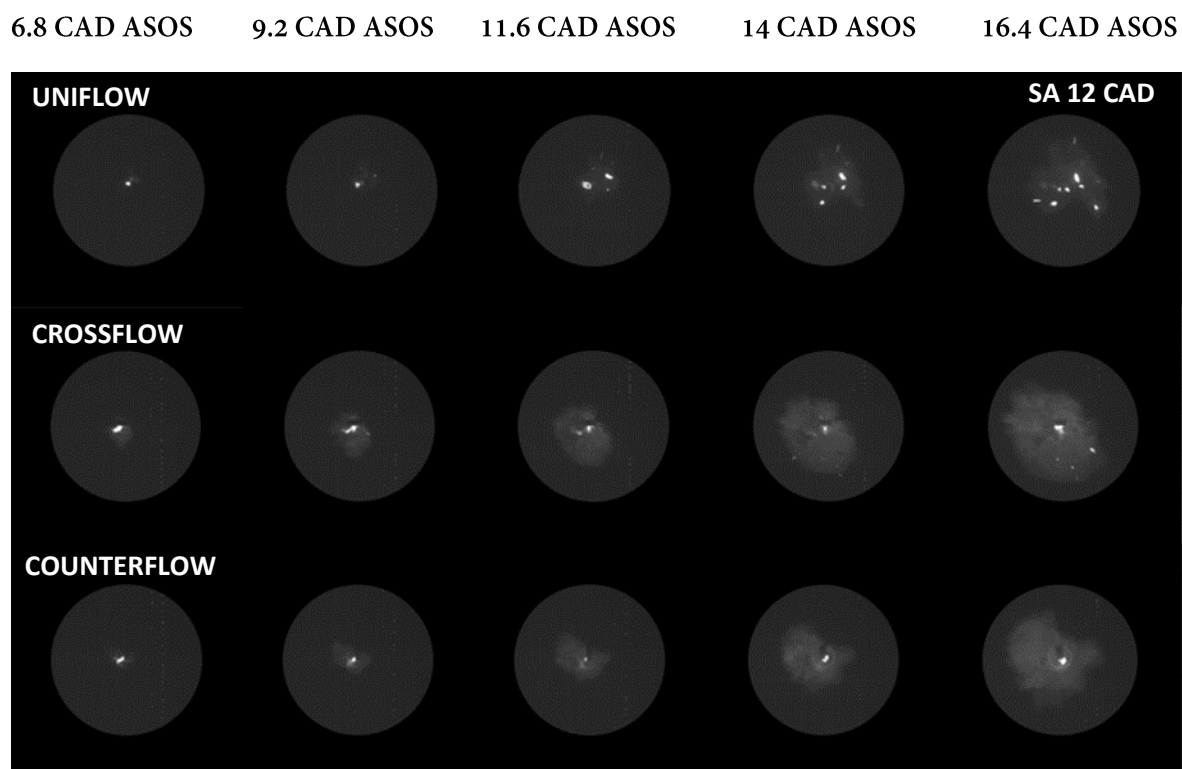


Figure 5. 30, Flame image sequence during the flame propagation stage, SA12 CAD, $\lambda=1.15$.

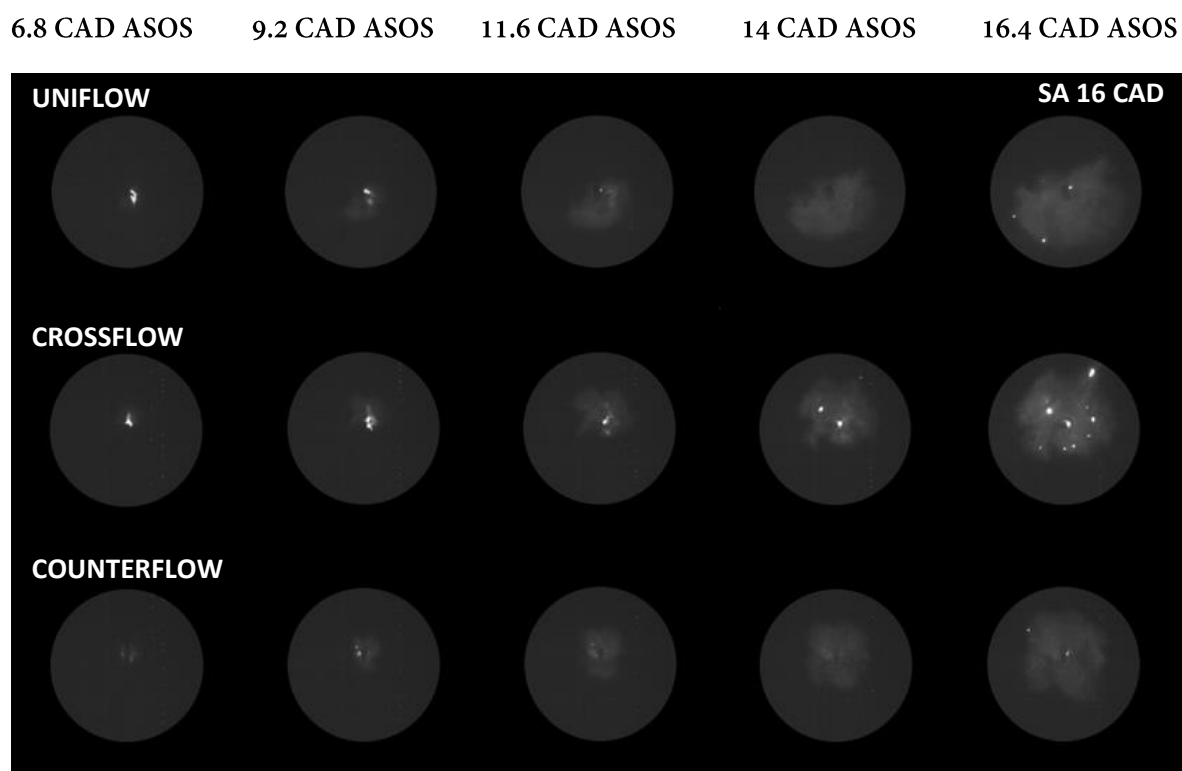


Figure 5. 31, Flame image sequence during the flame propagation stage, SA16 CAD, $\lambda=1.15$.

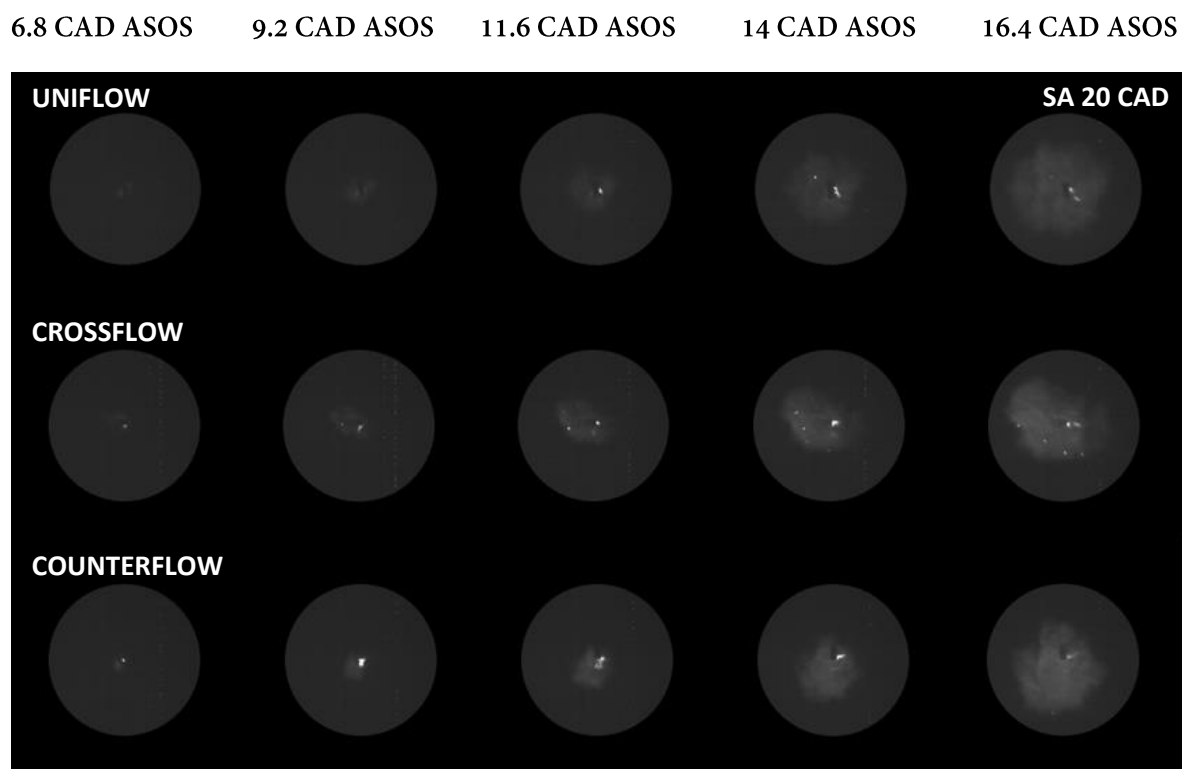


Figure 5. 32, Flame image sequence during the flame propagation stage, SA20 CAD, $\lambda=1.15$.

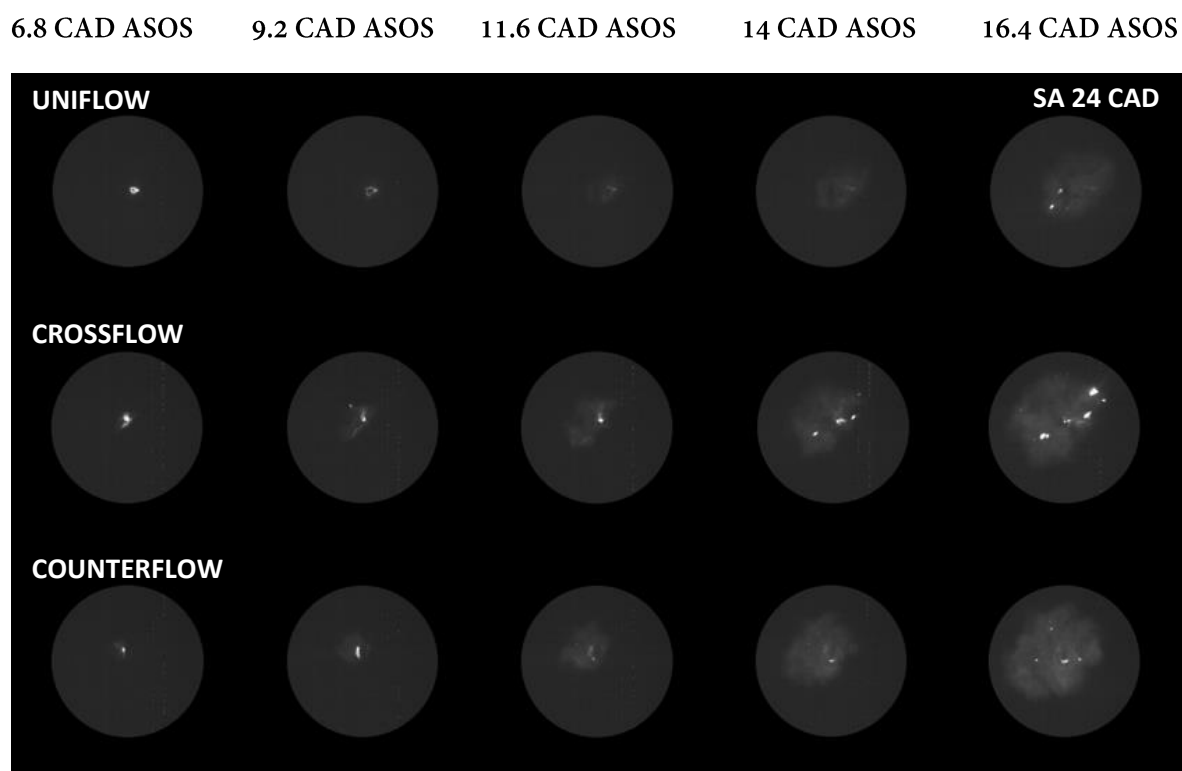
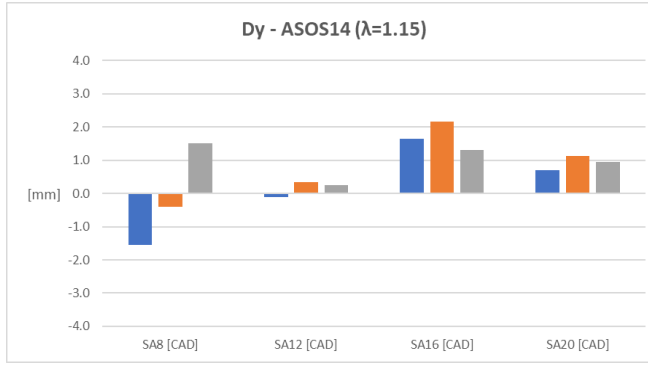
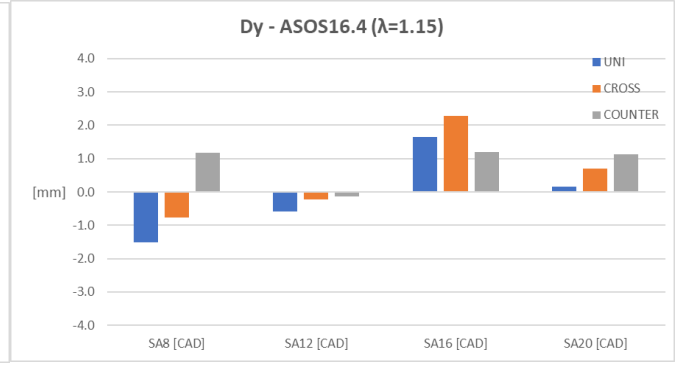


Figure 5. 33, Flame image sequence during the flame propagation stage, SA24 CAD, $\lambda=1.15$.

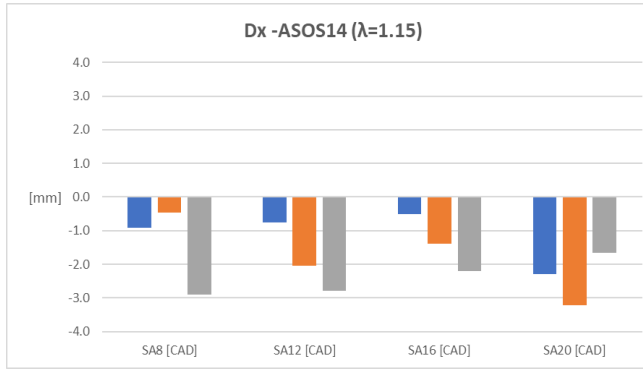


(a)

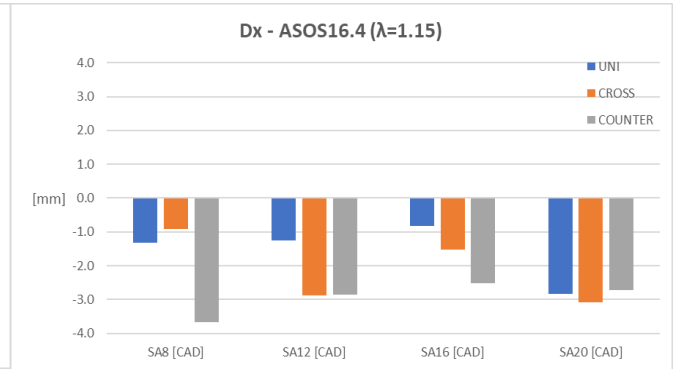


(b)

Figure 5. 34, Displacement along the vertical axis respect to the spark plug center, (a) frame at 14 CAD ASOS, (b) frame at 16.4 CAD ASOS.

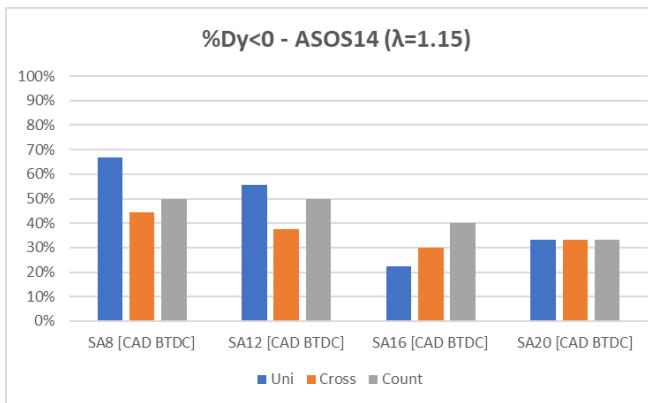


(a)

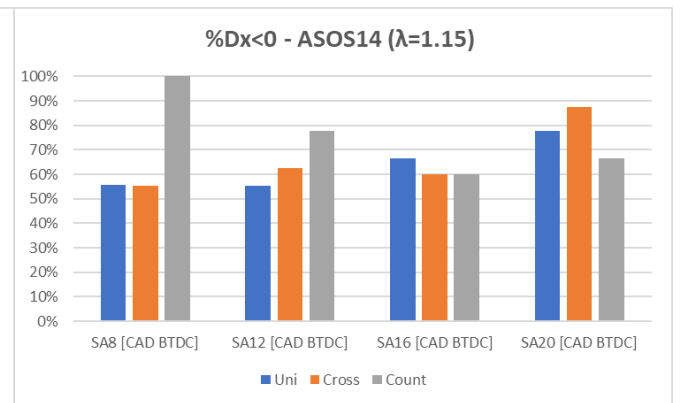


(b)

Figure 5. 35, Displacement along the horizontal axis respect to the spark plug center, (a) frame at 14 CAD ASOS, (b) frame at 16.4 CAD ASOS.



(a)



(b)

Figure 5. 36, (a) Percentages of Up-Down events, (b) Percentages of Right-Left events for frame at 14 CAD ASOS, $\lambda=1.15$.

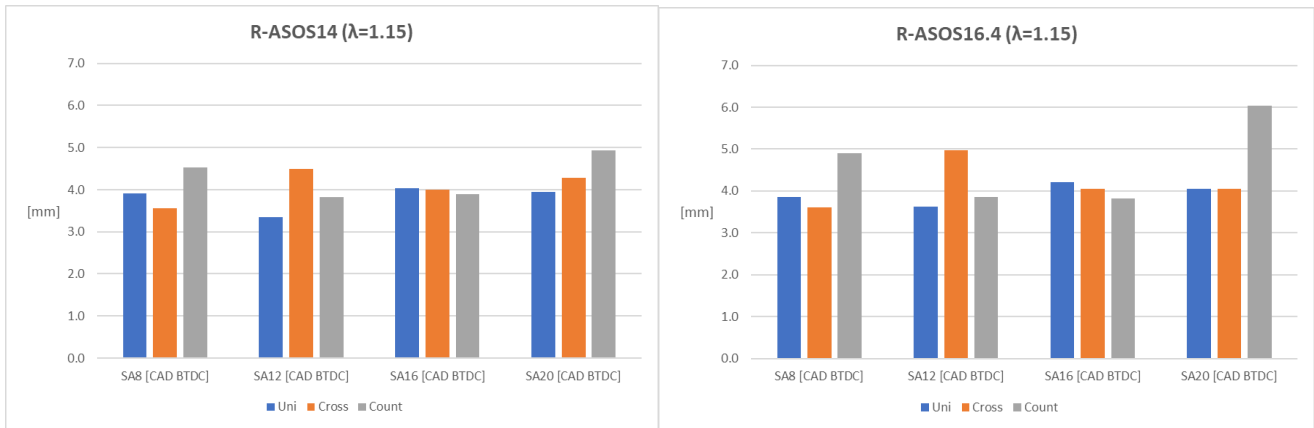


Figure 5. 37, Radial displacement of flame area center respect to the spark plug center for frames at 14-16.4 CAD ASOS, $\lambda=1.15$.

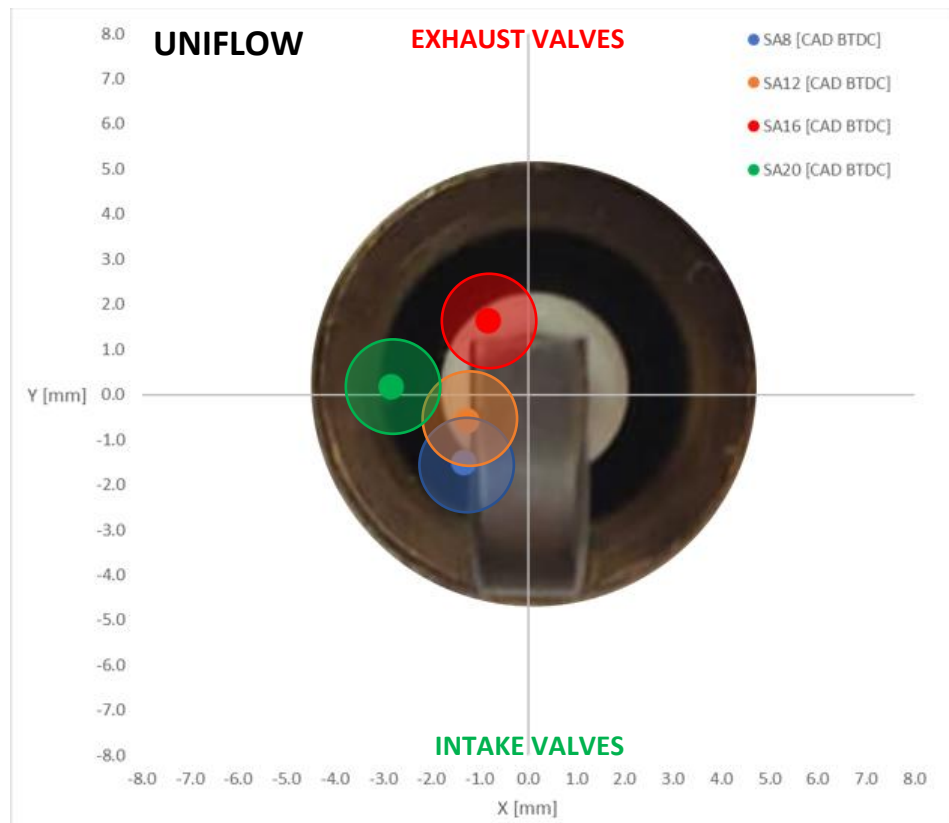


Figure 5. 38, Flame area center locations for the Uniflow configuration, $\lambda=1.15$, frame at 16.4 CAD ASOS.

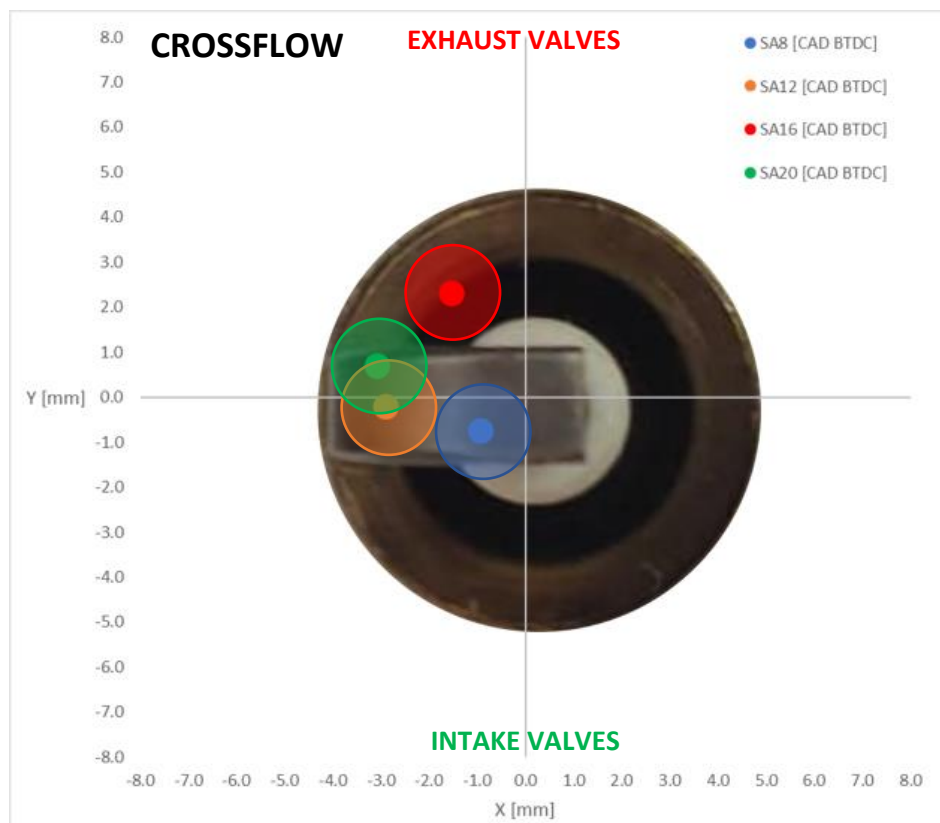


Figure 5. 39, Flame area center locations for the Crossflow configuration, $\lambda=1.15$, frame at 16.4 CAD ASOS.

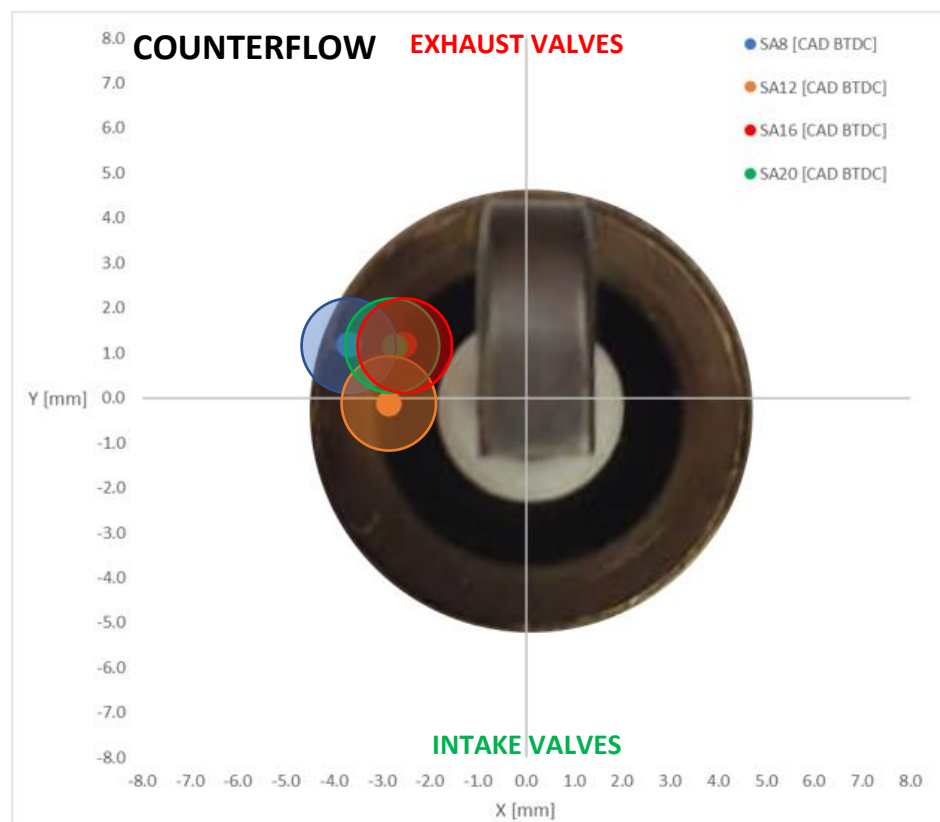


Figure 5. 40, Flame area center locations for the Counterflow configuration, $\lambda=1.15$, frame at 16.4 CAD ASOS.

Among the results shown, it is possible to note the absence of the ones related to the operative condition for the Spark Advance (SA) of 24 CAD. The latter proved particularly difficult to analyse due to repeated presence of luminous points in the sequence recorded. In fact, these made it difficult to obtain accurate results (the script was unable to distinguish the flame front). Therefore, the reported results do not consider this particular operative condition. For all orientations, once the mixing ratio is fixed, looking at the Figure 5.34, a quadratic trend of the displacement of the kernel is visible as the ignition advance increases (up to SA16 CAD, i.e., up to achieve the MBT condition). One exception is observed in the case of Counterflow in delayed conditions (SA8 CAD). The percentages of up-down events, figure 5.36 (a), confirm the reversal of the trend as the ignition advance increases. An evident displacement to the left side of spark plug of the flame kernel was detected (figure 5.35). This trend is to be attributed to a slight swirl motion that seems to have a greater influence on the ignition of combustion in the Cross and Counterflow configurations. The effect appeared to amplify as the ignition advance increases for Uni and Crossflow cases, while the Counterflow configuration is an exception showing a slightly decreasing trend. Looking at the percentages of $D_x < 0$ (figure 5.36 (b)) it seems that the counterflow configuration is in contrast with the others. For the radial displacement no-well defined trend was observed (figure 5.37). As an overall conclusion of this analysis, it is important to note the differences in terms of spatial distribution of flame area, even when the thermodynamic results indicated no particular trend, with practically the same engine output and stability figures. Certainly, further analyses are needed, with acquisition of more data to examine specific effects. An interesting example is the behaviour of the counterflow configuration that seems to have an opposite trend if compared with the Uniflow and Crossflow configurations.

5.4 Flame Front Velocity Analysis

The analysis of the propagation speed of the flame front, was carried out only for the operative conditions for a fixed AFR ($\lambda=1.15$) and variable spark timing. This specific investigation can be linked to the previous studies performed [19]. Thanks to the same orientations of the spark plugs, it is possible to compare those results obtained with the ones in this thesis. The velocity values were obtained using a dedicated tool of NI Vision; in fact, thanks to the “Particle analysis” function, it was possible to know the Feret Diameter of the flame front area for each frame that was acquired. This simplified approach made it possible to study the effect of turbulence motion on the different spark plug configurations, and to have better comprehension of flame-fluid interaction behavior for different spark ignition timing. Figure 5.41 shows the propagation speed of the flame front.

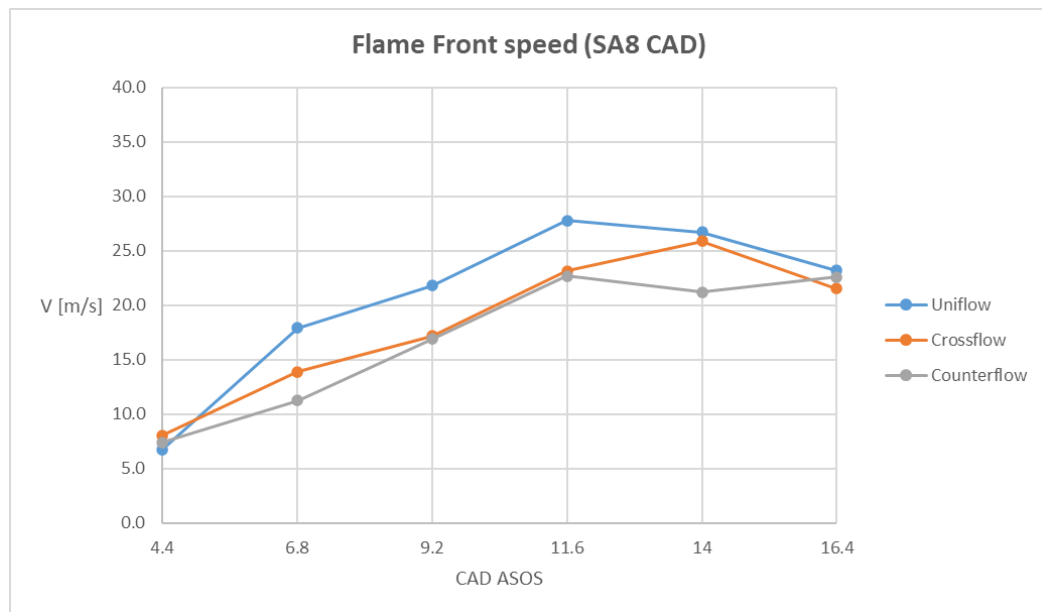


Figure 5. 41, Flame Front speed, SA8 CAD.

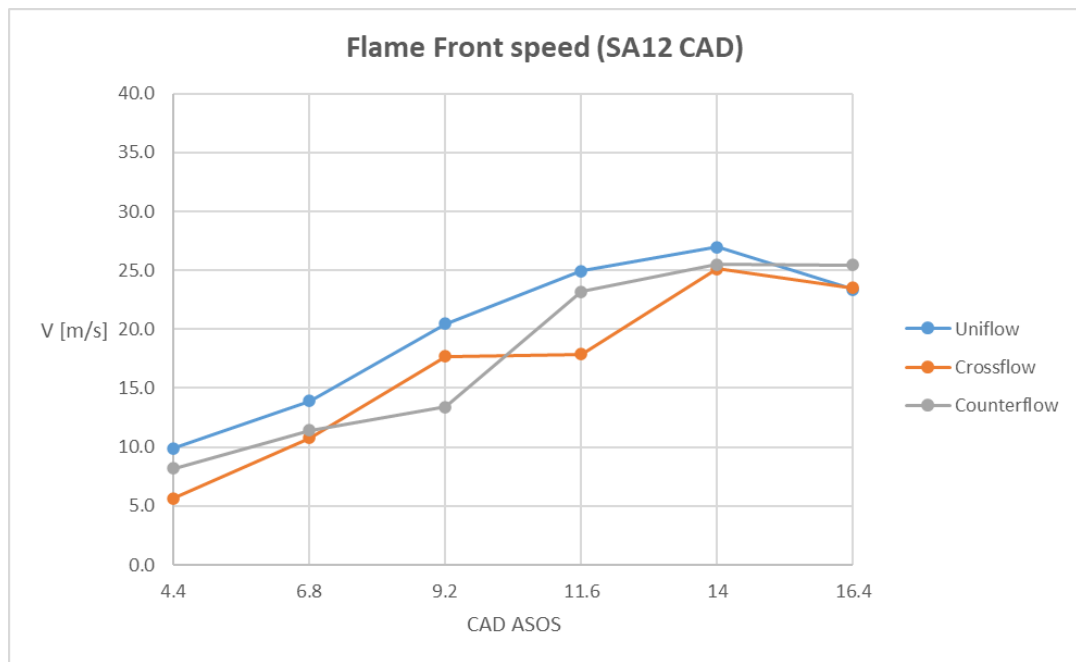


Figure 5. 42, Frame Front speed, SA12 CAD.

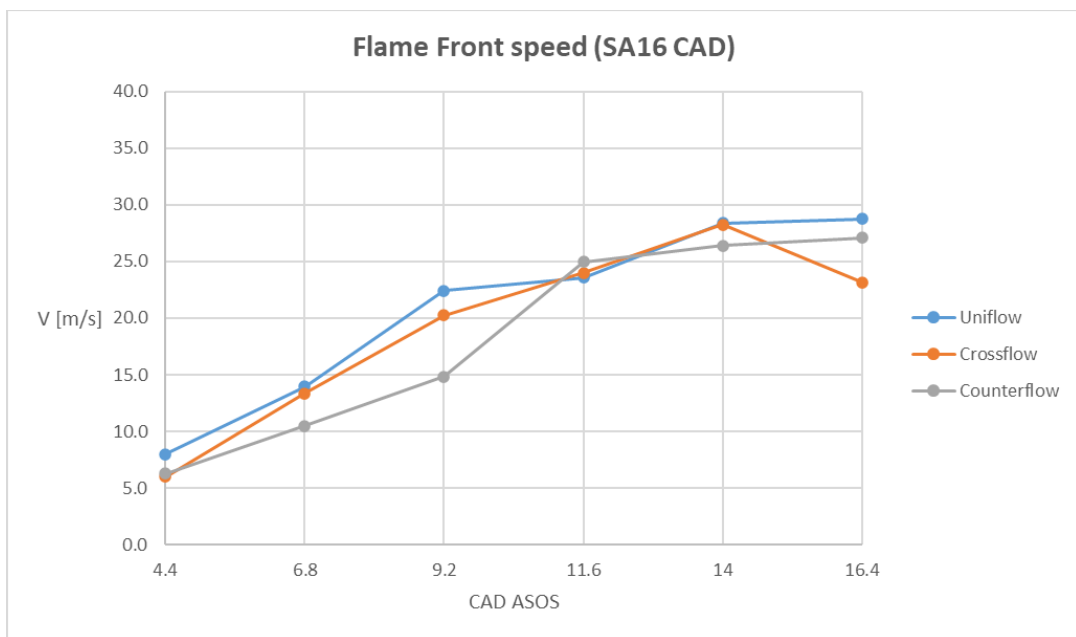


Figure 5. 43, Frame Front speed, SA16 CAD.

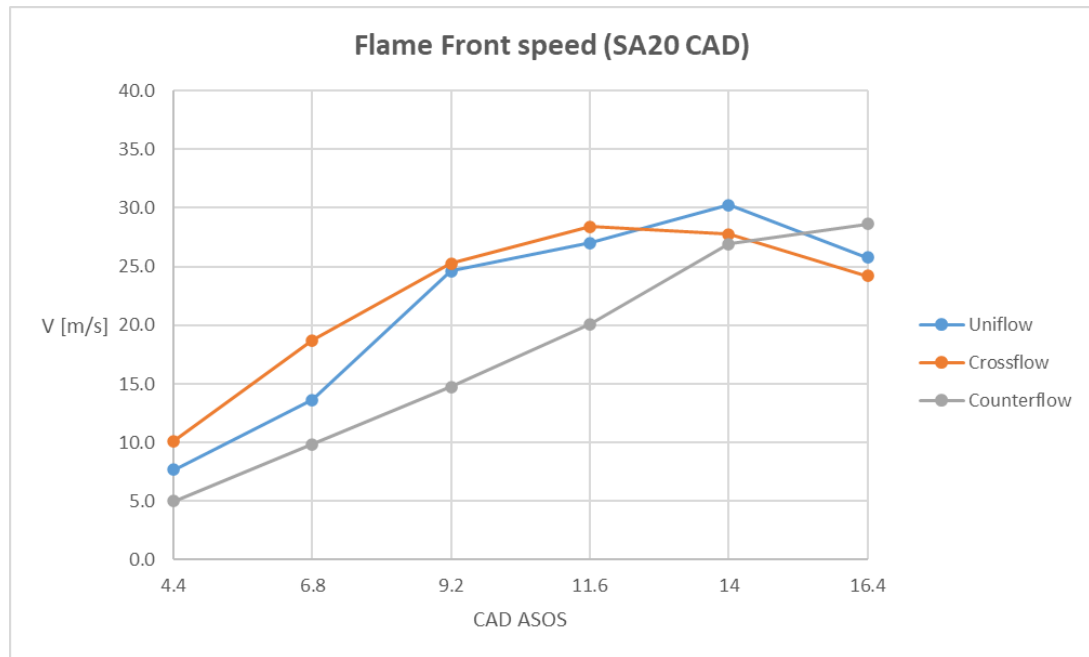


Figure 5. 44, Frame Front speed, SA20 CAD.

A common trend of increasing propagation speed can be noted as the flames increase in size (i.e., as the process evolves). All configurations seem to feature a value of around 20-30 m/s propagation velocity that can be considered as representative for the main combustion phase. No clear influence of plug orientation was identified, but as an overall effect, the Uniflow configuration tended to feature “faster” propagation and Counterflow was the “slowest”. As expected, the flame-fluid velocity is highly dependant on spark timing. Similar values can be expected for turbulence intensity at TDC [19], while the combined effect of direct influence of tumble and its conversion into turbulence require further information of fluid motion (e.g., from numerical simulation).

Chapter 6

GT-Power Model

To gain further insight into phenomena that place inside the combustion chamber (such as tumble motion, turbulence, blow-by losses, etc.), a model of the optically accessible DISI engine was built in the GT-Power environment [39]. The main goal was to evaluate the applicability of the combustion SITurb sub-model; to this end, calibration for a set of operative conditions was attempted. In this way, it is possible to define a certain predictability level of the model (considering the difficulties related to the intrinsically customized nature of the type of the engine used for this study). After a description of the aforementioned model and methodology used for the numerical application, a brief evaluation of simulation results is presented.

Figure 6.1 shows an overview of the model. Rather than showing detailed specifics of the different elements, it highlights the logic behind the simulation tool. Reading from top to bottom, air from an inlet environment component (illustrated as a green filled rectangle) is aspirated by the engine through the intake system, while combustion products are transferred through the exhaust system to an outlet environment. More to the point, each element is mainly intended to define a certain sub-volume of the intake-cylinder-exhaust series, connected between them with dedicated data flow links. For example, the intake manifold (shown as a series of T elements connected to runner pipes) is linked to the cylinder (intuitively identified with a piston a schematic representation of a propagating flame) through two ports and corresponding valves. These two links transport the working fluid backwards or forwards based on the pressure difference and effective discharge area. From the cylinder to the crank-train (shown as four piston-connecting rod assemblies with a common crankshaft) only kinetic energy is transferred (e.g. constant engine speed was imposed, and thus the crank-train component compensates torque variations due to the changes of in-cylinder pressure). Other connections are intended as signals (illustrated with blue colour lines) used for monitoring purposes (e.g. relative air-fuel ratio in the exhaust line) or for establishing specific targets used by the genetic algorithm optimizer for finding calibration parameters.

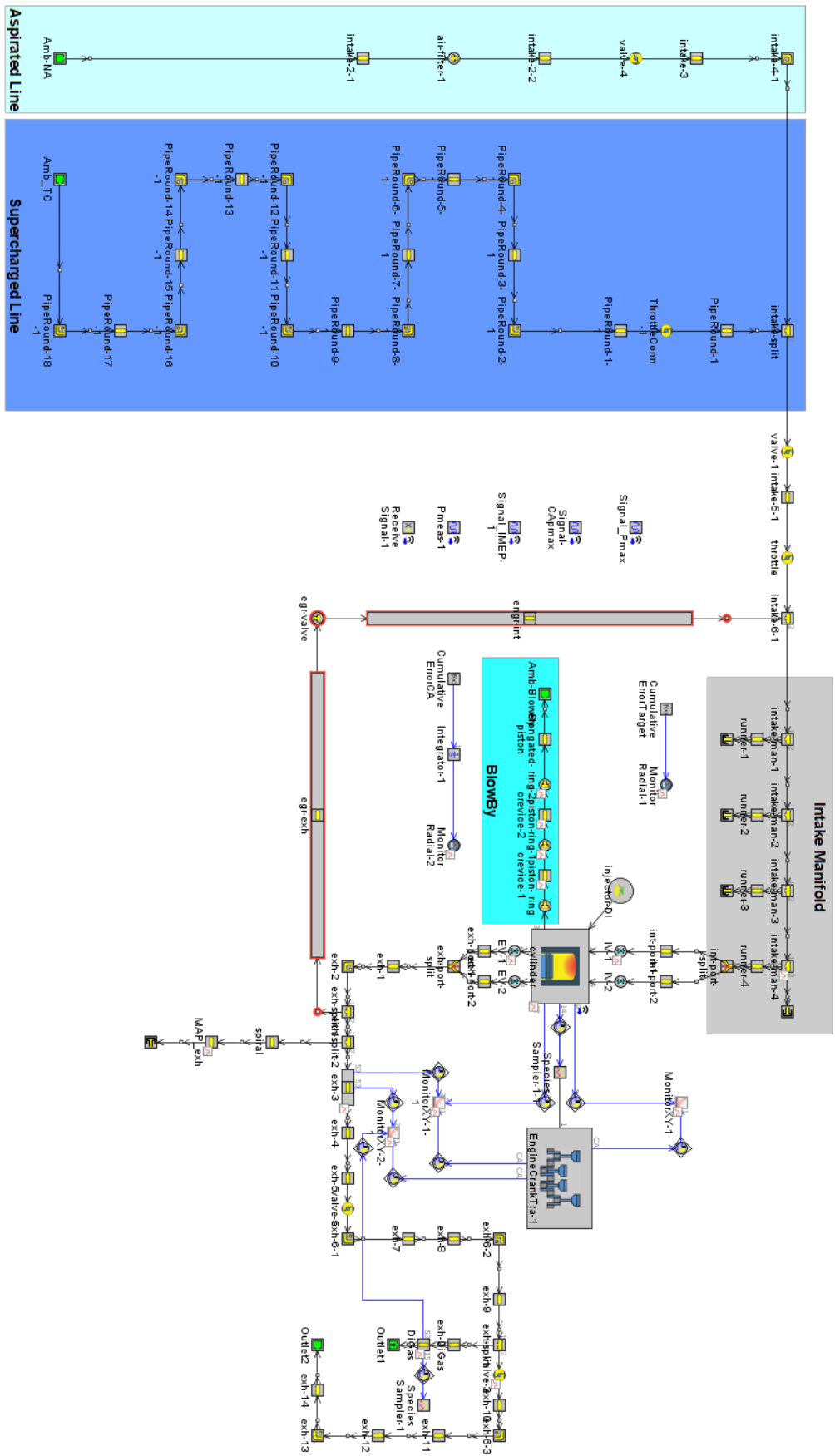


Figure 6. 1, Gt-Power simulation model.

6.1 Overall Calibration of the GT-Power Model

One of the first steps of the calibration was to check that intake pressure levels were correctly predicted during the intake stroke. Slight adjustments of the inlet environment pressure were required (1-2 percentage points around 1 atm). As figure 6.2 shows, in-cylinder pressure at intake valves closure (i.e. 216 CAD ATDC at the end of the exhaust stroke) was correctly modelled.

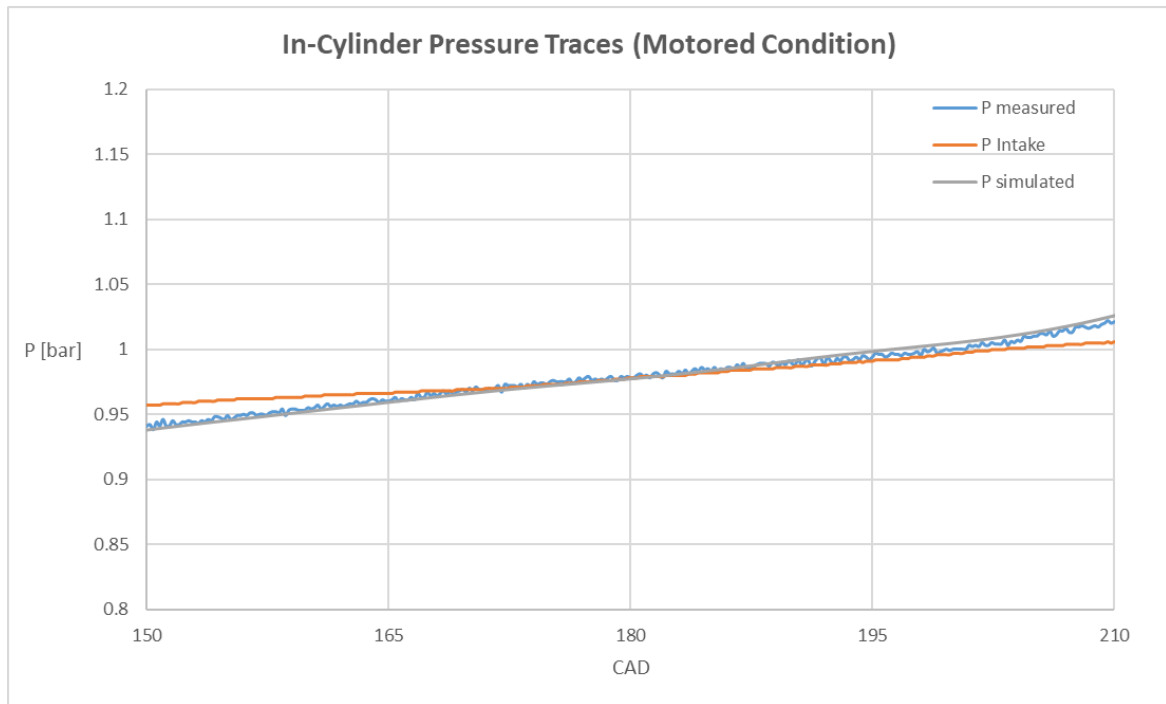


Figure 6. 2, In-Cylinder Pressure during the intake-stroke, motored condition.

Once the intake air quantity was validated as correct for ensuring valid cycle start conditions, attention was paid to the compression-expansion processes. Starting with motored pressure traces, adjustments were applied to the effective compression ratio (through changes in the geometric ratio as well as adjustments of the crevice volumes) that was not as straight forward to set as for commercial engines.

To better characterize the blow-by losses, a specific sub-model was elaborated (highlighted in light blue close to the cylinder component in figure 6.1), so as to be representative for the specific geometry of each piston ring volume (Chapter 2, Figure 2.8); this series of orifices and volumes was linked to the single-cylinder component on one end, and the environment at the other. The blow-by sub-model is divided into three sealing rings and is directly connected to the crankcase (whose setting are the same of the external environment, $P_{\text{CRANKCASE}}=1$ atm and $T_{\text{CRANKCASE}}=288$ K).

Given the very design of the elongated piston, slight changes in the geometric compression ratio are possible due to thermal expansion. Hence, the compression ratio and blow-by orifices were calibrated using the motored pressure traces. It was found that indeed, higher compression ratio values were required for fired conditions in order to obtain the correct pressure level at the time of ignition.

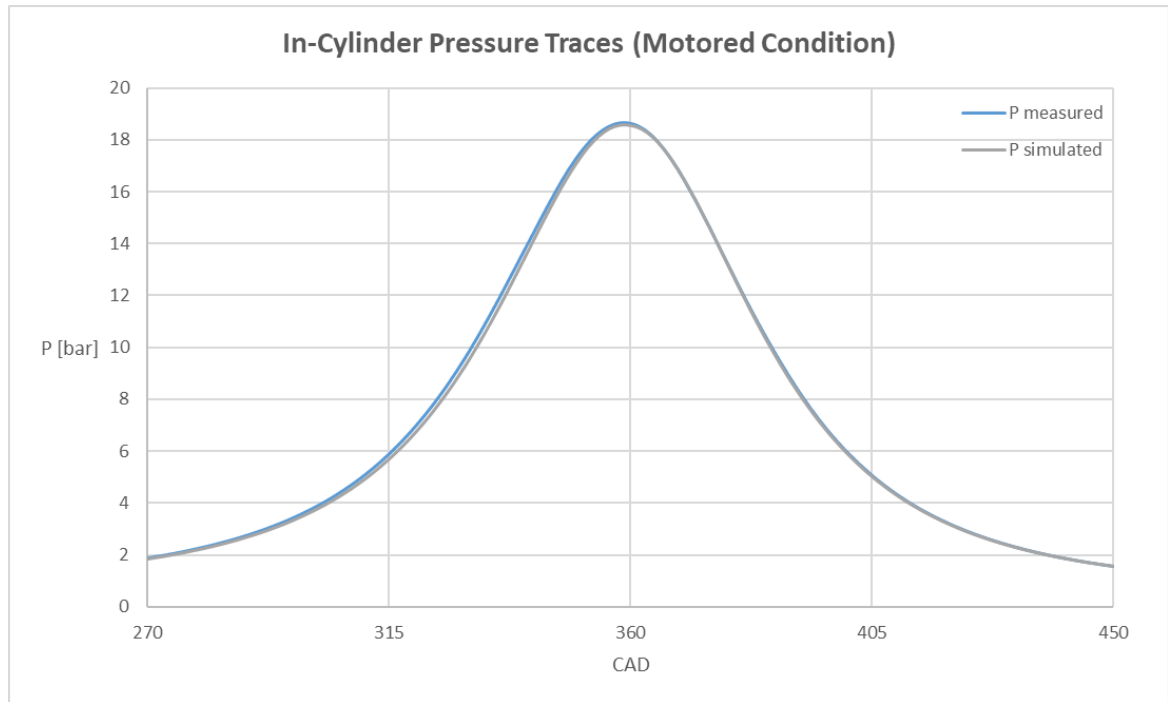


Figure 6. 3, In-Cylinder Pressure Traces Comparison, motored condition.

Figure 6.3 shows the comparison between the measured and simulated in-cylinder pressure traces in motored conditions. There is good accuracy of simulation throughout the cycle. As previously stated in the second chapter, the CR value is around 10 for the motored operative condition, while during in-firing operations, the thermal effects (considering the presence of the elongated piston) and mechanical stress can influence the latter with consequent variations in its value. Therefore, the maximum increase registered was noted for the operative condition for a spark advance of 24 CAD with a CR of 10.5, hence an increase of 5% with respect to the motored operative condition. This particular trend was found to be consistent with higher peak pressure levels as spark timing was advanced, resulting in increased heat transfer rates and therefore higher piston temperature and consequent larger expansion effects (effectively reducing piston-head clearance).

On the other hand, with the experimental data such as oil and coolant system temperature values, recorded during the motored and in-firing operative conditions, it was possible to define a thermal regime of each component of the GT-Power model. For the motored operative condition, the in-cylinder wall temperature was set equal to the same value of coolant system. During fired operation instead, higher piston temperature was imposed (e.g. over 500 K compared to around 370 K for motored conditions), so as to match the calibrated compression ratio value. Nonetheless, this was found to be of secondary importance when undertaking calibration of the combustion sub-model.

For a better reproduction of the combustion chamber, a 3D CAD model was implemented in the GT-Power model through an STL file; this ensured correct definition of the flame area during combustion. Finally, measured tumble coefficients were implemented for the intake valve components, so as to ensure correct modelling of tumble and turbulence. Given that no other data was available in this respect (e.g. cold-flow CFD simulations), all calibration parameters were set at their default values for the flow sub-model that calculates fluid velocity. Finally, the crevice sub-model was activated, and its volume was implemented based on measured bore-piston dimensions and related expansion effects during fired operation.

6.2 Combustion Sub-Model Calibration

Gas exchange, compression and expansion feature relatively low complexity compared to turbulent combustion. As shown in the previous sub-section, these processes were correctly modelled during motored operation, with minimal computational effort. Combustion instead features more calibration parameters, each related to a certain part of the process. These are the Flame Kernel Growth (FKG), Turbulent Flame Speed (TFS) and the Taylor Length Scale (TLS) multipliers. Additionally, the Dilution Effect Multiplier (DEM) can be adjusted for controlling the effect of residual gas on calculated laminar flame speed. As their names hint, FKG controls the transition from laminar to the turbulent flame speed regime (thus influencing mostly the initial stages of the process), TFS influences the rate at which fresh charge is entrained within the reaction zone (and indirectly links turbulence characteristics to combustion evolution), while TLS controls the rate of oxidation within the reaction zone.

The main goal of this part of the numerical analysis was the definition of a set of calibration parameters for the SITurb combustion model that can successfully simulate as many operating points as possible within the operative conditions that were investigated. Given the relatively reduced influence of spark plug orientation on thermodynamic parameters, the choice was made to consider only the uni-flow configuration. Flow model calibration parameters (in terms of tumble decay and turbulence production, length scale and so on) were set to their default values, as no other data was available for more detailed definition. The combustion model was set to v2019, the most recent version recommended by Gamma Technologies for the calibration of the predictive numerical model. The methodology used to perform this analysis involved the use of the optimization tool in GT-Power. Figure 6.4 shows how the parameters were set for running the optimizer.

Attribute	Object Value
<input type="radio"/> OFF	
<input checked="" type="radio"/> Integrated Design Optimizer	
<input type="radio"/> Simple Optimizer	
Number of Objectives	
<input type="radio"/> Single Objective	
<input type="radio"/> Multi-Objective, Pareto	
<input checked="" type="radio"/> Multi-Objective, Weighted-Sum	
Case Handling	
<input type="radio"/> Optimize Each Case Independently	
<input checked="" type="radio"/> Case Sweep and Cross-Case Studies	
Search Algorithm	
Search Algorithm	Genetic Algorithm ▾
Population Size	def (=calculated) ...
Number of Generations	30 ...
Show Genetic Algorithm Settings	<input type="checkbox"/>
Integrated Design Optimizer Options	
Optimization Restart File	ign ...
Faster Runtime (Local Runs Only)	<input checked="" type="checkbox"/>
Maximum Number of Parallel Designs	1
Timeout Duration (minutes)	300
Save Design Files?	<input type="checkbox"/>
Automatic Data Suppression (Recommended)	<input checked="" type="checkbox"/>

Figure 6. 4, Optimizer parameters setting.

As suggested by Gamma Technologies, the Integrated Design Optimizer allows more advanced choices in terms of settings with respect to the Simple Optimizer attribute. “Multi-Objective, Weighted Sum” allows to combine multiple different response RLTs (i.e. single value results calculated after each simulated cycle) into a single objective function that gets minimized or

maximized. This option finds a single best design for the created objective function, and the objective function has a very specific definition, as described in the optimization manual. Therefore, this option is recommended over the “Pareto” procedure when all objectives correlate with each other. “Case Sweep and Cross-Case Studies” refers to the necessity to optimize more than one case with a common solution. The use of the “Genetic Algorithm” is recommended by the manual for all problems having medium to high complexity, which would result from many factors, the presence of one or more constraints, and non-linear characteristics. The “Population Size” when set to “def” is calculated with the following logic,

n	Population Size
3	10
4	16
5	20
6	26
7	30
8	40
9+	50

where “n” is the factors number that must be optimized. Therefore, the three parameters inserted as “Factors” were the Turbulent Flame Speed (TFS), Taylor Length Scale (TLS) and Flame Kernel Growth (FKG) multiplier, while the Dilution Effect Multiplier (DEM) was set to the default value (1, representative of the most operative conditions in an ICE). With a calculated Population size (3 factors correspond to 10 Population size elements) and an imposed Number of Generations of 30, an exhaustive number of combinations was guaranteed to find the optimal solution. Finally, the “Faster Runtime” option allows the optimizer to launch a single solver process and attempt to run all designs using it. Doing so can greatly decrease the overall optimization time. Regarding the three factors, it was necessary to analyse the sensitivity level for each one of them in terms of how simulated in-cylinder pressure is affected. This allowed the definition of an operative range that the optimizer can work with to find the optimal solution. To do this, for an arbitrary set of SITurb parameters (TFS = 1.9, TLS = 4.4 and FKG = 5.3, obtained through trial and error as an initial gross evaluation), a variation was applied for each parameter ($\pm 10\%$ from the starting value) to

study the effect on the pressure cycle as shown in figure 6.5 ($\lambda=1.15$, SA12 CAD, WOT and CR=10.25).

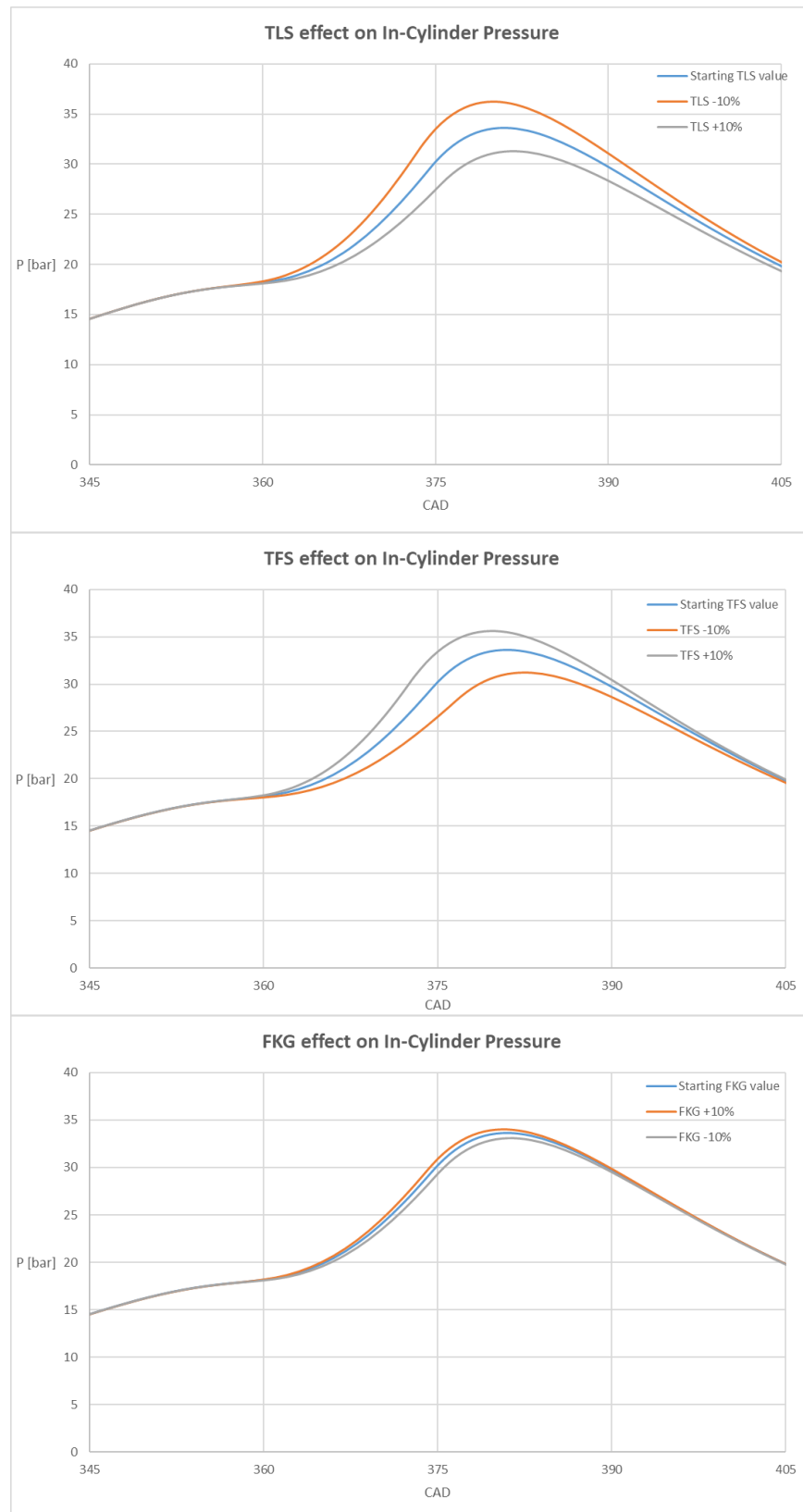


Figure 6. 5, SITurb parameters effect on In-Cylinder pressure.

It should be noted that only one parameter was varied at a time. On the basis of the obtained results, considering the starting values of SITurb, it is evident that the TFS has the greatest impact on the in-cylinder pressure traces with a set percentage of variation in its value. Therefore, considering the large number of operating conditions analysed and the consequent different resulting trace characteristics such as peak pressure, crank angle where it is reached and IMEP, it was decided to set the range limits shown in figure 6.6 for the three factors.

Attribute		1	2	3
Factor		TFS ...	TLS ...	FKG ...
<input type="radio"/>	Range	1.0	1.0	1.0
<input checked="" type="radio"/>	Lower Limit	0.8 ...	1.0 ...	4.0 ...
<input type="radio"/>	Upper Limit	4.0 ...	10.0 ...	10.0 ...
Integers Only		<input type="checkbox"/>	<input type="checkbox"/>	<input type="checkbox"/>

Figure 6. 6, Factors range limit setting.

Finally, the output signals of the MathEquations were set as RLT responses, with the aim of minimizing them. This component uses three input signals generated by using RLT values for peak pressure, its crank angle and IMEP, and calculates a sum of the difference between these three values and those obtained from the experimental data. In this way it was possible to calculate the error between the experimental values and the simulated ones (P_{max} , $CA_{P_{MAX}}$ and IMEP). Evidently, the output of the MathEquation component was used as a target to be minimized by the optimizer.

6.3 Simulation Model Results

As a first step, the optimizer was applied for the relative air-fuel ratio $\lambda=1.15$ with variable spark timing (8, 12, 16, 20 and 24 CAD BTDC). This was intended as in-between the two extreme values of air-fuel ratio that were investigated. Figure 6.7 shows the in-cylinder pressure traces obtained with the optimized calibration parameters. Acceptable results were obtained for spark timing of 8, 12 and 16 CAD BTDC, while the more advanced settings of 20 and 24 featured reduced accuracy. As Table 6.1 shows, only the SA12 and 16 show error values below 5% for all three target parameters. More detailed description of tumble and turbulence would most likely improve predictability, but again, as no additional data was available for calibrating the flow sub-model, the default settings were preferred. Another possible effect is the extensive influence of blow-by losses. The results in motored conditions (figure 6.3) give good confidence that the phenomenon is correctly modelled. The default blow-by sub-model included in the code was found to predict effective lambda values at EVO that were too low compared to measured relative air-fuel ratio at the exhaust. This was due to the fact that the default sub-model allows only air to escape the combustion chamber. While normally this would not be a problem, i.e. commercial engines feature around 1% blow-by [17], due to the high mass loss specific for the optical engine, the dedicated sub-model was preferred. Nonetheless, given that the simulation performed less satisfactory for spark advance 20 and 24 seems to confirm that this phenomenon can be one of the main reasons for lower accuracy for these conditions.

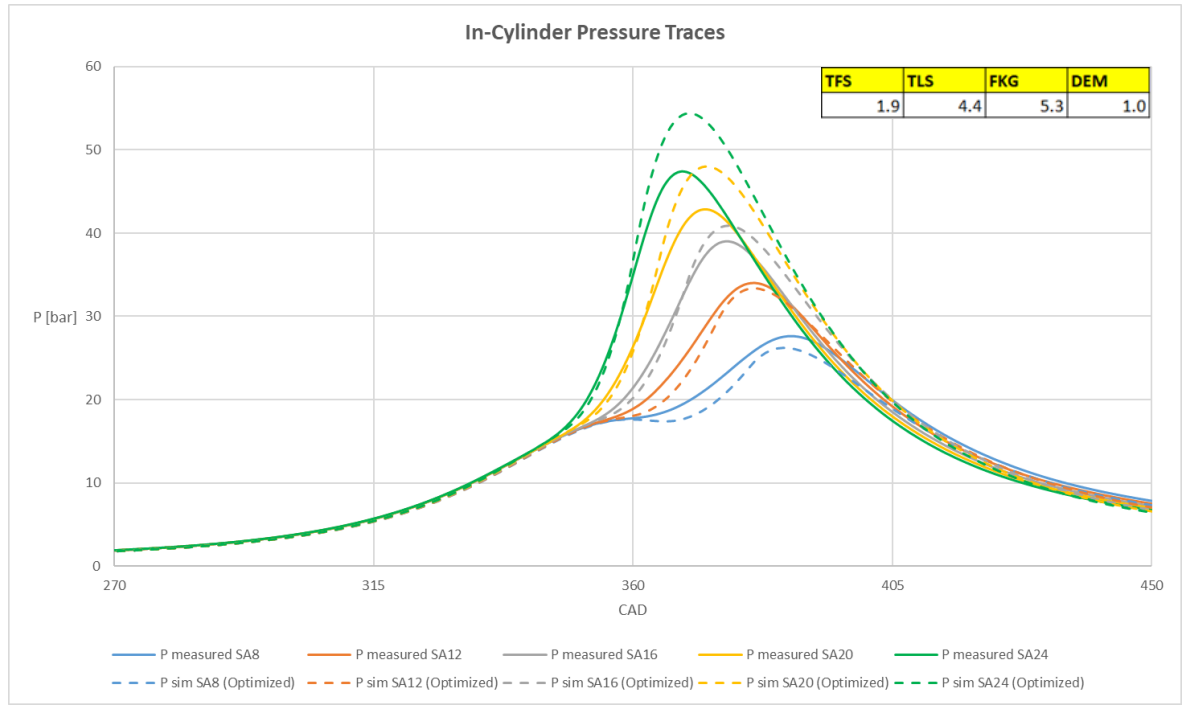


Figure 6. 7, In-cylinder Pressure traces comparison, $\lambda=1.15$, SA8 to 24 CAD BTDC.

ERROR%	SA8	SA12	SA16	SA20	SA24		
Pmax Error	5%	2%	5%	12%	15%		<5%
CAPmax Error	4%	0%	3%	4%	14%		5<E<15%
IMEP Error	7%	1%	4%	9%	14%		>15%

Table 6. 1, Calculated parameters error, $\lambda=1.15$, SA8 to 24 CAD BTDC.

In a second phase, the model was run with the optimized FKG, TFS and TLS values for the other two mixture strength settings, i.e. Duration of Injection (DOI) 30, 34 and 39 CAD, thus covering $\lambda=1.30$ -1.15-1.00 conditions, at a fixed spark timing of 12 CAD BTDC. Figure 6.8 shows the results for the three air-fuel ratio settings. As expected, the $\lambda=1.15$ condition featured the lowest error (given that this set of data was included in the optimization step), while $\lambda=1.30$ was characterized by large differences with respect to the measured parameters. The stoichiometric case featured good accuracy in terms of absolute peak pressure, while its location and IMEP were less satisfactory. The fact that the pressure trace is greatly anticipated for $\lambda=1.00$ suggests that FKG as well could be a determining factor. The initial phase of the process is highly dependent on the chemical reaction time, i.e. the results depend heavily on the value of laminar flame speed. This parameter is also essential for correct simulation in lean conditions, hinting towards the relatively high difference recorded for $\lambda=1.30$. Table 6.2 shows the relative error for each target parameter

and highlights that the stoichiometric case features high error only for the location of peak pressure, while the leanest condition fails to correctly model the pressure trace.

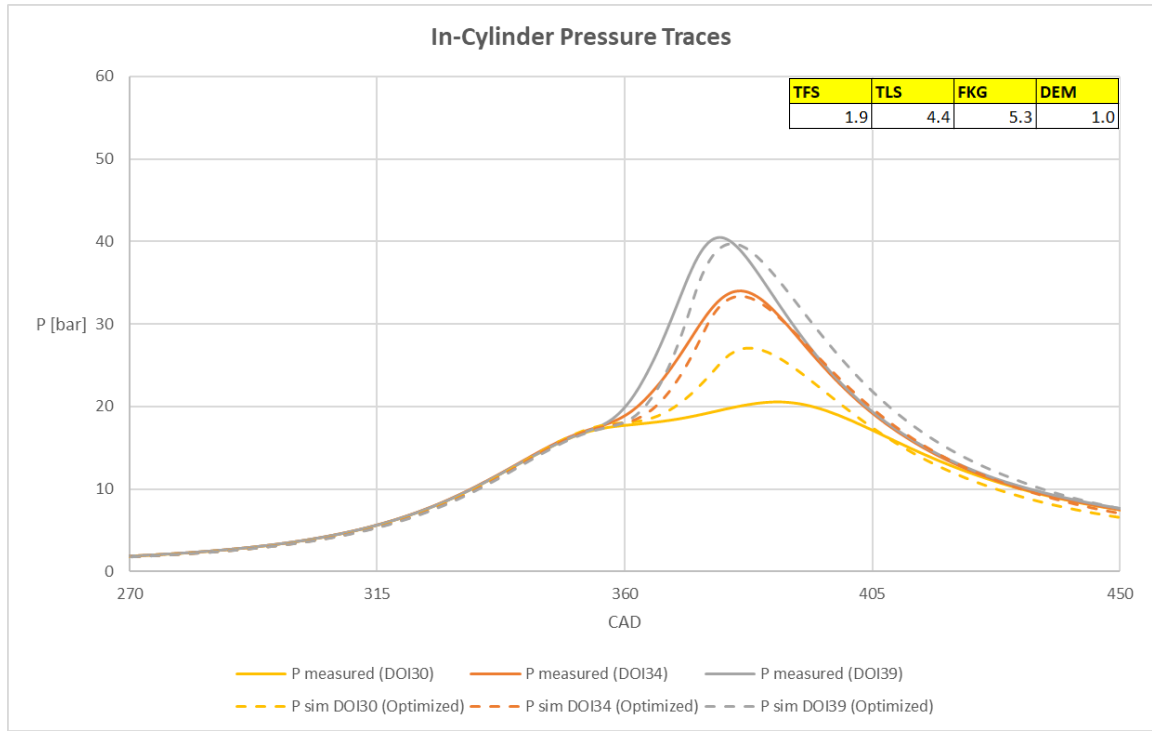


Figure 6. 8, In-cylinder Pressure traces comparison, SA12 CAD BTDC, $\lambda=1.00-1.15-1.30$.

ERROR%	DOI30	DOI34	DOI39		
Pmax Error	32%	2%	2%		<5%
CAPmax Error	17%	0%	14%		5<E<15%
IMEP Error	2%	1%	8%		>15%

Table 6. 2, Calculated parameters error, SA12 CAD BTDC, $\lambda=1.00-1.15-1.30$.

For the $\lambda=1.30$ case it is possible to attribute part of the difficulties of the model to return an acceptable matching to the high value of cyclic variability (COV_{IMEP} of 9.5%, Chapter 5, Figure 5.5). Figure 6.9 shows the entire set of 200 in-cylinder pressure traces, as well as the average and simulation data. There are numerous cycles that featured late burn, thus resulting in changes of the fluid composition at the end of the cycle, due to incomplete oxidation. Such significant variations in residual gas composition could explain, at least in part, the difficulties in simulating the combustion process. It should be noted that there no misfiring cycles recorded.

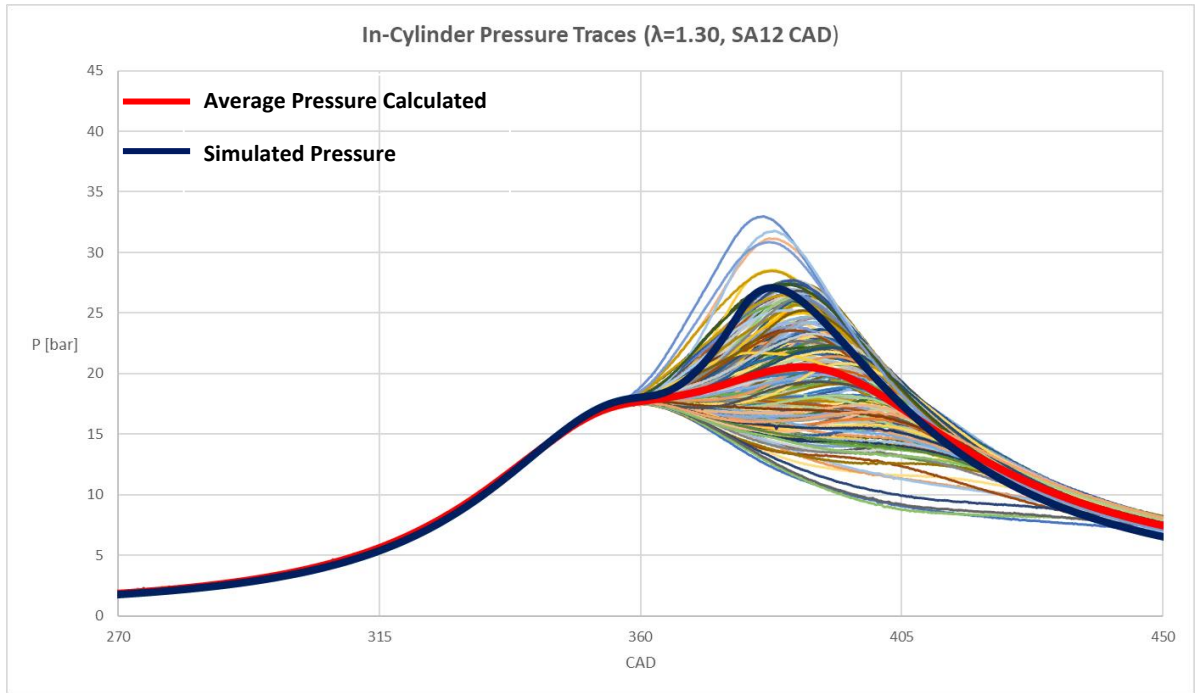


Figure 6. 9, In-Cylinder Pressure traces for $\lambda=1.30$, SA 12 CAD.

Figure 6.10 shows the normalized flame area (determined using the optical data recorded in cycle-resolved mode during the cycle that featured the trace closest to the average), compared to the calculated Wetted Flame Area (WFA). The latter parameter is referenced to the cylinder head, given the line-of-sight character of the optical data. The comparison reflects the overall accuracy that is similar to that shown in Tables 6.1 and 6.2 but constitutes a solid starting point for correlating simulations with the optical data.

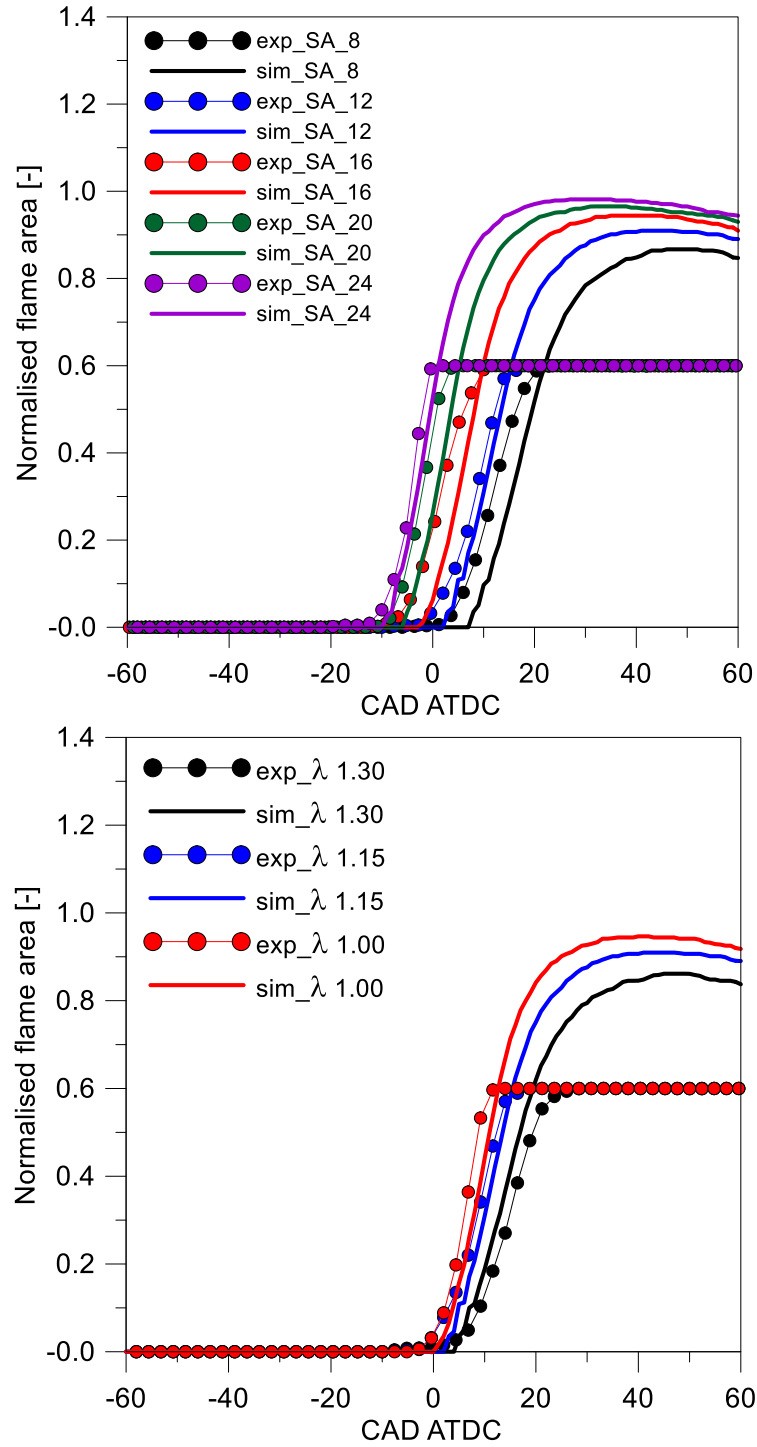


Figure 6. 10, Simulated (solid lines) and measured flame area (lines with symbols) for variable spark timing and air-fuel ratio.

More to the point, even if the 0D/1D nature of the model allows only a fraction of the resolution specific for 3D CFD simulations, important information of flame characteristics, as well as its interaction with the turbulent flow field can be obtain with contained computational effort.

To conclude, the GT-Power model was found to be predictive for part of the investigated conditions. The optimized set of calibration parameters was only partially successful in predicting the effect of spark timing and air-fuel ratio. Considering the difficulties intrinsically linked to this type of engine, the overall calibrations performed on the individual sub-models can however provide useful insight into in-cylinder phenomena, especially when considering the combination of thermodynamic and optical data. Further analysis on the turbulence and combustion model is needed to have a wider window of predictability (in terms of operative conditions covered by the optimizer).

Conclusive Remarks

The aim of the thesis work was to investigate the flame-fluid interaction for different operative conditions and return a database with the information on kernel displacement of flame front propagation direction. The main conclusions of this work are the following:

- Considering that the ignition strategy used for this study was the “Single breakdown event”, the coil charge duration does not seem to affect the engine performances in an appreciable way. However, a decreasing trend of the COV of the secondary current intensity signal was observed for extended duration of coil charge.
- For a fixed Spark Advance at 12 CAD and variable Air-Fuel ratio (λ), the Uniflow configuration seems to show a peak in terms of engine performance (Higher value of IMEP and lower COV_{IMEP}). For this operative condition, the Crossflow configuration has registered the higher value of COV-Is.
- For a fixed Air-Fuel ratio set to $DOI_{34}/\lambda=1.15$, in line with the previous study [19], the Counterflow configuration showed the slowest flame front propagation; in fact the latter achieves the MBT condition for a Spark Advance of 20 CAD, while for the other two configurations it is obtained for a SA of 16 CAD. The optical results confirm the thermodynamic data.
- The optical analysis, for a fixed SA, showed a reversal trend along the vertical axis (passing from the exhaust to the intake valves) for all the three configurations examined, with the fastest decrease recorded for the Crossflow orientation. In line with [19], the Crossflow configuration has registered the largest radial displacement of flame kernel with respect to the spark plug center.
- The optical analysis, for a fixed AFR, showed a reversal trend along the vertical axis (passing from the intake to the exhaust valves) up to 16 CAD for all the three configurations (the only exception is for Counterflow configuration with a SA of 8 CAD).
- The GT-Power model return a good level of predictivity for the operative cases with a fixed $\lambda=1.15$ and Spark Advance from 8 to 16 CAD. Further analysis and calibrations on the engine submodels are needed to improve the capacity of the model to return a better matching between simulated and measured in-cylinder pressure traces.

The results obtained suggest some interesting reference points for future analysis for the investigation on the Flame-Fluid interaction in a DISI engine. The Counterflow configuration sometimes exhibited opposite behavior in terms of optical results compared to the other two configurations. This orientation certainly requires more in-depth studies to improve and validate the results just obtained.

References

1. Statistical Review of World Energy 2020 | 69th edition.
2. IEA, *Global energy-related CO₂ emissions by sector*, IEA, Paris <https://www.iea.org/data-and-statistics/charts/global-energy-related-co2-emissions-by-sector> .
3. Light Duty Vehicle Stock by Technology Type, 2016 Annual Energy Outlook, United States Energy Information Administration.
4. European Environment Agency (online data code: env_air_gge).
5. Robert S., How advancing mobility will disrupt the mining and metals sector, EY US Mining & Metals Leader, <https://go.ey.com/33ShwOt>.
6. Avery K., Electric Vehicles Drive up Metals Demand, Visual Capitalist, <https://www.visualcapitalist.com/electric-vehicles-drive-up-metals-demand/#:~:text=Copper%2C%20nickel%2C%20and%20lithium%20are,in%20demand%20of%209%2D10x> .
7. Midterm Evaluation of Light-Duty Vehicle Greenhouse Gas Emission Standards and Corporate Average Fuel Economy Standards for Model Years 2022-2025, Draft Technical Assessment Report, Office of Transportation and Air Quality, United States Environmental Protection Agency, 2016.
8. Johansson AN, Hemdal S, Dahlander P ,2013, Experimental Investigation of Soot in a Spray-Guided Single Cylinder GDI Engine Operating in a Stratified Mode, SAE Technical Paper.
9. Yang J, Anderson RW, 1998, Fuel Injection Strategies to Increase Full-Load Torque Output of a Direct-Injection SI Engine, SAE Technical Paper.
10. Paul C. Miles, 2014, THE HISTORY AND EVOLUTION OF OPTICALLY ACCESSIBLE RESEARCH ENGINES, Sandia National Laboratories.
11. Bowditch, F.W., "Cylinder and Piston Assembly," in US Patent App. 2,919,688, 2,919,688.
12. Lee, D.W., A study of air flow in an engine cylinder, in NACA-TR-653, 1939.
13. Bowditch, F.W. "A New Tool for Combustion Research A Quartz Piston Engine," SAE technical paper 610002, 1961.

14. Holmström K, Denbratt I. Cyclic variation in an SI engine due to the random motion of flame kernel. SAE technical paper 961152; 1996. <http://dx.doi.org/10.4271/961152> .
15. Stone CR, Brown AG, Beckwith P. Cycle-by-cycle variations in spark ignition engine combustion – Part II: modeling of flame kernel displacements as a cause of cycle-by-cycle variations. SAE technical paper 960613; 1996. <http://dx.doi.org/10.4271/960613> .
16. N. Ozdor, M. Dulger, E. Sher, Cyclic variability in spark ignition engines, SAE Technical Paper No. 940987; 1994.
17. Heywood, J.B. Internal Combustion Engine Fundamentals. McGraw Hill. New York, USA, 1988.
18. M. Sjerić, D. Kozarac, R. Tatschl, 2015, Modelling of early flame kernel growth towards a better understanding of cyclic combustion variability in SI engines, Energy Conversion and Management, Vol.103, pag. 895-909.
19. Wang, Y., Zhang, J., Wang, X., Dice, P. et al., Investigation of Impacts of Spark Plug Orientation on Early Flame Development and Combustion in a DI Optical Engine, SAE Int. J. Engines 10(3):2017, doi:10.4271/2017-01-0680.
20. Irimescu, A., Merola, S., and Martinez, S., Influence of Engine Speed and Injection Phasing on Lean Combustion for Different Dilution Rates in an Optically Accessible Wall-Guided Spark Ignition Engine, SAE Int. J. Engines 11(6):1343–1369, 2018, doi:10.4271/2018-01-1421.
21. A. Schirru, A. Irimescu, S. Merola, A. d’Adamo, S. Fontanesi, Flame Kernel Growth and Related Effects of Spark Plug Electrodes: Fluid Motion Interaction in an Optically Accessible DISI Engine, World Academy of Science, Engineering and Technology International Journal of Mechanical and Mechatronics Engineering Vol:14, No:3, 2020.
22. Aleiferis P.G., Hardalupas Y., et al. Flame chemiluminescence studies of cyclic combustion variations and air-to-fuel ratio of the reacting mixture in a lean-burn stratified-charge spark-ignition engine, Combustion and Flame 136 (2004) 72-90.
23. Yang J, Anderson RW (1998) Fuel Injection Strategies to Increase Full-Load Torque Output of a Direct-Injection SI Engine. SAE Technical Paper 980495. doi: 10.4271/980495.

24. Serras-Pereira J, Aleiferis P, Richardson D, Wallace S (2007) Spray Development, Flow Interactions and Wall Impingement in a Direct-Injection Spark-Ignition Engine. SAE Technical Paper 2007-01-2712. doi: 10.4271/2007-01-2712.
25. Serras-Pereira J, Aleiferis P, Richardson D, 2012, Imaging and heat flux measurements of wall impinging sprays of hydrocarbons and alcohols in a direct-injection spark-ignition engine, <https://doi.org/10.1016/j.fuel.2011.07.037>.
26. Celik. M. B., Ozdalyan B. Gasoline direct injection. Fuel Injection. Siano D. InTech. Sciyo. ISBN 978-953-307-116-9.
27. Alkidas A. Combustion Advancements in gasoline engines. Energy Conversion and Management 48 (2007) 2751-2761.
28. Costa M., Sorge U., Allocca L., Increasing energy efficiency of a gasoline direct injection engine through optimal synchronization of single or double injection strategies. Energy Conversion and Management, Volume 60, 2012, Pages 77-86,ISSN 0196-8904, <https://doi.org/10.1016/j.enconman.2011.12.025>.
29. A. Schirru, A. Irimescu, S. Merola, A. d'Adamo, S. Fontanesi, "Flame Kernel Growth and Related Effects of Spark Plug Electrodes: Fluid Motion Interaction in an Optically Accessible DISI Engine ", World Academy of Science, Engineering and Technology International Journal of Mechanical and Mechatronics Engineering Vol:14, No:3, 2020.
30. <https://www.autodoc.co.uk/bosch/13782787>.
31. Irimescu, A., "Back-Pressure and Fuel Type Effects on Exhaust Gas Oxygen Sensor Readings for a Single Cylinder Spark Ignition Engine Running on Gasoline and Ethanol," SAE Technical Paper 2019-24-0046, 2019, doi:10.4271/2019-24-0046.
32. AVL DiTEST GmbH, "USER MANUAL AVL DITEST GAS 1000", www.avlditest.com.
33. Irimescu, A., Vasiu, G., and Trif Tordai, G., "Performance and Emissions of a Small Scale Generator Powered by a Spark Ignition Engine with Adaptive Fuel Injection Control," Appl. Energ. 121:196-206, 2014, doi:10.1016/j.apenergy.2014.01.078.
34. Eni S.p.A., Refining & Marketing and Chemicals "Benzina RON 95 E10".

35. S. Martinez, S. Merola, A. Irimescu, "Flame Front and Burned Gas Characteristics for Different Split Injection Ratios and Phasing in an Optical GDI Engine", Applied Sciences, MDPI.
36. Ge, H. and Zhao, P., "Numerical Investigation of the Spark Plug Orientation Effects on Flame Kernel Growth," SAE Technical Paper 2019-01-0005, 2019, doi:10.4271/2019-01-0005.
37. Optronis GmbH, "Optronis Hight-Speed Video Camera", Adept Electronic Solutions www.adept.net.au.
38. Clasen, K. and Koopmans, L., "Investigation of Homogeneous Lean SI Combustion in High Load Operating Conditions", SAE Technical Paper 2020-01-0959, 2020, doi:10.4271/2020-01-0959.
39. *** Gamma Technologies, GT-SUITE Flow Theory Manual Version 7.4, 2019.